# Numerical Modeling of Plasmas in which Nanoparticles Nucleate and Grow

A Dissertation
SUBMITTED TO THE FACULTY OF
UNIVERSITY OF MINNESOTA
BY

Pulkit Agarwal

IN PARTIAL FULFILLMENT OF THE REQUIREMENTS
FOR THE DEGREE OF
DOCTOR OF PHILOSOPHY

Adviser
Steven L. Girshick

October 2012

## Acknowledgements

I would like to express my immense gratitude to my adviser, Prof. Steven L. Girshick, for his guidance and support during the course of my PhD. He has always inspired me to be a very genuine, honest and thoughtful person. I have a deep appreciation for his attitude towards his work and his thorough understanding of the subject. He taught me to think very fundamentally and always aim for the best quality work. I feel very fortunate to have him as my adviser. His guidance and training has helped me not only in academics but also in making some very important decisions in life. Due to his constant support, encouragement and considerate nature, my entire experience as a graduate student has been very nice and exciting.

I also wish to acknowledge Dr. Uwe Kortshagen, Dr. Eray Aydil, Dr. P H McMurry Dr. Douglas Ernie, Dr. Laifa Boufendi, Dr Johannes Berndt and Dr Eva Kovacevic for their support and valuable comments. I would also like to acknowledge the support for research from National Science Foundation and Department of Energy.

I would also like to thank my friends Ankur, Srijan, Saket, Ricky and Brijesh for their wonderful friendship and immense help during the course of my PhD. I would like to express my thanks to Romain Le Picard and Karl Stathakis for being very good friends. I learned so many lessons related to life from Romain. I would like to acknowledge the immense help provided by Karl in proof reading the thesis and taking his valuable time to correct the grammar. I would like to thank Meenakshi Mamunuru for being very good friend and for very helpful discussions on the dusty plasmas and other topics related to life.

Finally, I would like to acknowledge my teacher from IIT and my family for their guidance in every aspect of life. Without the guidance from my teacher from IIT, it would have been difficult to take up this challenge of PhD. His guidance has always helped me seeing the reality and facing the difficult situations of life.

## Dedication

To the source of everything, my parents and my loving sister

## Abstract

Dusty plasmas refer to a broad category of plasmas. Plasmas such as argon-silane plasmas in which particles nucleate and grow are widely used in semiconductor processing and nanoparticle manufacturing. In such dusty plasmas, the plasma and the dust particles are strongly coupled to each other. This means that the presence of dust particles significantly affects the plasma properties and vice versa. Therefore such plasmas are highly complex and they involve several interesting phenomena like nucleation, growth, coagulation, charging and transport. Dusty plasma afterglow is equally complex and important. Especially, residual charge on dust particles carries special significance in several industrial and laboratory situations and it has not been well understood.

A 1D numerical model was developed of a low-pressure capacitively-coupled plasma in which nanoparticles nucleate and grow. Polydispersity of particle size distributions can be important in such plasmas. Sectional method, which is well known in aerosol literature, was used to model the evolving particle size and charge distribution. The numerical model is transient and one-dimensional and self consistently accounts for nucleation, growth, coagulation, charging and transport of dust particles and their effect on plasma properties. Nucleation and surface growth rates were treated as input parameters. Results were presented in terms of particle size and charge distribution with an emphasis on importance of polydispersity in particle growth and dynamics. Results of numerical model were compared with experimental measurements of light scattering and

light emission from plasma. Reasonable qualitative agreement was found with some discrepancies.

Pulsed dusty plasma can be important for controlling particle production and/or unwanted particle deposition. In this case, it is important to understand the behavior of the particle cloud during the afterglow following plasma turn-off. Numerical model was modified to self consistently simulate the dynamics and charging of particles during afterglow. It was found that dusty plasma afterglow is dominated by different time scales for electron and ion dynamics. Particle size and charge distribution changes significantly during the afterglow.

Finally, a simplified chemistry model was included in dusty plasma numerical model to simulate the dynamics of argon-silane dusty plasma. The chemistry model treats silane dissociation and reactions of silicon hydrides containing up to two silicon atoms. The nucleation rate is equated to rate of formation of anions containing two Si atoms, and a heterogeneous reaction model is used to model particle surface growth. Evolution of particle size and concentration is explained and the importance of variable surface growth rate and nucleation rate is discussed.

## Table of Contents

# List of Tables

# List of Figures

# List of symbols

| | |
|---|---|
| $a$ | Dust particle radius, section spacing |
| $A$ | Arrhenius parameter |
| $\bar{A}_{p,j}$ | Average particle surface area |
| $\dot{B}_J$ | Intra-sectional growth |
| $b_c$ | Effective ion collection parameter of a nanoparticle |
| $b_{\pi/2}$ | Effective ion impact parameter of a nanoparticle |
| $\dot{C}_J$ | Inter-sectional growth |
| $D$ | Diffusion coefficient |
| $d_P$ | Dust particle diameter |
| $E$ | Electric field |
| $\tilde{E}$ | Effective electric field |
| $E_{image}$ | Enhancement due to image potentials |
| $E_{Dipole}$ | Enhancement due to dipole interaction |
| $E_A$ | Activation energy |
| $F_e$ | Electric force |
| $F_{ID}$ | Ion drag force |
| $F_c$ | Collection force |
| $F_o$ | Orbital force |
| $F_T$ | Thermophoretic force |
| $F_{ND}$ | Neutral drag force |
| $F_G$ | Force due to gravity |
| $g$ | Gravitational constant |
| $I$ | Scattered light intensity |
| $I_0$ | Incident light intensity |
| $k_B$ | Boltzmann constant |
| $k$ | Dust particle charge, rate constant |
| $k_{sg}$ | Surface growth rate constant |

| | |
|---|---|
| $\dot{L}_{RD}$ | Loss due to radial diffusion |
| $\dot{L}_P$ | Loss due to pump |
| $m$ | Mass, refractive index |
| $m_r$ | Reduced mass |
| $n$ | Density |
| $N_{i,k}\ or\ N_{j,k}$ | Density of dust particles in size section i or j and charge k |
| $N_j$ | Dust particle density in section j for all charge states |
| $\dot{N}_s$ | Dust particle growth rate |
| $n(u)$ | Dust particle size distribution within section |
| $P$ | Pressure |
| $Q_{NCP}$ | Net charge on dust particles |
| $Q$ | Dust particle charge |
| $q_e$ | Electron energy flux |
| $q(u)$ | Size dependent property |
| $Q_{ext}$ | Ratio of scattered vs. incident laser light intensity |
| $r$ | Radius of dust particle |
| $R$ | Radius of reactor, distance between particle and light detector |
| $\dot{R}_P$ | Rate of production |
| $\dot{R}_L$ | Rate of loss |
| $S$ | Source and sink terms |
| $T$ | Temperature |
| $T_{Res}$ | Residence time |
| $t$ | Time |
| $u$ | Logarithm of particle volume |
| $v$ | Velocity, volume |
| $V$ | Voltage |
| $x_s$ | Surface coverage of surface species |
| $x$ | Spatial coordinate |

| | |
|---|---|
| $z$ | Dust particle charge |

## Greek symbols

| | |
|---|---|
| $\theta$ | Scattering angle |
| $\lambda$ | Wavelength, characteristic length for radial diffusion |
| $\beta$ | Coagulation coefficient, temperature exponent |
| $\sigma, \varepsilon$ | Lennard Jones parameter |
| $\epsilon$ | Dielectric constant |
| $\nu$ | Charging frequency |
| $\Phi$ | Dust particle potential, inter particle potential |
| $\Gamma$ | Flux term |
| $\rho$ | Mass density |
| $\sigma_o$ | Orbit momentum transfer cross section |
| $\kappa_T$ | Translational part of thermal conductivity |
| $\mu$ | Mobility, viscosity |
| $\lambda_L$ | Linearized debye length |
| $\alpha$ | Accommodation coefficient, Coefficient for charging |

## Subscripts

| | |
|---|---|
| $+$ | Positive ion |
| $j$ | Species index, size section |
| $i$ | Size section index |
| $k$ | Charge state index |
| $p$ | Dust particle |
| $e$ | Electron |
| $coag$ | Coagulation |

# Chapter 1: Introduction

## 1.1 Dusty Plasma

Plasmas are ionized gases that consist of free electrons, ions and neutral gas atoms and molecules. Plasma is created by supplying high energy to the gas by either thermal heating of the gas or by the application of strong electromagnetic fields which cause free electrons to gain enough kinetic energy to ionize the heavy neutral gas atoms upon collision. Dusty plasmas are a special class of plasmas that contain dispersed particulates having diameters in the range of a few nanometers to several micrometers or even much larger in the case of astrophysical plasmas. These dust particles are different from electrons and ions and are negatively charged because of the high mobility of electrons in comparison to ions.

Dusty plasmas are ubiquitous in nature and can occur in both cosmic and terrestrial surroundings (1,2). The vast majority of the visible universe is in the form of plasmas, ranging from hot, dense stars to much cooler solar wind and cold plasmas of intergalactic space. Most of the space plasma coexists with the cosmic dust. Terrestrial dusty plasmas include atmospheric, laboratory and industrial plasmas with dust particles. Noctilucent clouds are a fascinating example of atmospheric dusty plasmas. Noctilucent clouds are believed to be composed of ice coated particulates in the dry polar mesosphere. Particle formation and growth in laboratory/industrial plasmas can be due to a variety of reasons. Dust particles are formed in fusion reactors by the erosion of the inner discharge walls (3,4). However, in low pressure plasmas, dust formation can occur by the chemical nucleation or wall sputtering by high energy ions(5).

It is clear from the above discussion that dusty plasmas refer to a broad category of plasmas ranging from space plasmas to laboratory plasmas. There has been significant research in the area of dusty plasma. However, these plasmas are highly complex and they are still not well understood.

## 1.2 Regime of interest and applications

Many applications of plasma require a precursor gas flow which is different from the plasma carrier gas and is meant for specific application. For example, silane gas in argon plasma is required for chemical vapor deposition of silicon over a wafer. Energetic electrons present in the plasma can dissociate the precursor gas and form several reactive species like radicals and ions. Nucleation occurs when small reactive species present in the plasma react with each other and generate stable nuclei, which grow by coagulation and surface growth. These freshly generated nanoparticles become mostly negatively charged because of the higher mobility of electrons compared to ions. Particles are transported by diffusion and a variety of forces, including the electrostatic force, neutral gas drag, ion drag, thermophoresis and gravity (2).

In such chemically reactive plasmas, particle size is in nanometer range and their concentration may be as high as $10^8$ to $10^{10}$ per $cm^3$. In this regime, plasma and the dust particle cloud are very strongly coupled to each other. This means that the presence of charged nanoparticles in the plasma strongly affects the spatial distribution of electrons and ions. This regime is quite important and it occurs in several industrial and laboratory situations.

Chemically reactive dusty plasmas became a popular area of research after an important discovery by Selwyn et al (6) in 1989. They found that the particles formed inside the plasma reactor are the main cause of contamination in semiconductor manufacturing which led to a massive research on understanding the formation and transport of dust particles inside the plasma (7-12). Initial research in this field was focused on removing dust particles from plasma. However, later, these particles became objects of keen interest because of their various applications.

Dusty plasmas find applications primarily in nanoparticle synthesis for various processes. It has been noticed that particles can be tailored using different precursor gases in dusty plasmas (13). Dusty plasmas are also used for increasing the yield of plasma enhanced chemical vapor deposition (PECVD) process because for specific set of conditions when dust is present in plasma, electron temperature increases which results in increased vapor deposition over a substrate (2). In another application, dusty plasmas are used for embedding particles in thin films. Such particle-seeded thin films are used in solar cells, optoelectronics and lubrication (14). Dusty plasmas are also used in the pharmaceutical industry to functionalize microparticles for medical applications (15). In summary, applications of dusty plasmas are growing rapidly and many research groups are working to understand the fundamentals of dusty plasmas to have better control over the particle formation and growth process.

## 1.3 Background

Dusty plasma is a multi-disciplinary subject. Research in dusty plasma can be categorized into three major areas named formation and growth of dust particles, particle charging,

and particle transport. A brief overview of prior research on these areas is discussed in the following sections.

### 1.3.1 Particle formation

Low pressure argon-silane discharges are used for depositing thin silicon films on silicon wafers in the semiconductor industry. In 1989, Selwyn et al (6) found that contamination problems in such discharges were due to particles formed inside the plasma. Particle formation occurs over a wide range of process conditions and results in deposition of particles on thin films causing process yield to go down. Initial research in this area was focused on understanding the mechanism of particle formation. The nucleation of particles in a silane discharge occurs through a series of gas phase polymerizing reactions. In 1993, Choi and Kushner (10) pointed out the role of negative ions as a precursor for formation of particles. They performed Monte Carlo simulations and proposed that the residence time of neutral particles in plasma is too short to generate a higher order cluster. However, negative ions which are trapped in the plasma due to electric force allow the growth of large clusters. Howling and Hollenstein (16) showed by mass spectroscopy experiments that negative hydrogenated silicon ions reach much higher masses than positive ions, and therefore negative ions are the possible precursors to particulate formation in silane plasmas. They also suggested that ion molecule reactions or ion – ion recombination can be possible pathways to particle formation.

The pathway for silicon hydride clustering has been a contentious issue as some of the authors have reported experimental evidence of short life time radicals like $SiH_2$ etc. playing a key role in particle formation. In 1993, Veprek et al (17) have shown by

comparison of laser light scattering experiments and theoretical calculations that mechanism of cluster formation proceeds through $SiH_2$ insertion reactions. In 1997, Watanabe et al (18) performed laser light scattering and infrared diode laser spectroscopic experiments at various frequencies and observed $SiH_2$ and particle density profiles. They found that particle density profile is quite similar to $SiH_2$ density profile and thus clustering proceeds by $SiH_2$ insertion reactions.

First detailed chemistry model of particle formation during the chemical vapor deposition of silicon from silane was developed by Swihart and Girshick (19). They used group additivity schemes to get the thermo-chemical properties of silicon clusters having up to 10 silicon atoms. They considered a total of 221 species and 2614 reactions and used CHEMKIN (20) to integrate the rate equations. They used the numerical results to indentify the most important reaction paths leading to particle formation during the silane pyrolysis. Bhandarkar et al (21) extended the model of Swihart and Girshick (19) to simulate the particle formation mechanism in the plasma enhanced chemical vapor deposition process. They considered electron dissociation and attachment reactions, anion-neutral reactions and reactions involving silyls and H radicals and neutralization reactions in their plasma model. They observed that clustering in the plasma enhanced chemical vapor deposition process predominantly occurs via reactions between anions and $SiH_4$ instead of silane insertion reactions in the thermal chemical vapor deposition as predicted by Swihart and Girshick (19). This is important because in the plasma, several reactive species are present and the chemistry of particle formation is unique. They also concluded that $SiH_2$ insertion reaction is important only among the small silicon hydrides

with up to three or four silicon atoms. Their chemistry model consists of 300 species and 5500 reactions.

Gallagher et al (22) analyzed the experimental results of Howling and Hollenstein (16) and developed a model to understand the early stages of cluster growth. They found that anion-neutral reactions are important for nucleation however neutral species which induces cluster growth is $SiH_3$ radical and not $SiH_4$ as mentioned in paper by Bhandarkar et al (21).

The above review shows that particle formation has been a well researched subject. Although a majority of theories support the mechanics of particle formation via anions, some studies have shown the importance of $SiH_2$ insertion reaction in particle formation. Plasma chemistry is a complex phenomenon and a detailed explanation is still lacking. Thus, understanding the science of particle formation is a challenging problem.

### 1.3.2 Particle growth

The first model for particle growth in silane plasmas was given by Boufendi and Bouchoule (7). They carried out laser light scattering measurements on particles in a low pressure argon-silane RF discharge and performed time resolved TEM analysis to obtain temporal information on formation and growth kinetics. They proposed that particle formation follows three well-defined steps. In the first step small size (~2 nm) crystalline particles are formed by gas phase nucleation which involves polymerizing reactions as mentioned above. The second step is coagulation which eventually stops because particles acquire negative charges and consequently start repelling each other. Finally,

particles grow by surface deposition processes which go on until the power supply is switched off.

Warthesen and Girshick (23) developed a numerical model of the spatiotemporal evolution of nanodusty plasmas. They assumed an initial burst of nucleation followed by coagulation and surface growth based on the findings of Boufendi et al (7). They reported that the effect of coagulation on particle growth is negligible, and their simulation results are in qualitatively good agreement with laser light scattering experiments. Ravi and Girshick (24) extended the model of Warthesen (23) by adding the effect of image potential on coagulation coefficients and by extending the nucleation condition from initial burst to a combination of initial burst and nucleation in the particle free region. They found that coagulation is important as long as small particles are present in the reactor due to ongoing nucleation. Coagulation ceases shortly after quenching of nucleation. They also found that image potentials i.e. polarity induced in smaller neutral particles in proximity of charged particles, play a key role in coagulation.

Tachibana et al (13) have shown that particles can be tailored to have spherical shape and range of sizes by controlling the surface growth. Particle growth is important in many dusty plasma applications. Detailed knowledge of various processes related to particle growth is required to improve upon existing applications and to develop further applications.

### 1.3.3 Particle charging

A dust particle in plasma acquires net negative charge and responds to electric field. Electrons being more mobile than ions reach the particle's lattice giving it a net negative charge. A negatively charged particle starts repelling the electrons and attracting the ions and a steady state is achieved when net flux of ions and electrons to the particle is equal. The ion and electron flux to a particle depends on the charge of the particle which in turn depends on the size of the particle. If the particle is very small (less than ~ 5 nm) then the charge on particles can fluctuate between negative, neutral, and positive due to the discrete nature of charging.

The orbital motion limited (OML) theory given by Mott-Smith and Langmuir (25) is often used to calculate the charge on a particle. This theory assumes that plasma properties are unperturbed far away from the surface, the plasma sheath is collisionless, and the particle radius is much smaller than the Debye length. With these assumptions, OML theory is based on the principles of angular momentum conservation and energy conservation. A collection radius is defined such that ions inside the collection circle will be collected at the surface of the particle, and theoretical expressions for ion and electron flux are obtained. OML theory provides reasonably accurate results for plasma where the above assumptions are valid. However, in practice, these assumptions are true only for the collisionless regime where the Knudsen number ($\lambda/a$, where $\lambda$ is mean free path and a is the radius of particle) is greater than $10^3$ (26). Some of the shortcomings of OML theory include the assumption of monotonically decreasing effective potential around the particle, no trapped ions in the sheath around the particle which are generated due to

charge exchange collisions within the sheath around the particle and no secondary electron emission from particles.

Zobnin et al (27) proved theoretically that charge exchange collisions within the sheath of a dust particle have an important effect on the charge of particle. They developed a molecular dynamics model to calculate the charge on a particle by taking charge exchange collisions into account. They found that even with the assumption of the particle radius being much smaller than the Debye length, the OML theory leads to a large error in estimating the charge on dust particles. Recent experiments performed by Ratynskaia et al (28) have shown good agreement with the results of Zobnin et al (27).

Gatti and Kortshagen (29) followed the molecular dynamics model of Zobnin (27) and developed an extensive analytical model which is valid for a wide range of sheath collisionality varying from collisionless to highly collisional hydrodynamic regime. Their model was based on the concept of capture radius which is defined in a way that ions having collisions within the capture radius will finally be collected on the particle surface. They found good agreement between analytical and molecular dynamics results.

Charging is a very important phenomenon in dusty plasmas. Particles will never be trapped if they do not get charged. Coulomb crystal (30) observed in dusty plasmas is also a consequence of dust particle charging. A charged particle responds to forces like electrostatic force and ion drag and thus has interesting dynamics within plasma.

### 1.3.4 Particle dynamics

Dust particles in plasma experience various forces which confine them in plasma or drag them to the walls. Dust particles in plasma gain net negative charge thus they are subjected to electric force and ion drag force. Apart from these forces, dust particles experience viscous drag, thermophoresis, and gravity. A brief overview of various transport phenomena related to dust particles is discussed in following sections.

#### 1.3.4.1 Diffusion

Particle formation occurs in the bulk of plasma outside the sheaths. Therefore, particle concentration is high in the center and it decreases towards the walls. As a result of concentration gradient, dust particles tend to diffuse towards the wall. In low pressure plasmas, dust particles lie in free molecular regime which means that mean free path of gas molecules is greater than the dust particle diameter. At low pressures like 10 Pascal, mean free path of gas molecules is on the order of 10 μm whereas the dust particle radius in nanodusty plasmas is in nanometers. The expression of dust particle diffusion coefficient in the free molecular regime is (2):

$$D_p = \frac{1}{a^2\, n_g}\sqrt{\frac{k_B T_g}{2\pi m_g}}\left(\frac{3}{8}\right)\left(1 + \alpha\frac{\pi}{8}\right)^{-1}, \qquad (1.1)$$

where $a$, $n_g$, $k_B$, $T_g$, $m_g$ and $\alpha$ represent particle radius, neutral gas density, Boltzmann constant, neutral gas temperature, atomic mass of neutral gas and accommodation coefficient respectively. Accommodation coefficient accounts for specular or diffuse collisions with the gas molecules.

#### 1.3.4.2 Electric force

The electric force is the force which tends to trap dust particles in capacitively coupled RF plasmas. In capacitively coupled RF plasmas, negatively charged particles are pushed away from electrodes in the bulk of plasma by the action of electric field. It is interesting to note that a negatively charged dust particle experiences an electric force in plasma in spite of being surrounded by ions. Daugherty and Graves (9) analyzed this problem by solving linearized Poisson equation for a dust particle in a constant electric field. It was assumed that the dust particle is spherical with its radius being much smaller than the Debye length. Further it was assumed that the dust particle is present in the central region of plasma so that the sheath around a dust particle is spherically symmetric. They found that the potential around the particle consists of three terms. The first term corresponds to the potential due to original applied electric field, the second term is the Debye-Huckel potential and the third term corresponds to the polarization response of plasma. They calculated the electric force by the application of electrostatic stress tensor. The expression for electric force is:

$$\boldsymbol{F_e} = Q\boldsymbol{E_0}\left[1 + \frac{(a/\lambda_L)^2}{3(1 + a/\lambda_L)}\right], \qquad (1.2)$$

Where $Q$, $\boldsymbol{E_0}$, $a$ and $\lambda_L$ represent particle charge, electric field vector, particle radius, and linearized Debye length respectively. From the above expression, the net electric force on a dust particle in plasma consists of the force due to an external electric field and the force due to additional electrical field caused by polarization of plasma in response to an applied field. As stated above, it was assumed that a<< $\lambda_L$ so that the contribution of the second term in the above expression is very small. It is interesting to note here that

plasma does not shield the dust particle from the electric field, rather it adds an additional force.

Hamaguchi and Farouki (12) mathematically derived the force expression in a non-uniform plasma i.e. plasma with density gradients. They found that in the case of non-uniform plasma, the electric force has two components; one due to an applied electric field and another termed as 'polarization force', arising due to the gradient in Debye length. They estimated that the polarization force is around 16% of the net electrostatic force which means that even if the plasma is nonuniform, i.e. the sheath around the particle is distorted, plasma does not shield the dust particles from electric field. Polarization force acts in the direction of decreasing Debye length and it either enhances or reduces the electric field depending upon the direction of applied field.

#### 1.3.4.3 Ion drag force

An ion drag force acts on a dust particle in plasma because of momentum transfer from a positive ion current. In RF plasma, ions are accelerated towards electrodes by an electric field. When these ions contact the negatively charged particle's potential they either get deflected from their trajectories or get collected on dust particles and thus exchange momentum with the dust particle. The net momentum exchange caused by collection of ions at the particle surface is called collection force, and that caused by deflection of ions from their trajectory is called the orbit force. Barnes et al (8) derived the following expression for collection force using OML theory:

$$F_c = \pi a^2 n_i m_i v_T \boldsymbol{v_i} \left[1 - \frac{2eV(a)}{m_i v_T^2}\right], \quad (1.3)$$

where $n_i$, $m_i$, $v_i$, $v_T$ and $V(a)$ represent ion density, ion mass, ion drift velocity, total ion velocity, and particle potential respectively**.** They also give the following expression for the orbit force as derived by Bittencourt (31):

$$F_o = n_i m_i \sigma_o v_T \boldsymbol{v_i}\,, \quad (1.4)$$

where $\sigma_o$ is the orbit momentum transfer cross section for cut off Coulomb potential:

$$\sigma_o = 2\pi b_{\pi/2}^2 ln\left(\frac{\lambda_L^2 + b_{\pi/2}^2}{b_c^2 + b_{\pi/2}^2}\right), \quad (1.5)$$

where $b_c$ and $b_{\pi/2}$ represent the collection impact parameter and the impact parameter for ions whose asymptotic orbit angle is π/2.

Ion drag is considered important because of its role in determining the particle location and thus in void generation (32). The electric force and ion drag force act in opposite direction and depending on the size of the particle, they balance each other at a particular location. Kilgore et al (33) performed numerical calculations of the orbit momentum transfer cross section for cut off coulomb potential, screened coulomb potential and potential profile obtained by solving Poisson – Vlasov system. They found that the screened Coulomb potential can be used to calculate the orbit momentum collision cross section. Khrapak et al (34) extended the model of Kilgore et al (33) to take into account the ions with impact parameter greater than the Debye length. They found that their model give significantly larger magnitudes of ion drag force in comparison to previous

analytical models where the momentum transfer by ions having impact parameter greater than Debye length was neglected.

The above mentioned models assume collisionless plasma and do not take into account charge transfer collisions in the dust particle sheath. Ivlev et al (35) developed a linear kinetic approach to get an estimate of ion drag force in collisional plasma. However, their approach was limited to highly collisional plasmas. Recently, Ikkurthi et al (36) developed a 3D particle – particle – particle mesh model which accounted for necessary elastic and inelastic collisions with plasma species and realistic discharge conditions to accurately estimate the ion drag on dust particles. They found that the total ion drag force for collisional plasmas is larger than that for collisionless plasmas, and the force varies nonlinearly with the dust size.

#### 1.3.4.4 Thermophoresis

In presence of gradient in plasma gas temperature, gas molecules on the hotter side are more energetic and thus transfer more momentum to a suspended dust particle than gas molecules on the cooler side of plasma. As a result, dust particle experiences 'thermophoretic' force in the direction opposite to gas temperature gradient. Talbot (37) derived the following mathematical expression for thermophoretic force in free molecular regime (gas mean free path >> particle diameter):

$$F_T = -\frac{32}{15}\frac{a^2}{v_g}\kappa_T \boldsymbol{\nabla T}\left(1+\frac{5\pi}{32}(1-\alpha)\right), \tag{1.6}$$

where $\kappa_T$ is the translational part of thermal conductivity:

$$\kappa_T = \frac{15 k_B \mu}{4 m_g}, \tag{1.7}$$

where $\mu$, $m_g$, $k_B$, $v_g$, $\boldsymbol{\nabla T}$ and α represent dynamic viscosity, molecular mass of gas, Boltzmann constant, average thermal velocity, temperature gradient, and accommodation coefficient respectively. The accommodation coefficient accounts for collisions which are not specular, its value is 0 if the collisions are assumed to be perfectly specular and equal to 1 if the collisions are perfectly diffuse. Usually, accommodation coefficient is assumed to be 0.9.

Jellum et al (38) performed a series of experiments to study the effect of thermophoresis by looking at optical emission profiles and discharge electric properties in rf discharge with and without particles. They found that even a small gradient in gas temperature strongly affects the particle profile by pushing particles opposite to the temperature gradient. They did not observe any change in discharge property when they had pristine plasma with and without temperature gradient. Authors propose to use thermophoresis to scavenge particle from the plasma. De Bleecker et al (39) incorporated thermophoretic force in their one dimensional fluid model and observed similar particle profiles as in Jellum et al (38).

#### 1.3.4.5 Neutral drag

Neutral drag is also called viscous drag. The gas molecules collide with a bigger dust particle and transfer momentum because of which the dust particle experiences a drag force. In the free molecular regime, the neutral drag force can be written as (2):

$$F_{ND} = -\frac{4}{3}\pi a^2 m_g n_g v_g \left(\boldsymbol{u_D} - \boldsymbol{u_g}\right)\left(1 + \alpha\frac{\pi}{8}\right), \qquad (1.8)$$

Where $m_g$, $n_g$, $\boldsymbol{u_D}$ and $\boldsymbol{u_g}$ represent mass of neutral gas molecules, density of neutral gas, velocity of dust particle, and mean velocity of neutral gas, respectively. Drag force is proportional to the relative velocity between the gas and the particles. As described earlier, the accommodation coefficient accounts for the fact that all the collisions are not specular.

#### 1.3.4.6 Gravity

Gravitational force is proportional to the density and volume of the particle:

$$F_g = \tfrac{4}{3}\pi a^3 \rho \boldsymbol{g}\,, \qquad (1.9)$$

Here $\rho$ and $\boldsymbol{g}$ represent mass density of particle material and gravitational acceleration.

## 1.4 Motivation

Dusty plasma physics is a challenging field. It involves a wealth of complex physical and chemical phenomena. Although the field of dusty plasma is several decades years old, it has not been properly understood. There are still many unanswered questions. For example, the most convincing mechanism of particle formation, effect of dust particles on electron and ion distribution, charge distribution on particles, and events in dusty plasma afterglow are not well understood. Experimental techniques have limitations such as inability to detect subnanometer sized particles, inability to use Langmuir probes because of dust deposition, to name a few. Therefore, there is a need to develop a computational model which accounts for all the complex phenomena related to dusty plasma.

Developing such a computational model is a challenging task. Warthesen et al (23) has developed a numerical model which predicts the physical spatiotemporal behavior of strongly coupled plasma and dust particle system. However, this model fails to account for some very important phenomena like chemistry, non-Maxwellian distribution of electrons and ions etc. To bring this already developed model closer to reality and to understand the complex science involved in dusty plasma physics, it is required to account for various physical and chemical phenomena self consistently. Having such a numerical model and validating it with experiments will allow us to have fundamental understanding of dusty plasma system which can be used to explore further applications of dusty plasma.

# Chapter 2: Computational model

Any physical process can be approximated by a set of mathematical equations. These equations describe the essential physics behind a particular physical process. With the advancement of computer technology, numerical model and computer simulations have become an integral part of scientific community. Experiments are important but in many cases experiments have limitations and uncertainties and therefore are unable to explain the physics. In the modern world, computer simulations are extensively used for simulating different physical processes in the field of physics, astrophysics, chemistry, biology, economics, social sciences and of course engineering. Various modeling approaches like continuum, kinetic, hybrid etc. have been developed over the years to address specific problems. In this chapter, a brief overview of different approaches to dusty plasma modeling is presented followed by a detailed description of numerical model used for this work.

As mentioned earlier, main features of dusty plasmas include particle formation, growth, charging and transport. Several approaches, such as analytical models, fluid models, Monte Carlo (MC) methods and particle in cell methods etc., have been used for modeling of a particular feature or a combination of features of dusty plasma(40). Kushner (41) developed a detailed fluid model for silane chemistry in argon plasmas with polymerizing reactions leading to formation of dust. However, he did not account for dust particle growth, charging or transport. Belenguer et al (42) developed a self-consistent fluid and particle in cell model to study the electrical characteristics of dusty argon

plasmas. However, their model did not account for formation, growth and transport of dust particles.

Several numerical models have been proposed focused only on the particle formation mechanism. Choi and Kushner (10) used Monte Carlo method to understand the role of negative ions in the formation of particles. Bhandarkar et al (21) developed a zero dimensional fluid model with detailed chemistry to find the nucleation and surface growth pathways. Other modeling studies have focused on charging aspect of dusty plasma. Zobnin et al (27) and Gatti and Kortshagen (29) have used molecular dynamics techniques for understanding the importance for charge exchange collisions in particle charging. Similarly particle transport by ion drag force has been investigated by Ivlev et al (35) and Ikkurthi et al (36) by kinetic methods.

Few models exist which self consistently account for all the essential features of dusty plasma physics. Denysenko et al (43,44) and Schweigert et al (45) developed a self consistent model with kinetic description of electrons, however their model assumed a monodisperse particle distribution. Kortshagen and Bhandarkar (46) used sectional method to account for polydisperse size distributions and charge distributions for studying coagulation, however their model was zero dimensional and therefore neglected particle transport. De Bleecker et al (47) used sectional approach for size distribution in their 1D self consistent dusty plasma model with particle formation chemistry, however steady state charge on particles was calculated neglecting the charge distribution on particles. Also, their model neglected the charge dependence of coagulation and did not mention surface growth and effect of size distribution in their results. Girshick and

coworkers (23,24) developed a self consistent dusty argon plasma model using sectional method for particle charge and size distribution. The dust particle module was self consistently coupled to a plasma fluid model. Particle formation and growth chemistry were not modeled. Parameterized nucleation rate and surface growth rates were assumed based on the detailed chemistry study by Bhandarkar et al (21). Charge dependent coagulation including the effect of image potential was considered. They report the spatiotemporal evolution of particle size and charge distribution along with electron and ion densities.

In this work, the computational model of Girshick and coworkers (23,24) is used and modified to include dust particle formation and growth chemistry and the dust particle dynamics in an afterglow. Several other modifications were included to make computations more efficient and to have more functionality. A detailed description of model schematic and computational model is given in following sections.

## 2.1 Model schematic

Figure 2.1 shows the schematic of the model. Plasma model is of a capactively coupled plasma with upper electrode being RF powered and the lower electrode grounded. The upper electrode is showerhead and gas mixture flows through the upper electrode. The lower electrode can either be porous or solid. If the lower electrode is solid then gas flow is stagnation type flow otherwise the gas flow is considered to be uniform. It is assumed that the discharge is radially symmetric, therefore the calculations are performed only in 1D. Discharge is assumed to be pure argon plasma containing silicon nanoparticles. However, in the case where chemistry is included, discharge is a mixture of ions and

radicals produced by the silane chemistry in argon plasma. Discharge conditions include variable voltage, pressure, gas temperature, electrode gap, gas flow rate and argon-silane ratio. In the case with self consistent DC bias, plasma is connected to a blocking capacitor resulting in a bias on upper electrode. Detailed description of numerical model equations, assumptions and solution technique is given in following sections.

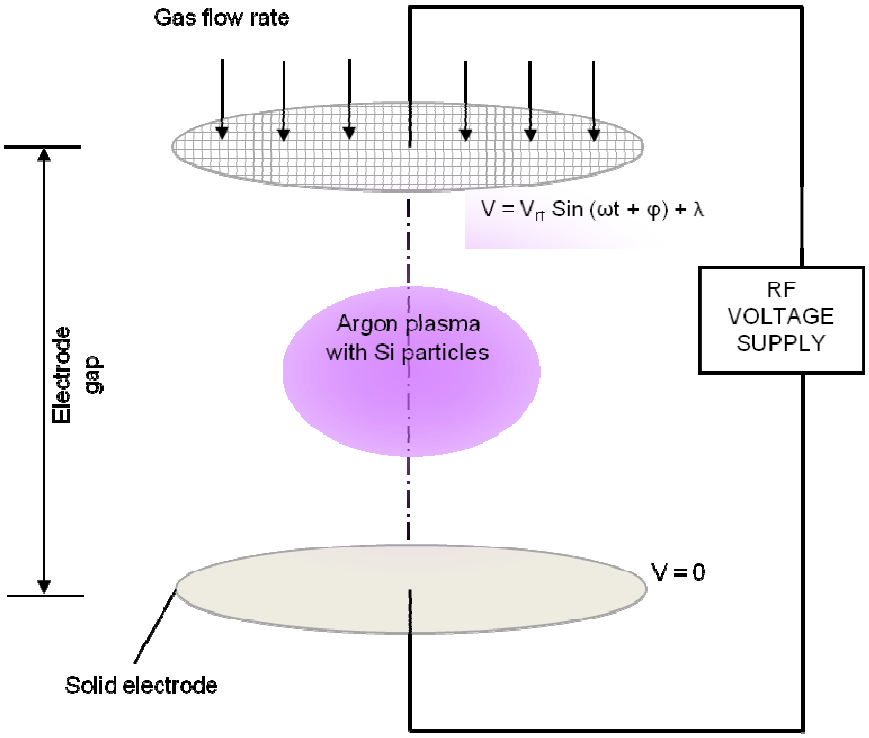


Figure 2.1: Model schematic

## 2.2 Numerical model equations

### 2.2.1 Fluid plasma model

The fluid plasma model consists of population balance equations for all the charged species (except charged dust particles) and electron energy equation for electron

temperature. The electric field is solved using Poisson's equation. These equations are coupled to each other therefore making the numerical model self consistent. Poisson's equation also contains the term for dust particle charge because we may have high density of dust particles and their charge may affect the electric field significantly. Poisson's equation for electric field can be written as:

$$\frac{d^2V}{dx^2} = -\frac{e}{\varepsilon_0}\left(\sum n_{j+} - \sum n_{j-} - Q_{NCP}\right), \tag{2.1}$$

where, $V$ is voltage, $n_{j+}$ is the density of positively charged species, $n_{j-}$ is the density of negatively charged species and $Q_{NCP}$ is the net charge on dust particles. Electric field can be calculated as:

$$E = -\frac{dV}{dx}. \tag{2.2}$$

The population balance equation for each charged species $j$ (electrons and ions) can be written as:

$$\frac{dn_j}{dt} + \frac{d\Gamma_j}{dx} = S_j, \tag{2.3}$$

where, $n_j$ and $\Gamma_j$ represent the charged species density and flux. $S_j$ represents the source and sink terms. Since the momentum equation for velocity is not solved; a drift diffusion approximation is used for the flux term. The flux term can be written as:

$$\Gamma_j = \mu_j n_j E - D_j \frac{dn_j}{dx}, \tag{2.4}$$

where, $\mu_j$, $D_j$ and $E$ are the mobility coefficient, diffusion coefficient and the electric field. Details about mobility and diffusion coefficients are discussed in section 2.2.4. For ions, electric field in above equation is replaced by an effective electric field because ions have momentum and cannot follow rapidly varying RF electric field. Relationship between the effective electric field and the actual electric field is given by following equation:

$$\frac{d\tilde{E}}{dt} = \frac{e}{\mu_j m_j}\left(E - \tilde{E}\right), \tag{2.5}$$

where $\tilde{E}$ is the effective electric field and $m_j$ is the mass of ions.

The source and sink term can be represented as:

$$S_j = \left(\dot{R}_P - \dot{R}_L\right)_{Reactions} + L_{P,j}, \tag{2.6}$$

where $\dot{R}_P$, $\dot{R}_L$ are the rate of production and rate of loss due to reactions. $L_P$ is the rate of loss of charged species to particles. Because of high mobility of electrons, dust particles are highly negatively charged and therefore it is assumed that the loss of negative ions due to attachment to dust particles is negligible. Negative ions have much lower mobility than electrons and therefore they rarely cross the potential of negatively charged particles. Expression for $L_P$ is following:

$$L_{P,j} = \sum_{Size}\sum_{Charge} N_{i,k}\nu_{j(i,k)}, \tag{2.7}$$

where $N_{i,k}$ is density of dust particle with size $i$ and charge $k$. $v_{j(i,k)}$ is the frequency of attachment of species j with the dust particle of size $i$ and charge $k$. Expression for frequency can be written as:

$$v_{j(i,k)} = \pi r_i^2 n_j \left(\frac{2E_j}{m_j}\right)^{\frac{1}{2}} \alpha_j \,, \tag{2.8}$$

where $r_i$, $E_j$ and $m_j$ are the dust particle radius, total kinetic energy of charged species j and mass of charged species j. The expression for $\alpha_j$ is following:

$$\alpha_j = \exp\left(\frac{-z_j e \Phi_{i,k}}{k_B T_j}\right) for\ z_j k\ \geq 0 \,, \tag{2.9 a}$$

$$\alpha_j = \exp\left(1 + \frac{-z_j e \Phi_{i,k}}{k_B T_j}\right) for\ z_j k < 0 \,, \tag{2.9 b}$$

$$\Phi_{i,k} = \frac{ke}{4\pi\varepsilon_0 r_i} \,, \tag{2.9 c}$$

where $z_j$ is the number of charges on species j, $k_B$ is the Boltzmann constant and $T_j$ is the temperature of species j.

The electron temperature is calculated by solving the electron energy density equation with the assumption of Maxwellian distribution of electron energy. Ions are considered to be at the gas temperature. Following is the equation for electron energy density:

$$\frac{d}{dt}\left(\frac{3}{2} n_e k_B T_e\right) + \frac{dq_e}{dx} = -e\Gamma_e E + S_q - \sum_{Size} \sum_{Charge} \left(N_{i,k} \nu_{e(i,k)} \Phi_{i,k}\right) \,, \tag{2.10}$$

where, $T_e$ is the electron temperature, $q_e$ is the electron energy flux and $S_q$ represents the loss of electron energy in electron impact collisions with heavy species (not including particles). Electron energy density flux can be represented as:

$$q_e = \frac{5}{2} k_B T_e \Gamma_e - \frac{5}{2} D_e n_e \frac{d}{dx}(k_B T_e), \tag{2.11}$$

where $\Gamma_e$ is the flux of electrons and is given by equation 2.4.

The equations are discretized using finite difference method. The Scharfetter Gummel method (48) was used for discretizing the flux term appearing in the population balance equation for charged species and the electron energy density equation. For the boundary conditions, electron concentration and negative ion concentrations are assumed to be zero at the electrode wall. Positive ions are assigned a zero concentration gradient at the wall. Electron temperature is assigned to be 0.5 eV at the walls. Lower electrode is grounded and upper electrode is RF powered.

### 2.2.2 Dust particle model

In the dust particle model, the aerosol general dynamics equation is solved for the spatiotemporal evolution of particle size and charge distribution. Aerosol general dynamics equation contains terms for particle charging by electron and ion attachment, size and charge dependent coagulation using image potentials, nanoparticle transport by diffusion, electric force, ion drag, gravity, neutral drag and thermophoresis. It also has terms for nucleation and surface growth rates.

Several methods have been proposed to solve aerosol general dynamics equation for particle size distribution and charge distribution (49,50). Most commonly used methods include the method of moments (51) and the sectional method (52). The method of moments involves solving for the first three moments of volume based particle size distribution (51). These methods are quite computationally efficient and relatively simple. However, their main disadvantage is that the form of the size distribution is specified in advance to have a closed set of equations. Therefore in cases where bimodal or trimodal distribution is important, these methods may not give correct results. Also, if we need to account for the dust particle charge then it might be complicated to use the method of moments.

The other approach, sectional method (52), is based on dividing the continuous particle size distribution into a number of sections based on a particular integral quantity that can either be volume, surface area or particle diameter. In the cases, where coagulation is important, volume based sectional methods have been the primary choice (52,53). Sectional methods are very good for modeling coagulation and mnucleation, however they suffer from numerical diffusion in cases where surface growth is important. Numerical diffusion is caused because of the underlying assumption that the particle size distribution is uniform within the section. Numerical diffusion might result in artificial broadening of the size distribution function in the cases where main growth mechanism is surface growth.

We have used the sectional approach to solve the general dynamics equation. Sections are spaced logarithmically by particle volume $v_p$, which means that a variable $u$ can be defined such that sections are evenly spaced with respect to that variable,

$$u = \ln v_p \, . \tag{2.12}$$

If volume at the lower edge of the $j^{th}$ section is $v_{p,j-1}$ then the volume at the upper edge of section can be determined by:

$$v_{p,j} = a v_{p,j-1} \, , \tag{2.13}$$

where $a$ is constant factor.

Average value of any size dependent property $q$(u) in $j^{th}$ section like particle mass, volume, surface area etc. can be written as:

$$\overline{q}_j = \frac{\int_{u_{j-1}}^{u_j} q(u) n(u) du}{\int_{u_{j-1}}^{u_j} n(u) du} \, , \tag{2.14}$$

where $n(u)$ is the particle size distribution function in the $j^{th}$ section. For simplicity, it is assumed that $n(u)$ is uniform within the section. As mentioned earlier, in the systems where surface growth has important contribution in growth, this assumption might result in artificial spreading of particle size distribution. Assuming $n(u)$ to be uniform in the section, expression for average value can be written in following way:

$$\overline{q}_j = \frac{\int_{u_{j-1}}^{u_j} q(u)du}{u_j - u_{j-1}}. \quad (2.15)$$

To accommodate for charge distribution, each size section can be divided into discrete charge states. Dust particle of the specific size (represented by $j^{th}$ size section) and the specific charge (represented by $k^{th}$ charge state) represents a species for which population balance equation has to be solved. Population balance equation for the number density of particles $N_{j,k}$, that lie in $j^{th}$ size section and $k^{th}$ charge state can be written as:

$$\frac{dN_{j,k}}{dt} + \frac{d\Gamma_{j,k}}{dx} = \left[\frac{dN_{j,k}}{dt}\right]_{nuc} + \left[\frac{dN_{j,k}}{dt}\right]_{coag} + \left[\frac{dN_{j,k}}{dt}\right]_{growth} + \left[\frac{dN_{j,k}}{dt}\right]_{charging}, \quad (2.16)$$

here, $\Gamma_{i,k}$ is dust particle flux which depends on size and charge and it includes particle transport by Brownian diffusion, neutral gas drag, ion drag, electrostatic forces, gravity and thermophoresis. It can be written as:

$$\Gamma_{j,k} = -D_j \nabla N_{j,k} + k\mu_j N_{j,k} E + \Gamma_F, \quad (2.17)$$

where $D_j$, $\mu_j$ and $\Gamma_F$ are the diffusion coefficient, mobility coefficients of particle in $j^{th}$ section and the flux term due to external forces respectively. Expression for diffusion coefficient is given in equation 1.1 in section 1.3.4.1. Mobility can be calculated from Einstein's relation:

$$D_j = \mu_j k_B T_{gas}. \quad (2.18)$$

$\Gamma_F$ can be expressed as:

$$\Gamma_F = (F_{ID} + F_G + F_{ND} + F_{TH}) \left(\frac{\mu_j}{e}\right) N_{j,k} \,, \tag{2.19}$$

where, $F_{ID}$, $F_G$, $F_{ND}$ and $F_{TH}$ are the forces due to ion drag, gravity, neutral drag and thermophoresis. These forces have been described in detail in section 1.3.

The terms on the right hand side of general dynamics equation represent rate of change of $N_{j,k}$ due, respectively, to nucleation, coagulation, surface growth and charging. The source term for nucleation is non zero only for the first size section. Therefore, it can be written as:

$$\left[\frac{dN_{j,k}}{dt}\right]_{nuc} = \delta_{j,1} J_k \,, \tag{2.20}$$

where $\delta_{j,1}$ is the Kronecker delta function and $J_k$ is the nucleation rate of particles of charge $k$.

Details of sectional representation of coagulation have been discussed in (52,53). Coagulation is considered between charged-charged, neutral-charged and neutral-neutral particles. Coagulation conserves particle mass and charge. Assuming that all collisions between particles result in their sticking to form a new particle, the rate of coagulation between two particles of size-charge class 1 and 2 can be written as:

$$R_{coag,1,2} = \beta_{1,2} n_1 n_2 \,, \tag{2.21}$$

where $n_1$ and $n_2$ are number densities of particles of the two size-charge classes, and $\beta_{1,2}$ is the charge dependent coagulation coefficient. Nanoparticles in low pressure plasmas lie in the free molecular regime which means that mean free path of gas molecules is much

larger than the dust particle radius. Therefore, the coagulation coefficient between two particles of volume $v_1$ (radius $r_1$) and $v_2$ (radius $r_2$) and charge $z_1$ and $z_2$ is given by following equation:

$$\beta_{1,2} = f(z_1, z_2, r_1, r_2) \times \left(\frac{3}{4\pi}\right)^{\frac{1}{6}} \left(\frac{6k_B T}{\rho}\right)^{\frac{1}{2}} \left(\frac{1}{v_1} + \frac{1}{v_2}\right)^{\frac{1}{2}} \left(v_1^{\frac{1}{3}} + v_2^{\frac{1}{3}}\right)^2, \tag{2.22}$$

where $\rho$, $k_B$ and T are the particle density, Boltzmann constant and gas temperature respectively. The factor $f(z_1,z_2,r_1,r_2)$ is defined as follows:

$$f(z_1,z_2,r_1,r_2) = \left\{ \begin{array}{cc} 1 & if\ z_1 = 0, z_2 = 0 \\ 1 - \dfrac{z_1 z_2 e^2}{4\pi\varepsilon_0 (r_1 + r_2) k_B T} & if\ z_1 z_2 < 0 \\ 0 & if\ z_1 z_2 > 0 \\ E_{image} & if\ z_1 \neq 0, z_2 = 0 \end{array} \right\}, \tag{2.23}$$

where $E_{\text{image}}$ is the enhancement in the collision rate between charged and uncharged particle due to image potentials. A detailed derivation of $E_{\text{image}}$ can be found in (54)**.** $E_{\text{image}}$ is given by following equation:

$$\begin{aligned} E_{image} \quad = \frac{1}{2} \int_0^1 \frac{1}{x^2} \frac{d}{dx} \left( x \frac{d\Phi(x)}{dx} \right) \times exp\left( \frac{x}{2} \frac{d\Phi(x)}{dx} - \Phi(x) \right) dx \\ + exp\left( \frac{1}{2} \frac{d\Phi(x)}{dx} |_{x=1} - \Phi(1) \right), \end{aligned} \tag{2.24}$$

$$x = \frac{r_1 + r_2}{r}, \tag{2.25}$$

where $r$ is the distance between the particles and $\Phi(x)$ is the inter-particle potential. Detailed description of $\Phi(x)$ can be found in (54)**.** In case of nanodusty plasma, coagulation between neutral and charged particles is dominated by coagulation between very small neutral particles and larger charged particles (24). For such systems, $\Phi(x)$ can be approximated by following expression:

$$\Phi(x) = \frac{aMx^2}{2(1-bx^2)}, \tag{2.26}$$

$$M = \frac{e^2}{4\pi\varepsilon_0 k_B T(r_1 + r_2)}, \tag{2.27}$$

$$a = \frac{\epsilon - 1}{\epsilon + 1} z_1^2 \left(1 - \frac{r_1}{r_1 + r_2}\right), \tag{2.28}$$

$$b = \left(\frac{\epsilon - 1}{\epsilon + 1}\right)^2 \left(\frac{r_1}{r_1 + r_2}\right)\left(1 - \frac{r_1}{r_1 + r_2}\right), \tag{2.29}$$

where, $\epsilon$ is the dielectric constant of the particles.

The equations for the sectional representation of coagulation term as it appears in the aerosol general dynamics equation become lengthy and therefore are skipped here. A detailed discussion is given in (52)**.**

In our model, we have used number conservation scheme proposed by (53) for the evaluation of surface growth term. According to this scheme surface growth rate can be presented as:

$$\left[\frac{dN_{j,k}}{dt}\right]_{growth} = \frac{\dot{B}_j V_j}{\bar{v}_{p,j}} + \frac{\dot{C_{j-1}} V_j}{\bar{v}_{p,j}} - \frac{\dot{C}_j V_j}{\bar{v}_{p,j}}, \tag{2.30}$$

where, $\dot{B}_j$ and $\dot{C}_j$ are, respectively, intra and intersectional growth coefficients (in units of $s^{-1}$). Intra and intersectional growth coefficients account for the fact that particles can either remain in the same section or can grow into the next section. $V_j$ is the particle volume concentration i.e. total volume of particle per unit volume of gas. $\bar{v}_{p,j}$ is the average particle volume of section *j*. Since surface growth does not affect particle charge, subscript *k* has been dropped in the description of surface growth.

The rate of volume addition to particles in section j can be written as:

$$\dot{B}_j V_j = \dot{N}_s v_m \bar{A}_{p,j} N_j , \tag{2.31}$$

where $\dot{N}_s$ is the rate of particle growth in terms of molecules added per unit particle surface area, $v_m$ is the molecular volume added to the particle, and $\bar{A}_{p,j}$ is the average particle surface area in section *j*, which can be calculated from equation (2.15). $\dot{N}_s$ can be calculated from chemistry model involving growth of particles by chemical reactions on their surface.

The intra and intersectional growth coefficients are related by,

$$\dot{C}_j = \dot{B}_j \frac{\bar{v}_{p,j+1}}{\bar{v}_{p,j+1} - \bar{v}_{p,j}} . \tag{2.32}$$

The term for particle charging in the general dynamics equation can be written as:

$$\left[\frac{dN_{i,k}}{dt}\right]_{charging} = v_{+(j,k-1)}N_{j,k-1} + v_{e(j,k+1)}N_{j,k+1} - \left(v_{+(j,k)} + v_{e(j,k)}\right)N_{j,k}\,, \quad (2.33)$$

where $v_{+(i,k)}$ and $v_{e(i,k)}$ are the electron and ion attachment frequencies to particles. It is assumed here that charging of dust particles is only due to ion and electron attachment and other charging processes like UV photodetachment and secondary electron emission are not being taken into account. Detailed expression for $v_{+\ (i,k)}$ and $v_{e(i,k)}$ are given by equation 2.9 in section 2.2.1**.** It is important to mention here that a maximum charge limit is imposed on the particles of a particular size. This limit is related to mutual Coulomb repulsion felt by electrons within the particle. Expression for maximum charge limit for $j^{th}$ size section $Z_{max,j}$ is taken from (55):

$$Z_{max,j} = -5.75 + \left[33.16 + 35.71\left(r_j + 0.23\right)\right]^{\frac{1}{2}}, r_j > 1.3\ nm \quad (2.35\ a)$$

$$Z_{max,j} = 1, r_j < 1.3\ nm\,, \quad (2.35\ b)$$

where, $r_j$ is the radius of size section $j$ in nanometer.

As mentioned earlier, particles are classified based on size and charge. Total number of particle classes considered is product of number of size sections and charge sections. In general, we have 140 size sections and 100 charge states so the total number of particle species considered is 14000. Therefore, sectional method is quite computation intensive, however, it enables us to get the spatiotemporal evolution of particle size and charge distribution. We use advanced computational techniques to make our computations more efficient. A discussion on computational aspects has been given in section 2.4.

General dynamics equation was discretized using the semi implicit finite difference scheme. The drift diffusion term was treated implicitly however the source and sink terms were treated explicitly. For charged particles, flux term was discretized using Scharfetter Gummel scheme (48). Density of neutral and negatively charged particles is assumed to be zero at the wall. For positively charged particles, concentration gradient is assumed to be zero at the wall. Pump loss and radial diffusion terms have been added to population balance equation for neutral particles. A detailed discussion on these terms is given in section 2.2.3.4

## 2.2.3 Chemistry model

In order to obtain self consistent nucleation and surface growth rate, a simplified chemistry model was used which is based on the detailed chemistry study by Girshick and coworkers (19,21). Bhandarkar et al (21) found that $Si_2H_5^-$ and $Si_2H_4^-$ are the main precursors in the pathways leading to particle formation. Therefore, in our simplified chemistry model, we have included silicon species containing only one silicon atom and we consider 34 reactions giving us the formation rate of species containing two silicon atoms.

### 2.2.3.1 Species included in the model

In argon-silane plasma, silane is a precursor gas which interacts with energetic electrons and gets dissociated into several reactive species. Therefore, in the current model, we have included silane and its products by electron impact collisions. These products include radicals like $SiH_2$, $SiH_3$ and atomic hydrogen. These reactive species containing one silicon atom undergo electron impact collisions and create important ionic species

like $SiH_2^-$ or $SiH_3^-$, which play an important role in particle formation. Apart from gas phase species, we also consider two surface species (SiH(S) and Si(S)) and their interactions with gas phase species. The surface species are silicon atoms on the surface of dust particles that either have H radical or dangling bond. Surface species are important for surface growth. However, rearrangement of surface species in the coagulation event has not been well understood. Therefore surface species are assumed to have fixed particle surface coverage and the relative abundances of SiH(S) and Si(S) is assumed to be (0.495:0.505) (56). Species considered have been described in table 2.1.

Table 2.1: chemical species considered in the model, S- surface species, B- bulk species

| Neutral species | Ions | Surface species |
|---|---|---|
| $SiH_4$, $SiH_3$, $SiH_2$, $H_2$, H, Ar, Ar* | e, $Ar^+$, $SiH_3^-$, $SiH_2^-$, $H_2^+$, $SiH_3^+$ | Si(S), SiH(S), Si(B) |

In the present model, 15 chemical species were considered to model silane chemistry in argon plasma. A sensitivity analysis was performed by Warthesen and Girshick (57) for 0D argon-silane plasma model with simulation condition being 117 mTorr pressure, 293 K gas temperature and 10 W power. They found that 84 species and 400 reactions have important contribution in nucleation chemistry. Although a detailed chemistry model will provide more accurate solutions for nucleation and surface growth rates, considering the computational expense and error involved in determining rate coefficients of various

reactions, we here use a simplified model. This simplified model can be easily extended to a more complex model in future as the code becomes more computationally efficient.

#### 2.2.3.2 Reactions included in model

The simplified chemistry mechanism considers 38 gas phase reactions (table 2.2) and 5 heterogeneous reactions on the dust particle surface (table 2.3). This reaction mechanism is based on the detailed chemistry model developed by Girshick and coworkers (19,21). The reaction rate constant (represented by $k$) for these reactions are presented in the Arrhenius form as follows:

$$k = AT^{\beta} \exp\left(\frac{-E_A}{RT}\right), \tag{2.36}$$

where $A$ is called the pre-exponential factor, $\beta$ is the temperature exponent, $E_A$ is the activation energy, $T$ is the temperature and $R$ is the gas constant. $A$, $\beta$ and $E_A$ are listed in table 2.1 along with the reactions. In the above equation, $T$ is the electron temperature if the reaction is electron impact reaction otherwise $T$ is the gas temperature.

In the reaction mechanism, we have electron impact reactions of silane. Silyl and silylene species are created in abundance by the electron impact dissociation of silane. These species undergo electron impact collisions and create further species. Apart from electron impact reactions, we have neutral-neutral reactions and ion-neutral reactions. It has been found that ion-neutral reactions are important in particle formation mechanism. Surface reactions are considered to model surface growth. For surface reactions, sticking coefficient is given in table 2.3 along with reactions. For the simulations conditions for

low pressure plasmas, the reactions considered here have much higher rate constants for forward reactions than the same for reverse reactions. Therefore reactions are considered irreversible. A detailed discussion of reactions rates for the reactions listed in table 2.2 and sticking coefficients for reactions listed in table 2.3 is given in (21).

Table 2.2: Chemical reaction mechanism

| **Reaction** | **A($cm^3s^{-1}mol^{-1}$)** | **β** | **$E_A$(cal/mol)** | **Ref.** |
|---|---|---|---|---|
| 1. $Ar + e \rightarrow Ar^+ + e$ | $4.25 \times 10^{13}$ | 0.6 | 371860 | (58) |
| 2. $SiH_4 + e \rightarrow SiH_3 + H + e$ | $1.1 \times 10^{21}$ | -1.0 | 245430 | (58) |
| 3. $SiH_4 + e \rightarrow SiH_2 + 2H + e$ | $5.4 \times 10^{21}$ | -1.0 | 245430 | (58) |
| 4. $SiH_4 + e \rightarrow SiH_3^- + H$ | $2.269 \times 10^{21}$ | -1.627 | 190540 | (56) |
| 5. $SiH_4 + e \rightarrow SiH_2^- + 2H$ | $2.269 \times 10^{21}$ | -1.627 | 190540 | (56) |
| 6. $SiH_4 + e \rightarrow SiH_3^+ + H + 2e$ | $1.51 \times 10^{32}$ | -2.93 | 553910 | (56) |
| 7. $SiH_3 + e \rightarrow SiH_2^- + H$ | $3.44 \times 10^{15}$ | -0.5 | 0.0 | (56) |
| 8. $SiH_3 + e \rightarrow SiH_3^+ + 2e$ | $1.36 \times 10^{12}$ | 0.9 | 188403 | (58) |
| 9. $SiH_3^- + e \rightarrow SiH_3 + 2e$ | $1.9 \times 10^{14}$ | 0.5 | 33070 | (59) |
| 10. $SiH_2^- + e \rightarrow SiH_2 + 2e$ | $1.9 \times 10^{14}$ | 0.9 | 27300 | (59) |
| 11. $H_2 + e \rightarrow 2H + e$ | $1.02 \times 10^{16}$ | 0.0 | 238356 | (58) |
| 12. $H_2 + e \rightarrow H_2^+ + 2e$ | $8.02 \times 10^{10}$ | 1.1 | 392590 | (58) |
| 13. $SiH_3 + SiH_3 \rightarrow SiH_2 + SiH_4$ | $1.8 \times 10^{13}$ | 0.0 | 0.0 | (58) |
| 14. $SiH_4 + SiH_3 \rightarrow Si_2H_5 + H_2$ | $1.77 \times 10^{12}$ | 0.0 | 4400 | (58) |
| 15. $SiH_2 + H_2 \rightarrow SiH_4$ | $1.2 \times 10^{11}$ | 0.0 | 0.0 | (60) |
| 16. $SiH_2 \rightarrow Si + H_2$ | $9.1 \times 10^{20}$ | 1.76 | 38241 | (61) |
| 17. $SiH_4 + H \rightarrow H_2 + SiH_3$ | $1.47 \times 10^{8}$ | 1.9 | 2190 | (58) |
| 18. $SiH_2 + SiH_2 \rightarrow Si_2H_2 + H_2$ | $6.51 \times 10^{14}$ | 0.0 | 0.0 | (58) |
| 19. $SiH_2 + H \rightarrow SiH + H_2$ | $1.39 \times 10^{13}$ | 0.0 | 0.0 | (58) |
| 20. $SiH_3 \rightarrow SiH + H_2$ | $1.98 \times 10^{26}$ | -3.1 | 44770 | (58) |
| 21. $SiH_3 + H \rightarrow SiH_2 + H_2$ | $1.5 \times 10^{13}$ | 0.0 | 2500 | (58) |

| | | | | |
|---|---|---|---|---|
| 22. $SiH_2^- + H_2^+ \rightarrow SiH_2 + H_2$ | $3.34 \times 10^{18}$ | -0.5 | 0.0 | (56) |
| 23. $SiH_3^- + H_2^+ \rightarrow SiH_3 + H_2$ | $3.34 \times 10^{18}$ | -0.5 | 0.0 | (56) |
| 24. $SiH_3^- + SiH_3 \rightarrow Si_2H_4^- + H_2$ | $1.27 \times 10^{10}$ | 0.0 | 0.0 | (56) |
| 25. $SiH_3^- + SiH_3^+ \rightarrow Si_2H_6$ | $1.27 \times 10^{10}$ | 0.0 | 0.0 | (56) |
| 26. $SiH_2^- + SiH_4 \rightarrow Si_2H_4^- + H_2$ | $1.27 \times 10^{10}$ | 0.0 | 0.0 | (56) |
| 27. $SiH_2^- + SiH_3 \rightarrow SiH_2 + SiH_3^-$ | $1.27 \times 10^{10}$ | 0.0 | 0.0 | (56) |
| 28. $SiH_3^- + SiH_2 \rightarrow Si_2H_3^- + H_2$ | $1.27 \times 10^{10}$ | 0.0 | 0.0 | (56) |
| 29. $SiH_2^- + SiH_3^+ \rightarrow Si_2H_5$ | $1.27 \times 10^{10}$ | 0.0 | 0.0 | (56) |
| 30. $SiH_2^- + Ar^+ \rightarrow SiH_2 + Ar$ | $8.64 \times 10^{17}$ | -0.5 | 0.0 | (59) |
| 31. $SiH_3^- + Ar^+ \rightarrow SiH_3 + Ar$ | $8.64 \times 10^{17}$ | -0.5 | 0.0 | (59) |
| 32. $Ar + e \rightarrow Ar^* + e$ | $7.04 \times 10^{15}$ | 0.0 | 283662 | (58) |
| 33. $Ar^* + e \rightarrow Ar^+ + 2e$ | $7.52 \times 10^{16}$ | 0.0 | 124191 | (58) |
| 34. $Ar^* + SiH_4 \rightarrow SiH_3 + H + Ar$ | $8.43 \times 10^{13}$ | 0.0 | 0.0 | (62) |
| 35.$Ar^* + SiH_4 \rightarrow SiH_2 + 2H + Ar$ | $1.56 \times 10^{14}$ | 0.0 | 0.0 | (62) |
| 36.$Ar^* + SiH_3 \rightarrow SiH_2 + H + Ar$ | $6.0 \times 10^{13}$ | 0.0 | 0.0 | (62) |
| 37.$Ar^* + SiH_2 \rightarrow SiH + H + Ar$ | $6.0 \times 10^{13}$ | 0.0 | 0.0 | (62) |
| 38.$Ar^* + H_2 \rightarrow 2H + Ar$ | $4.2 \times 10^{13}$ | 0.0 | 0.0 | (62) |

Table 2.3: Surface reaction mechanism

| **Surface reaction mechanism** | **Sticking coefficient** | **Ref** |
|---|---|---|
| 1. $SiH_4 + Si(S) \rightarrow 2SiH(S) + Si(B) + H_2$ | $1.0 \times 10^{-5}$ | (63) |
| 2. $SiH_2 \rightarrow Si(B) + H_2$ | 1.0 | (59) |
| 3. $SiH_3 + Si(S) \rightarrow SiH(S) + Si(B) + H_2$ | 0.09 | (59) |
| 4. $SiH_3^+ + Si(S) - Z_P\, e \rightarrow SiH(S) + Si(B) + H_2 - (Z_P - 1)e$ | 1.0 | Eq 2.8 |
| 5. $Ar^* + Particle \rightarrow Ar + Particle$ | 1.0 | Eq 2.37 |

#### 2.2.3.3 Nucleation and surface growth rate

The nucleation rate is simply assumed to equal the rate of formation of anionic silicon species containing two silicon atoms because they are considered to be the precursor of nucleation pathways leading to particle formation. Surface growth can occur either by heterogeneous reactions between radicals and the surface species present on particle surface or by the silyl or silylene ions being deposited over dust particles as a result of Coulomb attraction. The reaction rate of ion deposition on particles is calculated by equations (2.7, 2.8 and 2.9). For the reaction rate of heterogeneous reactions between radicals and surface species on particle surface, the collision rate between gas phase species and particles is calculated considering the effect of induced dipole attraction. The collision rate is then multiplied by the reaction probability which consists of sticking coefficient and relative abundance of surface species. Expression of rate constant $\boldsymbol{k_{sg}}$ (for the reaction between radicals and dust particles) can be written as:

$$\boldsymbol{k_{sg}} = \boldsymbol{E_{Dipole}}\,\boldsymbol{\sigma} \times \boldsymbol{x_s} \times \sum_{\mathrm{j}} \left(\frac{3}{4\pi}\right)^{\frac{1}{6}} \left(\frac{6k_B T}{\rho}\right)^{\frac{1}{2}} \left(\frac{1}{v_1} + \frac{1}{v_{\mathrm{j}}}\right)^{\frac{1}{2}} \left(v_1^{\frac{1}{3}} + v_{\mathrm{j}}^{\frac{1}{3}}\right)^2 N_j \,, \tag{2.37}$$

Where $E_{\mathrm{Dipole}}$ is the enhancement due to induced dipole attraction, $\boldsymbol{\sigma}$ is sticking coefficient, $\boldsymbol{x_s}$ is the relative surface abundance of the gas phase species SiH(S) and Si(S), $v_1$ is the volume of gas phase species and $v_{\mathrm{j}}$ is the volume of dust particle in section j, T is the gas temperature and $\rho$ is density of the material which is silicon in our case. $E_{\mathrm{Dipole}}$ is calculated in the same way as $E_{\mathrm{image}}$ by equations (2.24 to 2.29). Units of

$\boldsymbol{k_{sg}}$ are $s^{-1}$ and it needs to be multiplied by the concentration of gas phase species to get the rate of production of Si(B) on particle surface.

#### 2.2.3.4 Population balance equation for neutral species

As mentioned earlier, charged as well as neutral species are considered in the chemistry model. Population balance equation for all the charged species is solved with Poisson's equation in plasma module and the detailed discussion is given in section 2.1. In the neutral chemistry module, we solve balance equation for only neutral species. Although our calculations are 1D along the axial direction and we assume radial symmetry, in order to account radial effects, we add an approximate loss term for radial diffusion. We also consider a term for pump losses. Radial diffusion and pump loss terms are only used for neutral species. Charged species are under the influence of electric field therefore radial diffusion and pump loss can be neglected for them. Population balance equation for neutrals is following:

$$\frac{dN_j}{dt} - D_j\frac{d^2N_j}{dx^2} + \frac{d(N_j\vec{V}_{gas})}{dx} = \left(\dot{R}_{Pj} - \dot{R}_{Lj}\right)_{Reactions} + \dot{L}_{RD} + \dot{L}_{Pump}\,, \qquad (2.38)$$

where, $N_j$ is the concentration of neutral species $j$, $D_j$ is the diffusion coefficient, $\dot{R}_{Pj}$ and $\dot{R}_{Lj}$ are the rate of production and rate of loss, $\dot{L}_{RD}$ is the term for loss due to radial diffusion and $\dot{L}_{Pump}$ is the term for pump loss. The radial loss term can be written as (64):

$$\dot{L}_{RD} = -\frac{D_j}{\lambda^2}N_j\,, \qquad (2.39)$$

$$\lambda = \frac{R}{2.4}, \tag{2.40}$$

where, $R$ is the characteristic radial dimension of the cylindrical chamber. The pump loss term can be written as (65):

$$\dot{L}_{Pump} = -\frac{N_j}{T_{Res}}, \tag{2.41}$$

where, $T_{Res}$ is the residence time of species in the chamber. $T_{Res}$ is calculated iteratively such that the total pressure in the system is maintained and is same for all the neutral species.

The balance equation is discretized using finite difference scheme. Since, neutral species are not affected by variable electric field so the diffusion term was discretized using central finite difference method. It was assumed that the change in gas mixture density is not enough to change the velocity so stagnation flow profile was assumed for the mixture velocity. Ideally, a continuity equation and the momentum equation should be solved for the mixture density and velocity. For the boundary conditions, concentration gradient at the wall was assumed to be zero for all the neutral species except silane. For silane, concentration at the showerhead electrode was fixed.

## 2.2.4 Transport properties

### 2.2.4.1 Charged species

The electron and argon ion mobility were taken from (66). Mobility of silyl and silylene ions was calculated by using the Langevin model described in Perrin et al (59). Expression for the mobility can be written as:

$$\mu_i P = 38.7T(\alpha m_r)^{-1/2}\ cm^2.Torr.V^{-1}s^{-1}\ , \tag{2.42}$$

where, $\mu_i$ is the ion mobility and $P$ is the pressure in Torr, $\alpha$ is the polarizability in $\dot{A}^3$ and $m_r$ is the reduced mass in a.m.u.. Expression for $m_r$ is following:

$$m_r = \frac{m.m_B}{m + m_B}\ , \tag{2.43}$$

where, $m$ is the mass of species in a.m.u. and $m_B$ is mass of non polar background gas in a.m.u. Expression for polarizability for charged species containing n silicon atoms can be written as (59):

$$\alpha = 4.62(0.2 + 0.8n), \dot{A}^3\ , for\ Si_nH_m\ , \tag{2.44}$$

$$\alpha = 0.805, \dot{A}^3, for\ H_2\ . \tag{2.45}$$

The diffusion coefficient is calculated using the Einstein relationship given by equation 2.18.

#### 2.2.4.2 Neutral species

The diffusion coefficient for neutral species can be calculated by following expression:

$$D_{ij} = \frac{3}{16}\frac{\left(4\pi k_B T/2m_{ij}\right)^{1/2}}{N\pi{\sigma_{ij}}^2\Omega_D(T^*)}\ , \tag{2.46}$$

where, $D_{ij}$ is the diffusion coefficient of species $i$, in the background gas $j$. Background gas is argon. $N$ is total gas density, $T$ is the gas temperature in K, $\sigma_{ij}$ is the arithmetic mean of Lennard Jones parameters for species $i$ and background gas $j$. Lennard Jones parameter for several gases is given in table 9 in Perrin et al (59). $m_{ij}$ is the reduced mass given by equation (2.43). T* = T/$\varepsilon_{ij}$ with $\varepsilon_{ij} = \sqrt{\varepsilon_i \times \varepsilon_j}$, $\varepsilon$ is the second Lennard Jones parameter for species $i$ and background gas $j$ and is listed in table 9 of Perrin et al (59). $\Omega_D(T^*)$ can be calculated from following equation:

$$\Omega_D(T^*) = \frac{A}{T^{*B}} + \frac{C}{e^{D\times T^*}} + \frac{E}{e^{F\times T^*}} + \frac{G}{e^{H\times T^*}} \qquad (2.47)$$

where, A=1.06036, B=0.15610, C=0.19300, D=0.47635, E=1.03587, F=1.52996, G=1.76474, and H=3.89411.

## 2.3 Time slicing

Dust particles, neutral chemical species and charged chemical species have different time scales. In the RF dusty plasma, charged species respond to RF electric field therefore the time scale of change in their properties is much shorter than the time scale of change in the dust particle properties. Similarly, dust particles are charged by electrons and ions and respond to time averaged electric field. The time scale of change in the dust particles properties is shorter than that of the neutral species properties because of dust particle charging by electrons. Therefore, the coupled behavior of plasma, chemical species and dust particles was self consistently modeled in a three step process to make computations more efficient. This technique of computing different processes on the basis of their time scales is called time slicing.

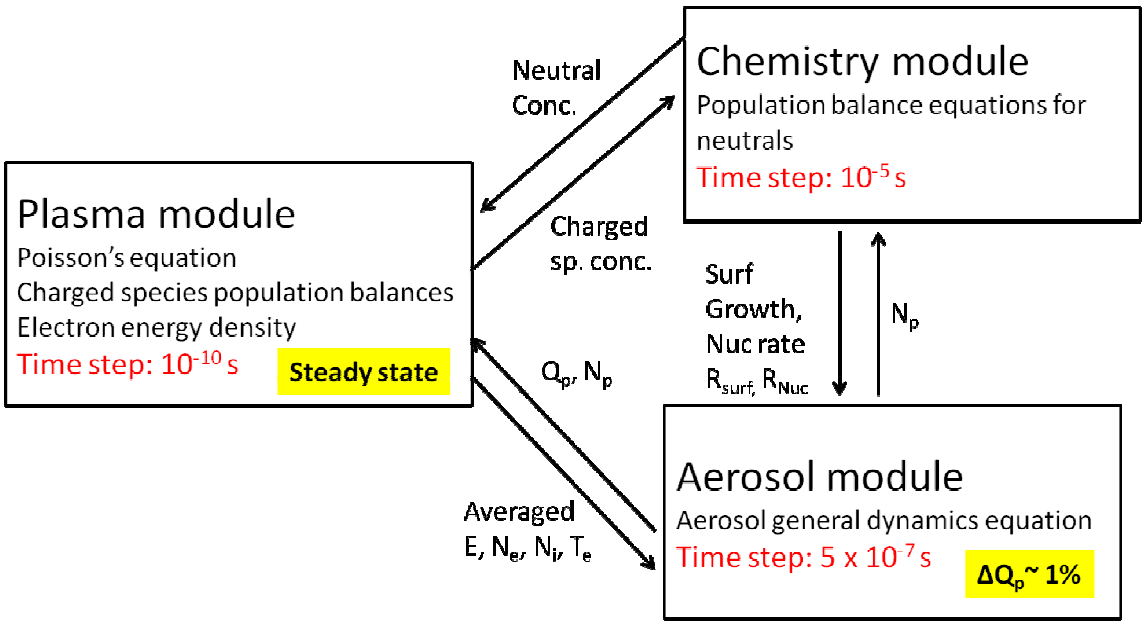


Figure 2.2: Time slicing scheme

A schematic of time slicing scheme is shown in figure 2.2. Plasma is calculated at a time step of $10^{-10}$ s until a steady state is reached. Model then starts to calculate dust particles at a time step of 5 x $10^{-7}$ s until the dust particle charge concentration at every location is changed by 1% which is assumed to be enough to affect the electric field. Once the dust particle charge concentration is changed by 1%, model again calculates plasma to update electric field, electron temperature and charged species densities. Every 20 dust particle time steps, neutral species are calculated implying a time step of $10^{-5}$ s.

## 2.4 Computational aspects

### 2.4.1 Parallel processing

Parallel processing is a well known tool for increasing the speed of a serial code. The numerical model for dusty plasma simulation developed is highly computation intensive

and it takes 4000 hrs of CPU time per 1 second of plasma simulation on SGI Altix machine (24). However, by implementation of parallel processing, the CPU time reduced to 40 hrs per 1 second of plasma simulation on SGI Altix XE 1300 cluster and 30 hrs per 1 second of plasma simulation on Intel 6-core Xeon X5670 2.93 GHz machine with 24 GB RAM. Message passing interface (MPI) and open multi processing (OpenMP) are two well known techniques for implementation of parallel processing (67). A brief description of parallel processing techniques and their implementation in the numerical model is presented in the following sections.

#### 2.4.1.1 Message passing interface (MPI)

MPI is a tool for programming parallel computers with distributed memory. Distributed memory refers to a system where different processors have a local memory which is not shared. Message passing is a way to set up processes that have local memory and they communicate with each other by sending and receiving messages. Message passing interface (MPI) is a library which collects the best features of many message passing models and gives a set of simple commands which can be incorporated in the FORTRAN code to simultaneously execute it on multiple processors with efficient message passing (68).

In the numerical model, MPI was first implemented such that calculations related to each spatial grid point were carried out on a separate processor. It was found that MPI was efficient for coagulation calculations but it was highly inefficient for solving equations simultaneously by tridiagonal matrix algorithm (Thomas algorithm, TDMA). TDMA involves frequent communications among processors so the time taken in

communications was more than the time taken for calculations which resulted in poor efficiency. To overcome this problem, MPI was used to perform all other calculations except solving the equations. Equations were solved on a single processor and the outcome was broadcast to all the other processors to carry out other calculations.

#### 2.4.1.2 Open multi processing (OpenMP)

OpenMP is used for programming multi core machine with shared memory, systems. When different computers have a common global memory i.e. change made by one processor in a variable will be visible to all other processors without any message passing, then it is called shared memory system. Similar to MPI, OpenMP is also a library or a set of commands that can be added to a serial code to share the work amongst different processors having access to a shared memory (69). In this case it is not needed to set up message passing among processors but one has to be careful that different processors should not access the same memory location (a variable occupies a particular memory location) simultaneously.

OpenMP was used to increase the efficiency of coagulation subroutine by computing the size sections simultaneously on multi core processors. Work was divided in a way that a set of size sections was calculated on a specific processor. By doing so, all the big arrays were shared because every processor was allowed to access only its own set of size sections and therefore there was no overlapping of memory access. OpenMP directives were used to divide work dynamically so that processor wait times were reduced. The code was tested for 8 OpenMP cores, 16 OpenMP cores and 24 OpenMP cores. It was

found that speed up does not increase with the increase in number of cores. Generally, speed up per increase in number of cores depends on amount of work per processor.

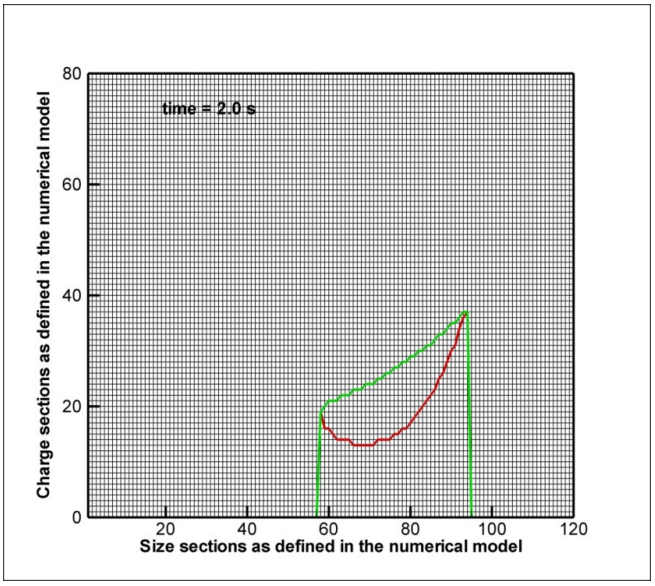


Figure 2.3: Each rectangle represents a class of particles having particular size and charge. All the classes which lie within the leaf shape area are populated with particles while the rest all are empty.

### 2.4.1.3 Computational savings in coagulation implementation

As discussed in the section of numerical model, aerosol general dynamics equation is solved using sectional model. We have 120 – 140 size sections and 80 – 100 charge sections. Particles are classified based on particular size and charge. Therefore, we have 120 x 80 or 140 x 100 classes of particles. In the ideal case, we need to solve aerosol general dynamics equation for all these classes which is very computation intensive. It was observed from results of our numerical model that only a few classes are populated (concentration > 1) at a particular time. Figure 2.3 shows the populated classes in calculations at 2.0 s for the case with 100 mTorr pressure, 300 K gas temperature and 100 V RF voltage amplitude. Figure 2.3 shows that out of 80 x 120 classes (one block

corresponds to each class) only those classes which lie within the leaf shape area are populated at 2.0 s. The classes which are not populated are completely removed from the coagulation calculations to make computations more efficient.

## 2.5 Summary

A self consistent numerical model is presented for the spatiotemporal behavior of particle size and charge distribution in argon-silane plasma. Numerical model consists of three modules namely fluid plasma module, dust particle module and neutral chemistry module. These three modules are self consistently coupled and are calculated at different time steps to make calculation more efficient. Poisson's equation and the population balance equations for charged species are solved in plasma module along with electron energy density equation. Population balance equations for neutral species are solved in chemistry module. Aerosol general dynamics equation is solved in dust particle module using sectional methods for particle size and charge distribution. Aerosol general dynamics equation contains terms for coagulation, particle charging, particle transport, nucleation and surface growth. The nucleation and surface growth rates are self consistently calculated from charged and neutral species chemistry. This numerical model is computationally expensive. Parallel processing techniques like MPI and OpenMP were used to make the computations faster. Also, it was found that calculations in coagulation can be reduced by selective taking out particle classes which have concentrations lower than unity.

# Chapter 3: Spatiotemporal evolution of particle size and charge distribution

Plasmas in which nanoparticles nucleate and grow are very important in the industry as well as the laboratory. Such chemically reactive plasmas are used for thin film deposition over wafers. Particles formed within the plasma may deposit over the thin film and therefore reduce the yield of deposition process. In a different application, such chemically reactive plasmas are used for the synthesis of nanoparticles for optoelectronic applications. In one application, the dust particles are unwanted and need to be removed. In the other application, nanoparticles are deliberately formed within the plasma and control of their size and morphology is desired. To address the issues related to both the applications, it is important to understand the formation, growth, charging and dynamics of these particles within the plasma.

There has been significant experimental and numerical research to understand the physics of dusty plasmas. Laser light scattering experiments performed by Bouchule and coworkers (7,70,71) at GREMI demonstrate important information on particle dynamics, growth and density. Similarly, mass spectrometry experiments performed by Howling and Hollenstein (16) and laser spectroscopy experiment performed by Kawasaki et al (18) reveal important information on particle formation mechanism and the role of various species in nucleation and growth chemistry. However, these experiments have limitations. For example, it is difficult to detect particles that are less than 20 nm in size through laser light scattering. Similarly, mass spectrometry experiments and laser spectroscopy are invasive diagnostic techniques involving application of electro-magnetic

fields which may change the plasma properties and therefore chemistry. Therefore, it is important to have a numerical model which simulates the formation, dynamics, growth and charging of dust particles in the plasma.

Most of the numerical models of plasmas are either not self consistent or they assume that the particle size distribution is monodisperse. Dusty plasmas involve a large number of physically and chemically interacting phenomena and therefore are difficult to model (40). Monodisperse models offer a reasonable and computationally inexpensive approach for self consistently modeling the systems that contain micron size particles. However, in the chemically reactive systems, particle nucleation and growth occurs over a period of time resulting in a polydisperse particle size distribution. Particle size is generally in nanometer range and therefore as a result of stochastic charging, particles of a particular size may have charge distribution rather than every particle having same charge. In such systems, where particles nucleate and grow, several important phenomena depend on particle size and charge distribution. For example, the nature of coagulation and particle transport is strongly influenced by both size and charge distribution of particles. Since particles and plasma are strongly coupled to each other, therefore it is important to account for particle size and charge distribution and its effect on several interacting phenomena self consistently.

Several researchers have used sectional methods for modeling dust particle size distribution in nanodusty plasmas. A detailed description of sectional methods has been given in Chapter 2 section 2.2.2. Kortshagen and Bhandarkar (46) used 0D sectional methods to study coagulation in dusty plasmas. They also accounted for particle charge

distribution by specifying discrete charge states for each size section and considered charge dependent coagulation. Kim et al (72) used a 0D discrete sectional model for size distribution and Gaussian charge distribution to study the particle growth by coagulation. Both of the above mentioned models were 0D and therefore neglected particle transport. The main aim of above mentioned references was to study coagulation. Bhandarkar et al (21) developed a detailed model for particle nucleation and growth chemistry. Detailed chemistry model was coupled to aerosol sectional model and plasma model. Charge distribution was modeled in the same way as in Kortshagen and Bhandarkar (46).

De Bleecker et al (47) used a sectional method to simulate particle dynamics in argon silane plasma. They used a modified version of chemistry mechanism described in Bhandarkar et al (21). Their model was 1D and includes particle transport. However, they do not account for particle charge distribution and charge dependent coagulation. Girshick and coworkers (23,24) used sectional method to model dusty argon plasma containing silicon nanoparticles. The model was self consistently coupled to a fluid plasma model. In their model, particle formation chemistry was not included rather nucleation and surface growth rates were treated as input parameters. Values of nucleation and surface growth rates were taken from the detailed chemistry study by Bhandarkar et al (21). Charge distributions were calculated within each section and coagulation was considered charge dependent with image potentials on neutrals. The spatiotemporal evolution of particle size and charge distribution was calculated and the effect of coagulation on growth mechanism was discussed.

In this chapter, a detailed description of spatiotemporal evolution of particle size and charge distribution is presented and it is emphasized that the consideration of polydispersity is important to understand the physics behind several interacting phenomena in dusty plasmas. It has been discussed that the nature of coagulation and particle transport is significantly influenced by the polydispersity in size and charge distribution.

## 3.1 Numerical model and assumptions

Numerical model is described in detail in chapter 2 and is an extension of model developed by Girshick and coworkers (23,24). For simplicity, chemistry model is not included in the simulations presented here. In this chapter, nucleation and surface growth rates are treated as input parameters. It was found by several researchers (10,21,24) that negative ions are the main precursors in particle formation. These negative ions are trapped within the sheath boundaries. Therefore, it is assumed that nucleation and surface growth occurs in a chemically active zone. Chemically active zone is the region outside the sheath boundaries. Sheath boundaries are defined as the location where the total negative charge lies 5% below the total positive charge. There is a competition between nucleation and surface growth for active species generated by plasma chemistry. To model this competition in qualitative way, it is assumed that silicon nanoparticles of diameter 0.75 nm are formed by gas-phase nucleation where total surface area of particles is less than a particular value $1.8 \times 10^{9}$ $nm^2cm^{-3}$ and surface growth occurs where particle nucleation is quenched. The nucleation rate is assumed to be $10^{12}$ $cm^{-3}s^{-1}$ and the surface

growth rate is assumed to equal 12 nm/s. These values are based on the detailed chemistry model developed by Bhandarkar et al (21).

System modeled corresponds to the experiments at GREMI, University of Orleans which involved 13.56 MHz capacitive RF argon-silane (30:1) plasma at a pressure of 17 Pa. Electrode gap was 4 cm with top electrode being powered and lower electrode was grounded. The applied RF voltage is assumed to be 55 V with DC self bias of -20 V. Gas flows through the top electrode of radius 12 cm and with a flow rate of 31 sccm. Bottom electrode is considered to be solid resulting in stagnation flow profile for the gas flow. It was mentioned earlier that the numerical model is 1D. Since the gap between electrodes is small compared to the electrode diameter, it was assumed that radial effects are negligible and calculations are performed in the axial direction.

## 3.2 Numerical simulation results

Spatiotemporal behavior of dusty plasma is explained in four different cases. These cases correspond to a particular time after the plasma was switched on and the particle formation was started. Four different cases considered correspond to 100 ms, 1s, 5s – 6s and 11 s after the plasma was switched on.

### 3.2.1 Case 1: t = 100 ms

Figures 3.1 shows a snapshots of particle size distribution function. In this figure, x axis shows the distance from lower electrode, y axis shows the particle diameter in nanometer and the colored contours represent the particle size distribution function $dN/d(\log(d_P))$ at 100 ms. White lines represent average negative charge on particles. At 0.1 s (figure 3.1),

particles are small (diameter range from 0.75 to 2.5 nm) and they are either neutral or have unit positive or negative charge. Negatively charged particles are trapped in the center whereas neutral and positive particles tend to diffuse towards the electrodes. The trapped particles continue to grow by surface growth and coagulation.

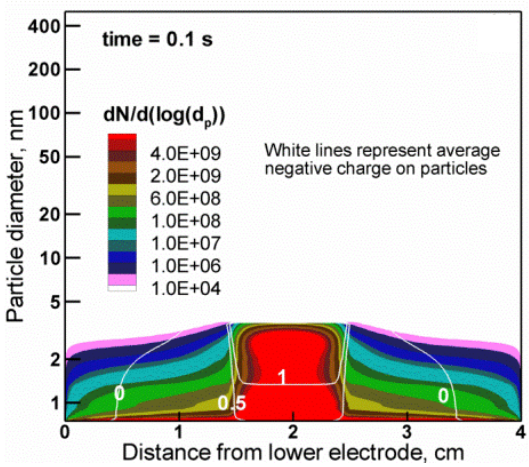


Figure 3.1: Particle size distribution and average particle charge at t=0.1 s

Figure 3.2 (a) shows the profile of positive, negative and neutral particles, and figure 3.2 (b) shows the profile of electron density, ion density and net negative charge on particles density at 100 ms. In figure 3.2 (a), presence of the neutral, negative and positive particles is due to stochastic charging. Because the electron mobility is much higher than the ion mobility, therefore concentration of negatively charged particles is much higher than the positively charged particle. At this instant, most of the negative charge is being carried by dust particles and ion density closely follows the particle density to maintain quasineutrality (figure 3.2 (b)). It should be mentioned that in the numerical model, Poisson's equation is solved for the electric field. Poisson's equation contains the term for particle charge. Poisson's equation by itself takes care of quasineutrality and no

additional condition was imposed for the quasineutrality. Since charged dust particles play a significant role in modification of electric field therefore the dust particles and plasma are strongly coupled to each other.

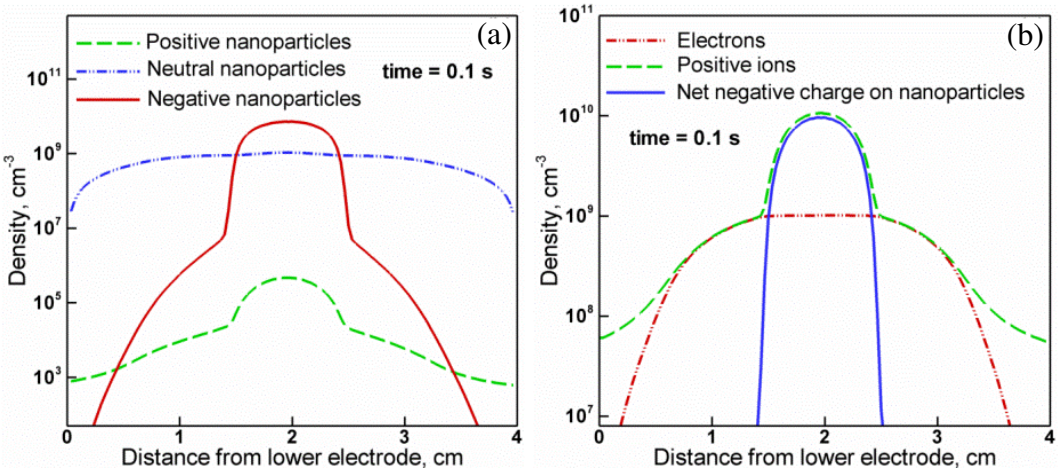


Figure 3.2: Spatial profiles of a) particle density and b) charge carrier density at 0.1 s

It is clear from figure 3.1 and 3.2 that dust particle distribution and charge carrier densities are symmetric at this moment. Although the neutral drag force and gravity are present, they are proportional to particle diameter and therefore their magnitude is small in comparison to the electric force and the ion drag force.

### 3.2.2 Case 2: t = 1 s

It was mentioned earlier that the sectional method is used for modeling particle size and charge distributions. Sectional methods are quite computation intensive but they enable us to get the spatiotemporal evolution of particle size and charge distribution function. We are interested in particle size and charge distributions because dust particles may be far from monodisperse.

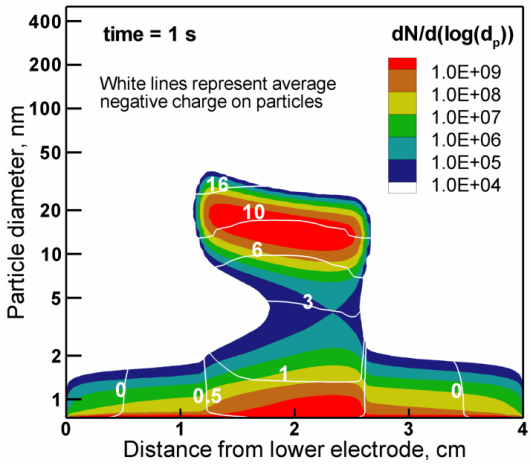


Figure 3.3: Particle size distribution and average particle charge at t = 1 s

Figure 3.3 shows the particle size distribution function and average negative charge on particles at 1 s. It is clear from the figure 3.3 that dust particles are not monodisperse. Deviation from monodispersity is because of ongoing nucleation, charging, diffusion, surface growth and coagulation. Freshly nucleated particles are positive, negative or neutral. Positive and neutral particles are lost to walls while the negatively charged particles are trapped due to electric force. Negatively charged small particles may get neutralized and diffuse to wall or may get lost by coagulating with larger particles. Particles are stably trapped once they are big enough and carry multiple negative charges. Therefore, two separate populations are formed, one is the freshly nucleated small particles and other is the population of large stably trapped negatively charged particles.

Figure 3.4 (a) shows the histogram of particle size distribution at 2 cm away from lower electrode. Size distribution is bimodal with modal diameters being 0.75 nm and 14.8 nm. Charge distribution on for these modal diameters is shown in figure 3.4 (b). Small

particles have +1, -1 or 0 charges. Concentration of neutral and negative particles is

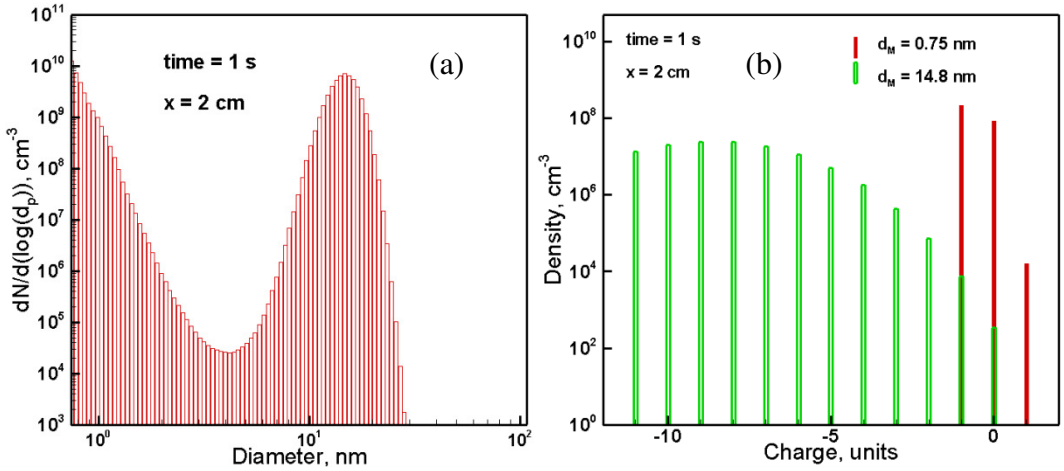


Figure 3.4: Nanoparticle size and charge distribution at midplane of discharge at t = 1 s; (a) Particle size distribution with each bar representing one numerical section; (b) charge distributions for the sections at the two modes of the size distributions, corresponding to diameters of 0.75 and 14.8 nm

comparable because of stochastic nature of charging. Large particles on the other hand have broad distribution of discrete charge states. There are several phenomena in dusty plasmas that strongly depend on charge and size distribution. Coagulation and particle transport are strongly influenced by particle size and charge distribution. At this instant, coagulation is important between the large negatively charged particles and the small neutral particles, enhanced by the image potentials in neutrals (24). Similarly, particle transport is primarily by neutral drag, ion drag, electric force and gravity. These forces strongly depend on particle charge and size. Therefore, a distribution in size and charge distribution will also result in a distribution of forces and particles will drift accordingly. It can be observed from figure 3.3 that larger particles are pushed farther towards lower electrode because of neutral drag. Thus, the study of particle size and charge distribution obtained by sectional methods reveals important details of physics of dusty plasmas.

### 3.2.3 Case 3: t = 5 s and t = 6 s

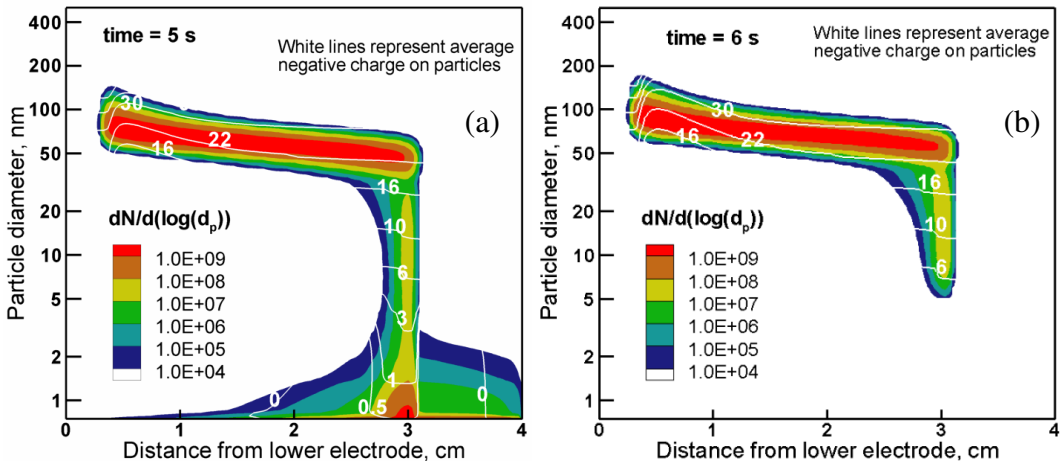


Figure 3.5: Particle size distribution and average charge at (a) t = 5s and (b) t = 6s

Figure 3.5 (a) shows the particle size distribution at 5s and 6s. At 5 s, particle cloud has been pushed towards the lower electrode primarily by neutral drag and gravity and the mean particle diameter at the location of peak concentration (x=0.52 cm) is around 80 nm. Average particle charge for 80 nm particle at this location is -22. Ion drag pushes particles out of the center towards the electrodes causing the large spatial spread of dust particle cloud. At 5 seconds, particle size distribution is still bimodal because of the fresh nucleation near upper electrode. However, as particles grow in size and accumulate more charges, ion drag, which is proportional to charge (depends on size) and $d_p^2$, results in larger spatial spread of dust particle cloud and therefore quenching the nucleation at 6 s (figure 3.5 (b)).

As the nucleation is quenched, neutral and positively charged particles diffuse to walls or coagulate with the large negative particle, leaving only the stably trapped negative particles near upper electrode. Figure 3.6 (a) and (b) shows the neutral, negative and

positive particle profiles at 5 and 6 s. At 5 seconds, positive, neutral and negative particles have significant population. However, at 6 seconds, neutral and positive particles have disappeared from the system and the size distribution is no longer bimodal. Since only negatively charged dust particles are present in the system, there is no coagulation at this time.

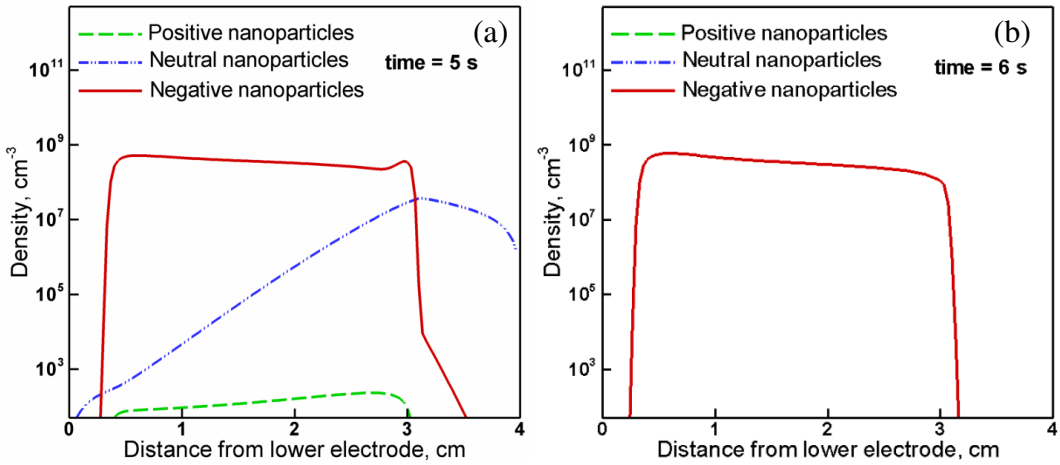


Figure 3.6: Density profiles of positive, neutral and negative nanoparticles at a) 5 s and b) 6 s

Figure 3.7 shows the profile of charge carrier densities at 5 seconds. It is clear from figure 3.7 that dust particles and plasma are very strongly coupled to each other. For example, asymmetry in dust particle distribution, which arises due to size and charge dependent forces, results in asymmetry in electron and ion density profiles. Bigger particles consume more electrons therefore larger concentration of electrons is depleted near lower electrode in comparison to upper electrode where relatively small dust particles are in abundance. In the same manner, ion density follows the dust particle charge density to maintain quasineutrality.

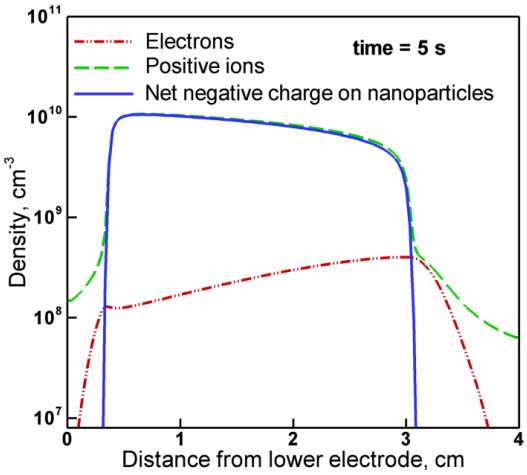


Figure 3.7: Density profiles of electrons, ions and net negative charge carried by nanoparticles

### 3.2.4 Case 4: t = 11 s

Figure 3.8 (a) shows the particle size distribution at t = 11 s. At this instant, high concentrations of particles with diameter 100 to 200 nm with mean diameter of 140 nm is present in the system. It is interesting to note that the white lines showing the contours of average charge on particles have significant curvature in the lower half of reactor and then tend to become horizontal in the upper half of reactor. This implies that for a given particle size, its charge distribution is sensitive to its location except in upper half of reactor.

Particle charge distribution is strongly influenced by the electron and ion density. Figure 3.8 (b) shows the profiles of electron density, ion density and net negative particle charge density at 11.0 s. Electron density near lower electrode is two orders of magnitude lower than the ion density and most of the negative charge is carried by dust particles. This is

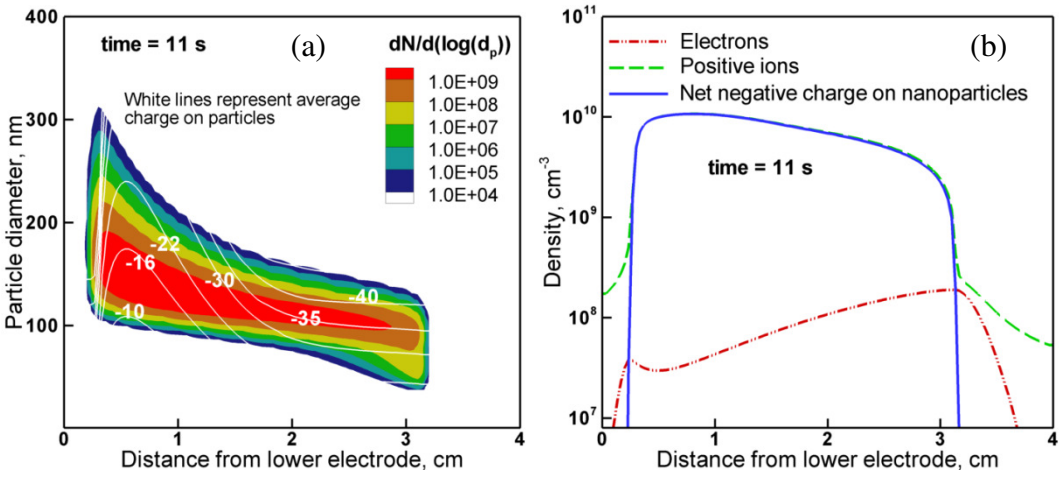


Figure 3.8: a) Particle size distribution and average charge at t = 11 s, b) density profiles of electrons, ions and net negative charge on dust particles

because of the presence of high concentration of large particles near upper electrode. Large particles are pushed towards lower electrode by neutral drag, ion drag and gravity leading to nonuniform distribution of particles over the spatial domain. Since the particles deplete electrons therefore ion to electron ratio varies strongly across the plasma. Dust particles in the lower half of reactor become less negatively charged because of the higher ion to electron ratios in that region in comparison to upper half of the reactor. This leads to strong curvature in the contour lines representing particle charge. It is interesting that although the particles are bigger near lower electrode, they are less negatively charged on average in comparison to smaller particles near upper electrode. For example, particle of diameter 175 nm at location 0.54 cm away from lower electrode carries 16 negative charges whereas particle of diameter 110 nm at midplane carries 35 negative charges.

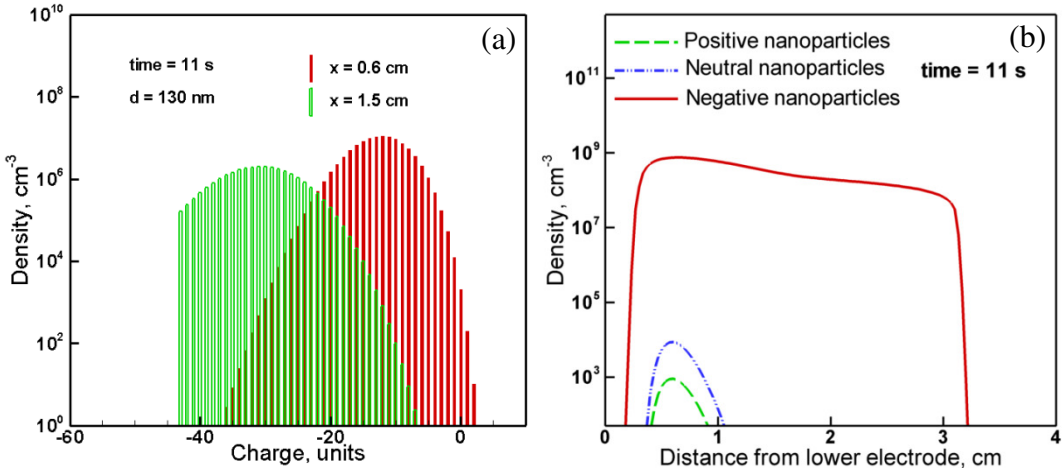


Figure 3.9: a) Charge distributions for 130-nm-diameter particles located either 0.6 or 1.5 cm from lower electrode at t = 11 and b) density profiles of positive, negative and neutral nanoparticles at t = 11 s

Spatially nonuniform electron and ion density profiles result in different charge distribution for a give size of particles at different locations. Figure 3.9 (a) shows the charge distribution of 130 nm particles at x=1.5 cm and x=0.6 cm from lower electrode. At x=1.5 cm, ion to electron density ratio is 124 and the average charge on 130 nm particles is -30.7. However, at x=0.6 cm, ion to electron density ratio is 341 which results in ion attachment being greater than electron attachment and therefore the average charge is -12.0 with small fraction of particles being neutral and even positively charged. Figure 3.9 (b) shows the profiles of positive and neutral particles along with the negatively charged particles in the reactor at 11 s. Although the concentration of neutral and positive particles is orders of magnitude lower than the negative particle concentration, it has important consequences. For example, coagulation at this instant is between the large positively charged or neutral particles and the large negatively charged particles. Similarly, positive particles are accelerated towards the walls and the neutral particles diffuse towards the walls causing a net flux of large particles falling onto the electrodes.

## 3.3 Importance of size and charge distribution on the nature of coagulation

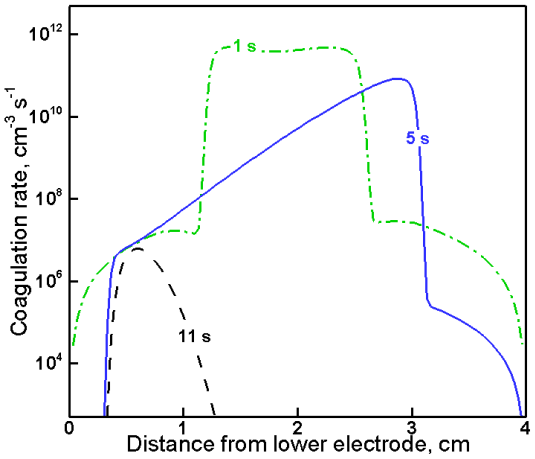


Figure 3.10: Profiles of coagulation rate for various times following onset of nucleation

Coagulation is one of the very important features of dusty plasmas and has been studied in depth (24,46,70). Nature of coagulation is strongly influenced by the size and charge distribution of particles. Figure 3.10 shows the profiles of coagulation rate at different instant at 1s, 5s and 11s. At 1s, coagulation rate is higher in the central part of reactor and reduces near the walls. Figure 3.3 shows the particle size distribution and average charge at 1 s. It is clear from figure 3.3 that the large negatively charged particles are trapped outside the sheaths (x = 1.1 cm to x = 2.6 cm) and the nucleation is also prominent in the same region. Therefore outside the sheath region, coagulation is primarily between small neutral particles and large negatively charged particles enhanced by image potentials in neutrals (24). However within the sheaths, coagulation is primarily between small neutral particles which are not trapped and diffusing towards the electrodes.

At 5 s, coagulation rate peaks at a location 3 cm away from lower electrode (figure 3.10). At 5 s, particles are pushed towards the lower electrode opening the space for nucleation near the upper electrode i.e. around x = 3 cm. At this time because of high particle surface area, nucleation is confined to a small region near x = 3 cm. As seen in figure 3.6 (a), the concentration of neutral particles peaks at 3 cm and then decreases towards both electrodes. Similar to the nature of coagulation at 1s, coagulation at 5 s is prominent outside the sheath region (x = 0.3 cm to x = 3.0 cm) and is mainly between large negatively charged particles and small freshly neutral particles enhanced by the image potentials (24). Slope in the coagulation rate at 5 s in bulk of plasma is related to slope in profile of neutral particles as seen in figure 3.6 (a).

At 11 s, nature of coagulation is quite different than at 1 s and 5 s. At 11 s, fresh nucleation has been quenched by the outward spread of particle cloud. At this time, as seen in figure 3.9 (b), positive and neutral particles are present near lower electrode because of strong electron depletion by attachment to particles as mentioned in section 3.2.4. Therefore coagulation at this instant occurs between large particles and primarily between oppositely charged particles, enhanced by Coulomb attraction.

At 6 s, nucleation has been quenched because of the outward spread of particles and the electron depletion is not yet strong enough to generate positive particles. Therefore, only negatively charged particles are present in the system and there is no coagulation at this instant.

## 3.4 Summary

Self consistent numerical simulations of plasmas in which nanoparticles nucleate and grow were performed for the spatiotemporal behavior of particle size and charge distribution. Snapshots of particle size and charge distribution at several times were presented, together with corresponding plasma properties. Dust particles are strongly coupled to plasma and therefore as particles grow and move in reactor, plasma properties change significantly. The importance of polydispersity in size and charge distribution was discussed and it was found that several phenomena like coagulation and particle transport are strongly influenced by the particle size and charge distribution.

# Chapter 4: Comparison with experiments

In the previous chapters, we discussed the computational model and the results of particle size and charge distribution. This chapter is based on comparing the results of numerical model with the experiments. Numerical model consists of equations describing the physics of specific system. Comparison of numerical model with experiments is important to know the validity of equations in describing the physical behavior of the system. Depending on the results of comparison with experiments, equations can be modified or added to simulate the system more accurately. Once the numerical model results are in good qualitative and quantitative agreement with the experiments, they can be used to understand the fundamental physics as well as design the systems with similar physics for specific application. Therefore, in this chapter, an effort is made to compare the results of model with the experiments.

There has been a significant experimental and numerical research (7,10,23,39,42,47,70) in dusty plasmas but few comparisons of numerical model and experiments exist. Denysenko et al (43) performed measurements of spatial distribution of emitted light, Hα line and electron density in argon-acetylene plasma and compared these measurements to a simplified 1 D numerical model results. Measurements related to plasma emission were performed by spectrograph and for the electron density measurements microwave interferometry was used. Plasma fluid model was used with the assumption of monodisperse particle distribution. Sheath and bulk plasma were modeled separately and the dust particle transport was not taken into account. Numerical model results were in good agreement with the experimental measurements.

Warthesen and Girshick (23) compared the axial profiles of calculated scattered light intensity from their numerical model with the measurements of Rozsa et al (73). The experimental conditions like pressure, voltage and electrode gap were slightly different from the simulation conditions. It was concluded from both the simulation and experimental results that the smaller particles are trapped in center while the larger particles are pushed towards electrode walls by ion drag force, forming a double layer of particles near sheath edge.

Schweigert et al (45) presented the comparisons of numerical model and experiments for argon-acetylene plasma. They used a hybrid fluid-kinetic model to simulate discharge behavior in presence of dust particles. Their model assumed monodisperse particle distribution and accounted for particle transport by ion drag, electric force and diffusion. Their kinetic model accounts for non-Maxwellian electron and ion distribution. They compared their model results of particle density and power with the measured laser light scattering and emission from plasma at different times. Their model results were in good agreement with the experimental results. They also reported that as the dust particles grow in time, discharge behavior changed from capacitive mode to resistive mode. However, their numerical model was not transient and did not account for particle formation, coagulation and surface growth. They assumed that in the experiments, particle distribution is monodisperse and particular time in experiments corresponds to a particular size of particles. Based on this assumption, they changed the particle size in their numerical model and obtained the steady state results.

Among the studies discussed above, the model by Warthesen and Girshick (23) is fully self consistent model and simulates the spatio-temporal evolution of plasmas in which nanoparticle nucleate and grow. However, their model does not account for particle transport by neutral drag and the effect of image potentials in neutral-charged particle coagulation. In this chapter, computational model, as described in chapter 2 with the assumptions given in chapter 3, is used for the comparison with experimental measurements of laser light scattering and emission from plasma. Before presenting the comparison, we give a brief description of three different techniques used in this chapter followed by a detailed description of experimental setup.

## 4.1 Diagnostics for dusty plasmas

In this work, three diagnostic techniques namely laser light scattering, plasma emission measurements and particle collection are used for the diagnostics of dusty plasma. Laser light scattering and plasma emission measurements are *in situ* techniques, however particle collection measurements is an *ex situ* technique. These three techniques have been used differently in different experimental setting. Following is brief description of these techniques in the context of experiments performed in this work:

### 4.1.1 Laser light scattering

Laser light scattering is one of the most widely used methods for particle detection in plasma reactors. A laser beam is directed to the plasma chamber through an optical window. If the particles are present in the system, they interact with the laser beam and scatter the light in different directions. Intensity of scattered light is a function of particle

size distribution and the angle between scattered and incident beam. A detector is placed in front of a window to detect the scattered light. The angle between scattered and incident beam depends on the geometry of system and availability of windows. Detector is generally a charge-coupled device (CCD) camera which can be automated to take snapshots of scattering signal at certain time intervals. This enables one to record the temporal behavior of laser light scattering.

Wavelength of laser beam is an important parameter. Shorter wavelengths correspond to higher energy laser beams like x-rays. If the laser beam wavelength is short or in other words it has high energy, interaction of laser beam with plasma and dust particles may lead to significant change in the properties of plasma and dust particles. If the laser has longer wavelength or in other words low energy, it might not detect particles of small size. Therefore, there is always a compromise in selecting the laser wavelength such that the interaction of laser with dust plasma should not affect its properties and at the same time it should be able to detect particles of reasonably small size. For example, laser beam of wavelength 405 nm is less energetic to change the properties of plasma and at the same time detect particles of size greater than 20 nm.

Scattered light can be predicted theoretically if the particle size distribution function is given. Mie solutions to Maxwell's equations describe the scattering of electromagnetic radiation by a spherical particle. According to Mie scattering theory, scattered light is a complex function of scattering direction, particle size, refractive index and polarization of incident laser beam. A simplified Rayleigh approximation describes scattering of light by

spherical particles which have diameter much smaller than the wavelength. According to this approximation the expression for scattered light intensity $I$ can be given as:

$$I = I_0 \left(\frac{1 + cos^2\theta}{2R^2}\right)\left(\frac{2\pi}{\lambda}\right)^4 \left(\frac{m^2 - 1}{m^2 + 2}\right)\left(\frac{d_p}{2}\right)^6 \qquad (4.1)$$

Where $I_0$ is the light intensity of the incident beam, $R$ is the distance between the detector and particle, $\theta$ is the scattering angle between the incident laser beam and scattered beam, $m$ is the particle refractive index and $d_p$ is the diameter of particle.

### 4.1.2 Particle collection measurements

Particle collection measurement is an ex situ technique for characterizing the properties of dust particle. Properties like size, refractive index, chemical composition, morphology are very important and facilities like electron microscopy, X-ray diffraction and Raman spectroscopy can be used to characterize the particle properties.

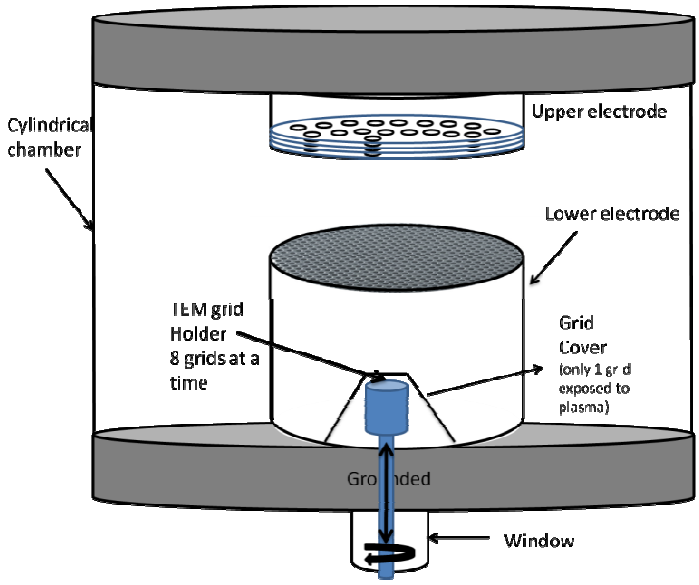


Figure 4.1: TEM grid holder for particle collection measurements

Electron microscopy techniques are used to obtain information on particle size and morphology. Particles can be collected on electron microscope grids. In the experiments performed in this work, electron microscope grids are placed on a rotating multigrid holder (figure 4.1) as described by Boufendi et al (7). Grid holder is covered by an aluminum tube with a hole such that only one grid is exposed for the particle collection. Particles are swept by the gas flow and gravity once the discharge is turned off and some of the particles are collected over the electron microscopy grid.

To study the kinetics of particle size distribution, Bouchoule and Boufendi (70) performed particle collection measurements for various plasma durations for the same plasma conditions. They analyzed the particles collected over electron microscope grids and calculated the mean size and standard deviation for the particle size distribution.

### 4.1.3 Plasma emission measurements

Optical emission spectroscopy is one of simplest and useful technique to study the changes in plasma with the formation and growth of the dust particles. It has been reported by Bouchoule and Boufendi (70) that the plasma becomes brighter in the presence of dust particles. Dust particles consume electrons so the electron density goes down. However, electron temperature increases to compensate for the depletion of electrons. Consequently, excitation rate of argon is increased resulting in the brighter plasma. Therefore, optical emission spectroscopy provides useful information related to changes in plasma with the evolution of dust particles.

Bouchoule and Boufendi (70) have used this technique in argon-silane plasmas to analyze the plasma properties. They used a microscope lens in front of the optical window to focus the light coming from plasma on the optical fiber of a spectrometer. Optical fiber can be a single optical fiber giving the details of specific location in the plasma reactor or one can use an array of optical fibers to get the spatial profile of emission intensity. Spectrometers are also capable of recording temporal evolution of emission intensity.

To study the specific excitation process, one can select the wavelength corresponding to that particular process and filter other wavelengths. This allows one to study the important excitation processes in plasma in presence of dust particles. Bouchoule and Boufendi (70) used optical emission measurement with electron density measurements using microwave cavity technique to study the electron temperature during the evolution of dust particles.

## 4.2 Experimental setup

The experimental setup is shown in figure 4.2. The experimental setup consisted of an rf-capacitive discharge with a powered upper showerhead electrode and grounded bottom electrode with 1-mm diameter holes and 20% transparency. The setup consisted of a large cylindrical chamber with electrodes located within that chamber. The discharge was not contained around the periphery of the two circular electrodes, representing an open configuration. The pump port was located perpendicular to the axis of cylinder as shown in figure 4.2. This introduces large radial component in the experimental flow profile making the flow profile 3D as shown in figure 4.3. It is difficult to numerically model such type of flow profile in 1D, therefore stagnation flow profile is assumed in the

numerical model. The setup has been described in detail in (74). The operating conditions for experiment as well as model consist of a pressure of 17 Pa (127.5 mTorr), gas temperature 300 K, RF voltage amplitude 55 V with a DC self bias at the powered electrode of -20 V, 13.56 MHz frequency and gas flow rates of 30 sccm argon and 1 sccm silane.

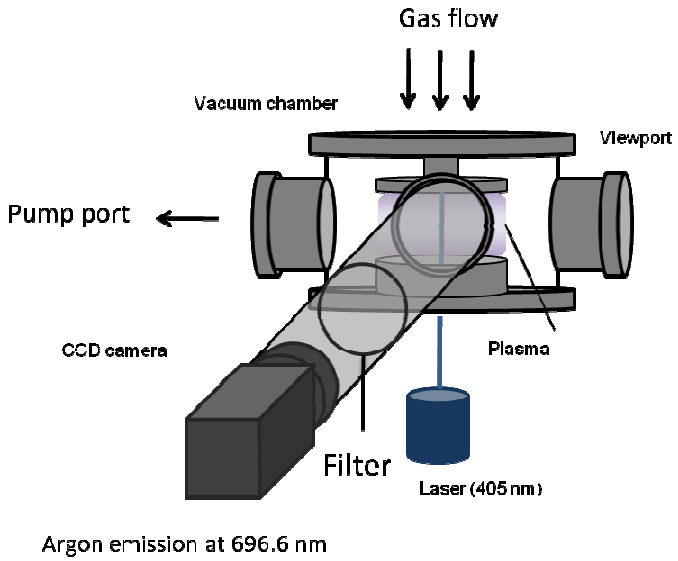


Figure 4.2: Experimental set up

For laser light scattering measurements, laser of wavelength 405 nm was sent from the window located at the bottom of cylindrical chamber. By sending laser in the above mentioned way, the whole spatial domain along the axis of cylinder can be captured in one shot. However, laser sent from the bottom window results in strong reflection from top metal electrode as shown in figure 4.4 (a) and (b). Figure 4.4 (a) shows a schematic of laser sent from lower electrode and figure 4.4 (b) shows a snapshot of plasma reactor and the reflection from top electrode. Reflected light from top electrode might cause scattering from particles and therefore result in erroneous result. Scattered light was

captured using from the window perpendicular to the axis of cylinder using a CCD camera. CCD camera was also used to measure the plasma optical emission. CCD camera can be set to automatically take snapshots at certain time intervals. Using this experimental setup, spatially and temporally resolved measurements of laser light scattering and plasma optical emission were obtained and compared with the same calculated using numerical model.

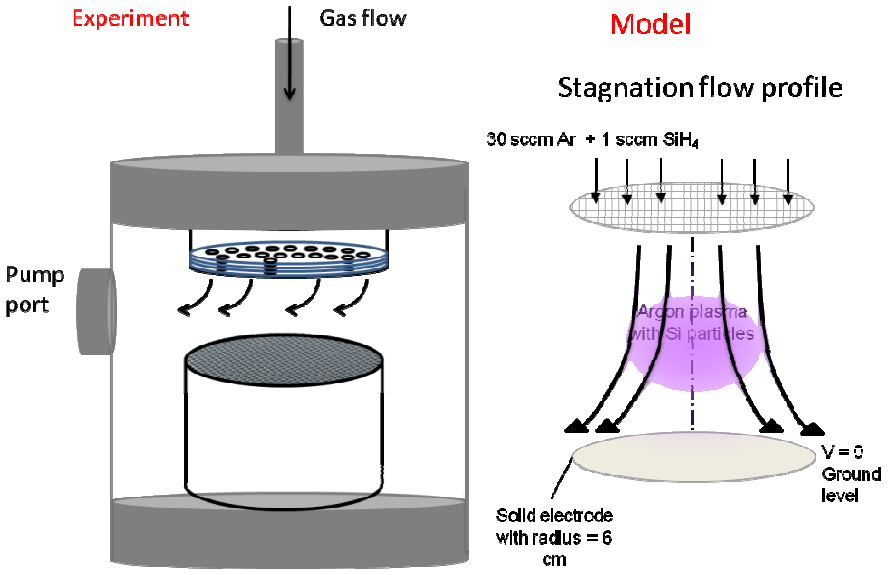


Figure 4.3: Experimental flow profiles and the stagnation flow profile

Mie scattering theory was used to calculate spatial profiles of laser light scattering from numerical model. According to Mie theory, scattered light is a function of particle size distribution, refractive index, angle between incident and scattered light. To calculate the scattered light, particle size distribution was obtained from numerical model, refractive index was assumed to be that of pure crystalline silicon particles at 405 nm

(5.4+0.24*i*,(75)) and the scattered light was perpendicular to the incident laser beam.

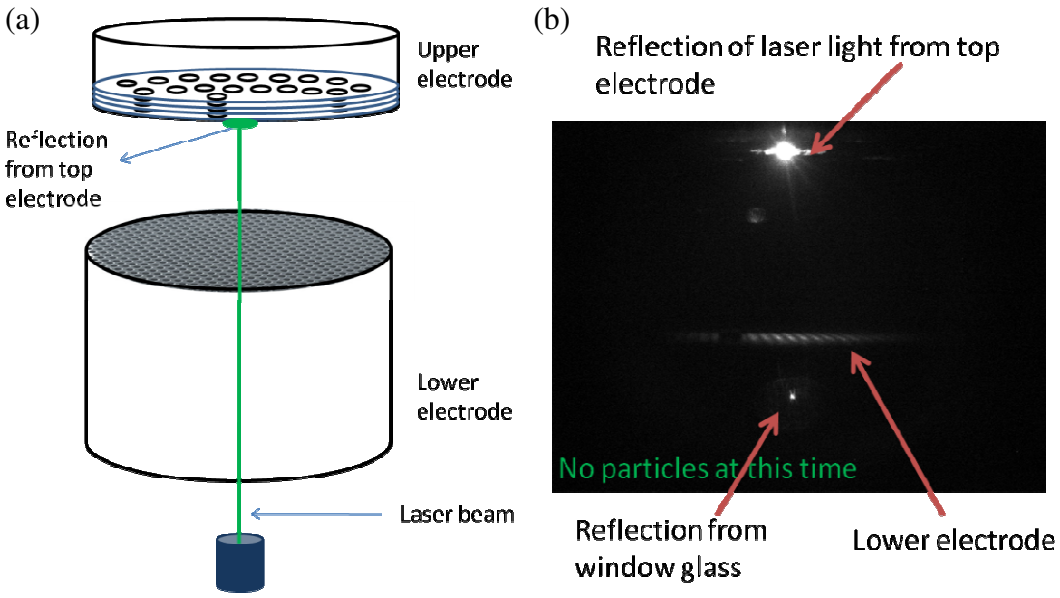


Figure 4.4: Reflection of laser from top electrode shown in a) schematic and b) in the snapshot

Fortran code given in Bohren and Huffman (76) was used for calculating the ratio of scattered light intensity and incident laser light intensity ($Q_{ext}(\pi d_P/\lambda,m)$ where $d_P$ is particle diameter and $\lambda$ is laser wavelength, m is particle refractive index) from single particle. This ratio is called Mie scattering coefficient. Mie scattering coefficient was integrated over the particle size distribution obtained from numerical model in the following way:

$$\left(\frac{I}{I_0}\right)_{Total} = L\left[\int_0^{\infty} \frac{\pi d_P^2}{4} Q_{ext}\left(\frac{\pi d_P}{\lambda}, m\right) n_d(d_P) d(d_P)\right] \qquad (4.2)$$

where $n_d$ is the dust particle density and $L$ is the light path length from particle to detector.

Plasma emission depends on electron density and electron temperature. Numerical model provides spatial profiles of electron density and electron temperature at different times. Spatial profiles of plasma emissions are calculated based on the collisional radiative model developed by Vlcek (77). Wavelength for the emission was taken to be 696.5 nm, which corresponds to 4p (13.328 eV) to 4s (11.548 eV) transition of argon excited atoms.

## 4.3 Comparisons of model and experimental results

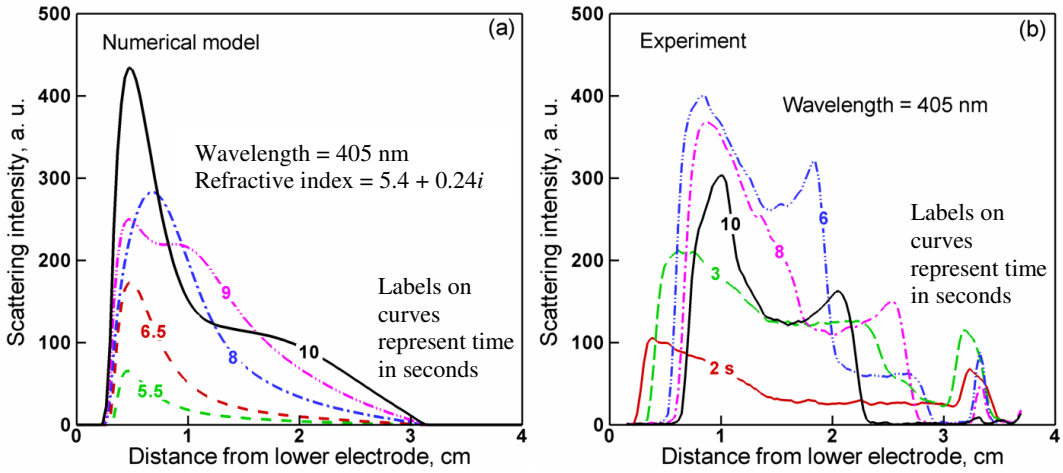


Figure 4.5 (a) Numerical model and (b) Experimental scattering intensity results at different times. Labels on the curves represent time after the plasma was switched on.

### 4.3.1 Laser light scattering comparisons

Figure 4.5 (a) shows simulation results for predicted spatial profiles of laser light scattering intensity at various times, and Figure 4.5 (b) shows the corresponding experimental measurements. In experiments, time zero corresponds to the time when the plasma was switched on. There is always a time lag between switching on the plasma and the onset of nucleation and this time lag depends on plasma conditions like temperature (78). In the numerical model, time zero corresponds to the time when plasma is ON and

particle formation has started. Time lag in onset of nucleation and surface growth rate could be two important factors in the time discrepancy between numerical model and experiments.

Comparing these results, there are two main areas of qualitative agreement, and some discrepancies. The simulations and the experimental results both indicate that light scattering is concentrated in the lower half of the electrode gap. This is expected because large particles are pushed towards lower electrode by the neutral gas drag and gravity. Neutral drag is proportional to the square of diameter and the force of gravity is proportional to the cube of diameter. Scattering is more pronounced in the lower half of the reactor because scattered light is proportional to $6^{th}$ or $3^{rd}$ power of diameter depending on Rayleigh ($\pi d_P/\lambda << 1$) or Mie regime ($\pi d_P/\lambda \sim 1$). In dusty plasmas, sheath structure depends not only on plasma conditions but also on particle transport. Particle are negatively charged and trapped by electric force. If the particles are pushed towards the wall by a drag force, sheath width reduces and electric field increases such that forces on particles are balanced. Therefore, sheath structure being similar in experiments and modeling justifies the use of stagnation flow profile to compensate the large radial component in experiment due to the location of pump port. One of the discrepancies is that the experiments show a small scattering peak near the upper electrode, not predicted by the model. The cause of this discrepancy is presently not understood. It might be due to complex flow profile in experiments or due to the reflection of laser from upper electrode.

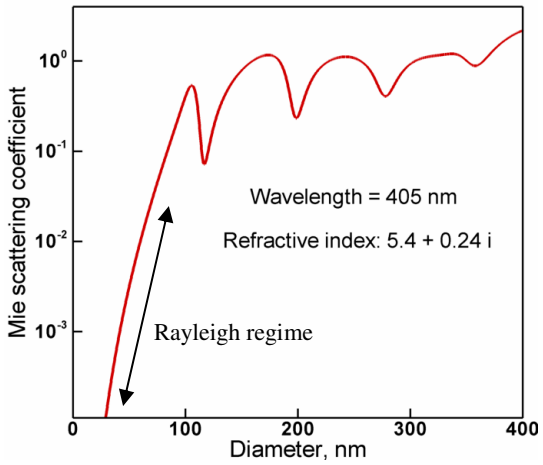


Figure 4.6: Mie scattering coefficient vs. diameter for refractive index 5.4 + 0.24 i (c- Si) at wavelength of 405 nm

As seen in Figure 4.5 (a) and (b), both experimental results and simulations indicate that after several seconds the scattered intensity profile develops a double-peaked structure (not counting the small peak near the upper electrodes in the experiments), with a minimum in between. Superficially this seems to suggest the existence of a double layer of particles, one layer near the lower electrode, the other closer to the center of the plasma. However, the simulation results indicate that this is not the case. Instead, the simulation indicates that this behavior is caused by a resonance in Mie scattering as particles grow out of the Rayleigh scattering regime and beyond about 100 nm in diameter.

This point is demonstrated by Figures 4.6 and 4.7 ((a), (b) and (c)). Laser light scattering depends on particle density and Mie scattering coefficient (equation 4.2). Mie scattering coefficient is a non linear function of particle size. Figure 4.6 shows the predicted single-

particle scattering intensity vs. particle diameter from Mie theory. For the assumed refractive index, a first strong resonance peak (minimum in scattering) occurs at 114 nm.

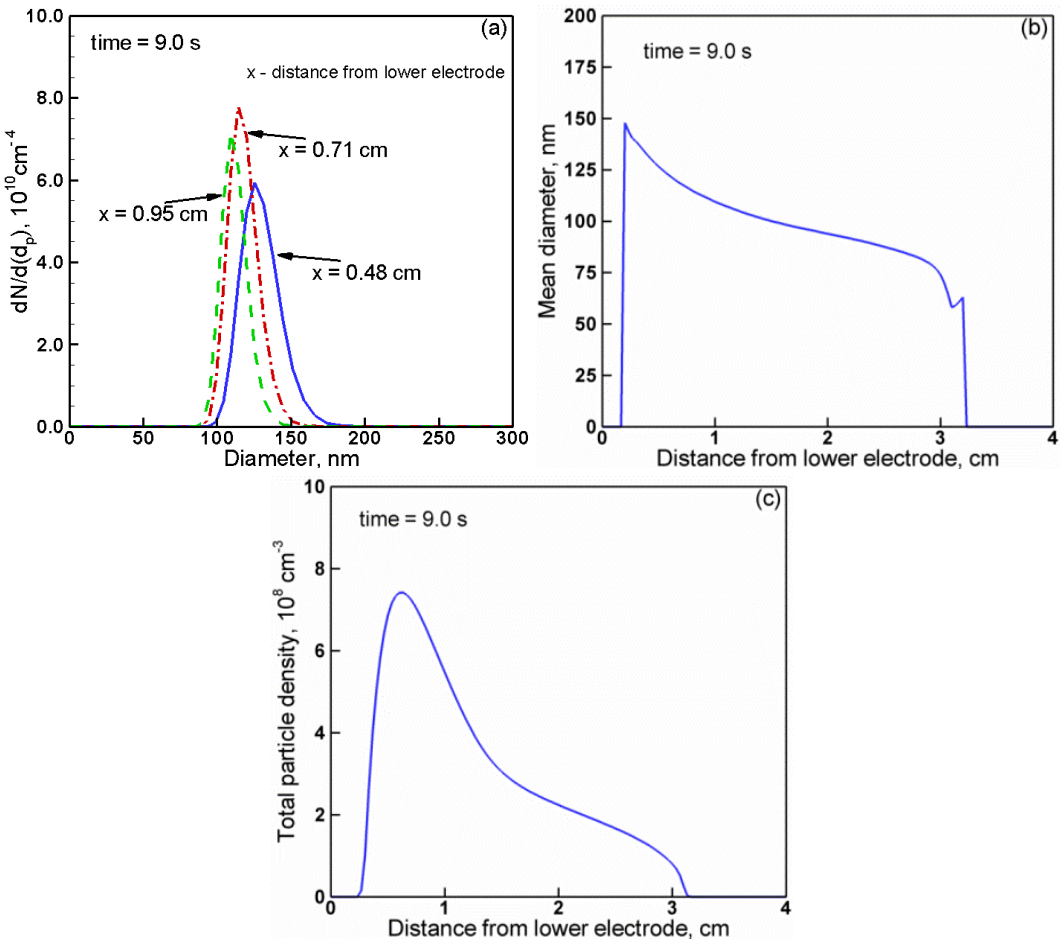


Figure 4.7: (a) Particle size distribution at three spatial locations corresponding to two minima and maxima of model scattering profile at 9s (b) Particle mean diameter at 9 s (c) Particle density profile at 9 s

Figure 4.7 (a) shows the particle size distributions at three locations, corresponding to the two maxima (x = 0.48 cm and x = 0.95 cm) and the minimum (x = 0.71 cm) in the scattering intensity profile in the simulation at t = 9 s (seen in Figure 4.5 (a)). Modal diameters at three locations x= 0.95 cm, x = 0.71 cm and x = 0.48 cm are 110 nm, 114 nm and 125 nm respectively. Figure 4.7 (b) shows that the average particle size increases

as distance from the lower electrode decreases. This is caused by a combination of ion drag, neutral drag and gravity. Figure 4.7 (c) shows the particle density profile at 9 s. At x = 0.71 cm, particle density is higher than the same at x = 0.48 cm and x = 0.95 cm. Particle density and particle diameter both are higher at x = 0.71 cm in comparison to x = 0.95 cm, but, as seen in figure 4.5 (a), scattering intensity is slightly lower at x = 0.71 cm than at x = 0.95 cm. This is because the modal diameter at x = 0.71 cm lies right on top of the Mie resonance (minimum in scattering) at 114 nm. Although, the particle density is lower at x = 0.48 cm in comparison to both x = 0.71 cm and x = 0.95 cm, scattering intensity is higher because of higher Mie scattering coefficient in comparison to x = 0.71 cm and x = 0.95 cm.

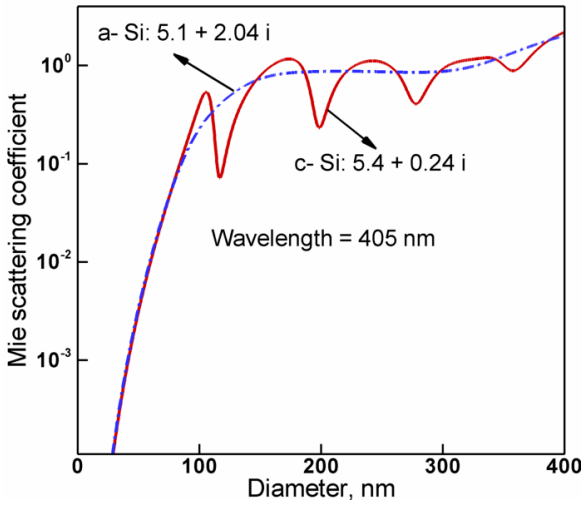


Figure 4.8: Mie scattering coefficient for amorphous (a- Si) and crystalline silicon (c- Si), complex numbers are the refractive indices for a-Si and c-Si

It is important to note that Mie scattering strongly depends on the refractive index of particles. Figure 4.8 shows the Mie scattering vs. diameter for two refractive indices corresponding to crystalline (5.4+0.24*i* ) and amorphous (5.1 + 2.04*i*) silicon. Figure 4.8

shows that the scattered light is strong function of refractive index and Mie resonances do not occur in case of amorphous silicon. In the numerical model, particle refractive index represents crystalline particle. It is clear from Figure 4.8 that selecting amorphous silicon particle refractive index will not result in the double peak structure. Therefore, from the analysis of numerical model results, it cannot be concluded that the double peak structure in experiments is due to Mie scattering. One of the possibilities for double peak structure in experiments is related to complex 3D gas flow profile. At this stage, it is difficult to know the reason for double peak structure in experiments and it is subjected to further research. However, if it is true that the double peak structure is due to resonances in Mie scattering, then the scattering measurement can be used to know the particle size in the system given the optical properties of the particles.

Optical properties of dust particles in argon-silane plasma have not been very well explored. It has been reported in couple of papers dating back to mid 90's (79,80) that the dust particle refractive index in argon-silane plasma is close to amorphous silicon. However, recently it was reported that particle refractive index strongly depends on hydrogen content of dust particle and plasma conditions which vary depending on particle size and location in reactor (81,82). For example, high hydrogen content, particle heating and plasma operation at high powers lead to crystalline particle. Further research is required to explore the optical properties and morphology of particles formed in argon silane plasmas.

### 4.3.2 Emission intensity comparisons

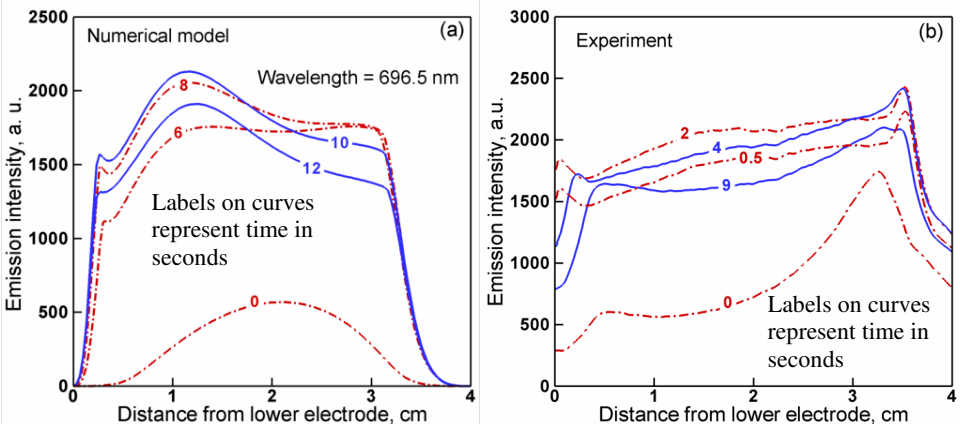


Figure 4.9 (a) Numerical model and (b) Experiment emission intensity results at different times. Labels on the curve represent time after the plasma was switched on

Figure 4.9 shows the spatial profiles of emission intensity at 696 nm predicted by the numerical simulations and measured in the experiment at different times. Again, time zero in experiments corresponds to the time when the plasma was switched on. At this time the plasma is pristine plasma and it takes some time before the particle formation starts. In the numerical simulations, there is no chemistry therefore parameterized nucleation and surface growth rates were assumed and at time zero particle formation and growth has just started. Still, the emission profile at time zero in numerical model corresponds to pristine plasma. Process of nucleation and surface growth affects the time scales of dusty plasma. One should be careful in comparing the time scales of model and experiment.

It can be seen from figure 4.9 (a) and 4.9 (b) that there are both similarities and discrepancies between the model predictions and the experiments. Emission at time 0 seconds, when the plasma is pristine, is considerably different in model and experiment

(figure 4.9 (a) and 4.9(b)). This difference is due to stochastic heating near the sheath region in experiments. Numerical model in this work accounts only for ohmic heating and not the stochastic heating. Such difference caused by stochastic heating has been previously reported by Nitschke and Graves (83) by comparison of Particle in cell (PIC) simulation and classical fluid model of capacitively coupled pristine plasma. Paticle in cell model included stochastic heating whereas classical fluid model did not. Nitschke and Graves (83) report that the difference in heating near the sheath regions is prominent at lower pressures and the reason for this difference is that the classical models do not account for stochastic heating at sheath boundaries. However, it has been reported in several modeling and experimental studies related to dusty plasmas (42,43,45,71) that the presence of dust particles makes the plasma much more resistive in comparison to pristine plasma. Therefore, it is fine to compare classical numerical model without stochastic heating and experiment for plasma with dust particles.

Both in experimental measurements and numerical model results, emission intensity is relatively low in the region where particle light scattering is strongest, and peaks near the upper electrode, where light scattering is relatively weak. Comparing figures 4.5 (a) and 4.9 (a) of numerical model, scattering intensity at 10 s peaks at 0.48 cm from lower electrode whereas emission intensity at 10 s peaks at 1.14 cm from lower electrode and is quite low at 0.48 cm. For the experiments, scattering intensity peaks at 1 cm from lower electrode at 10 s where as emission intensity at 9 s is lowest at 1 cm from lower electrode. This behavior is explained by the fact that plasma emission depends on the local electron density, and particles deplete electrons by electron attachment. This is

illustrated in Figure 4.10 (a), which shows simulation results of electron density profile at different times. To some extent, the emission intensity profiles in Figure 4.9 (a) follow the electron density profile.

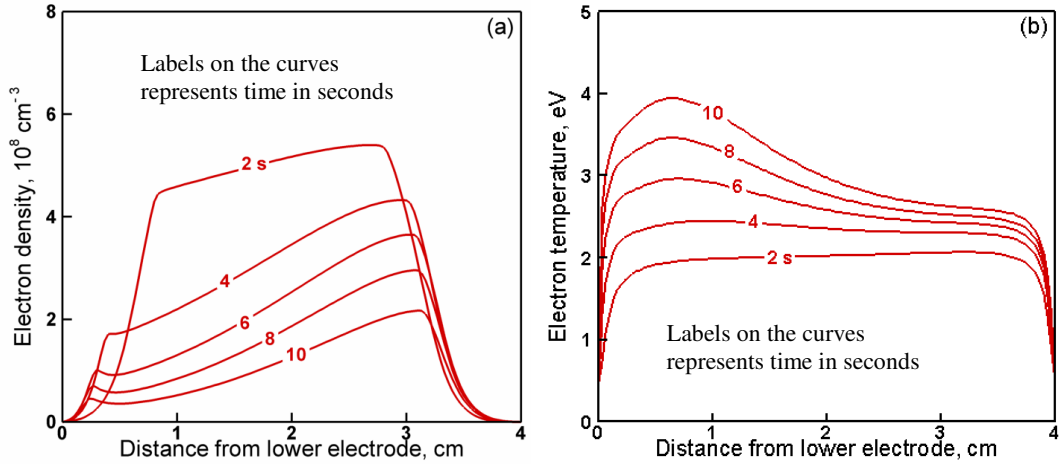


Figure 4.10: (a) Electron density profile and (b) Electron temperature profile at different times. Labels on curves represent time after the plasma was switched on.

However the emission profile does not completely follow the electron density profile, because emission is affected not only by electron density but also by electron temperature. Figure 4.10 (b) shows the simulation results of electron temperature profile at different times. Electron temperature increases as particles grow. This fact also explains the interesting observation that both the experiment and simulation indicate that emission intensity at first increases with time, but then begins to decrease.

For given RF voltage, as electron density decreases (figure 4.10 (a)) due to attachment to particles, electron temperature increases (figure 4.10 (b)) in order to create more electrons and ions to maintain quasineutrality. It can be seen from figure 4.10 (b) that the electron temperature near lower electrode increases from 1.8 eV at time zero to 4.0 eV at 10 s. At

earlier times up to 8 seconds, increase in electron temperature dominates over decrease in electron density and this causes emission intensity to increase, despite the drop in electron density. However, at later times, when particles have grown up to 100 nm around 8 seconds, electron depletion becomes very strong and depletion in electron density dominates over increase in electron temperature which causes plasma emission to decrease.

It is also interesting to note that the peak near lower electrode appears at earlier times and diminishes at later times both in model and experiment (figure 4.9 (a) and (b)). In the profiles of emission intensity from numerical model (figure 4.9 (a)), development of the peak near lower electrode can be seen at 6, 8 and 10 s. The peak diminishes at 12s. In the measured profiles of emission intensity development of the peak can be seen at 0.5, 2 and 4 s. The peak completely diminishes at 9 seconds. This peak is related to similar peak in electron density profiles at 4s – 10s (figure 4.10 (a)). This peak appears because of the ionization at the sheath edge and as the electron temperature increases with time, peak becomes stronger. However, as the particles grow bigger, they, being pushed towards lower electrode by neutral drag force, consume the electrons and therefore the peak near lower electrode diminishes.

### 4.3.3 Particle deposition at electrodes

In order to experimentally investigate the size of particles that reach the electrodes, particles were collected on TEM grids placed on the upper and the lower electrodes. The experiment was conducted with similar conditions as discussed above with the power at 25W, the pressure at 16.6 Pa, and an argon and silane flow rate of 30sccm and 1sccm,

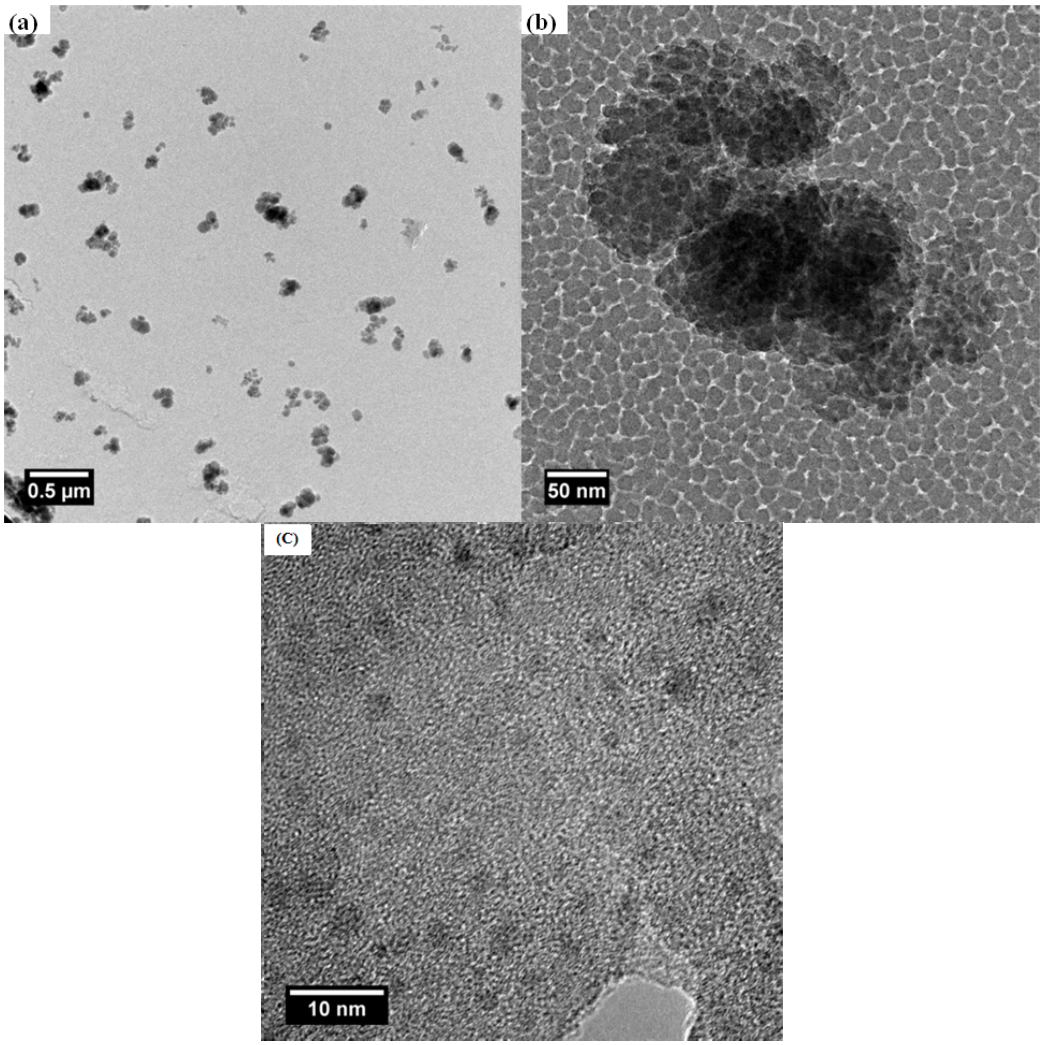


Figure 4.11: TEM images of particle collected at lower (A and B) and upper (C) electrodes

respectively. In order to collect a sufficient number of particles for microscopy, particles were collected over a series runs where the plasma was initiated and left on for 10s then off for 50s which was repeated for a total of ten runs. Particles were being collected over the grids during both on and off phase of plasma. As shown in figure 4.11, the particles that arrived at the lower electrode, figure 4.11 (a) and 4.11 (b), were much larger than the particles that arrived at the upper electrode, figure 4.11 (c).

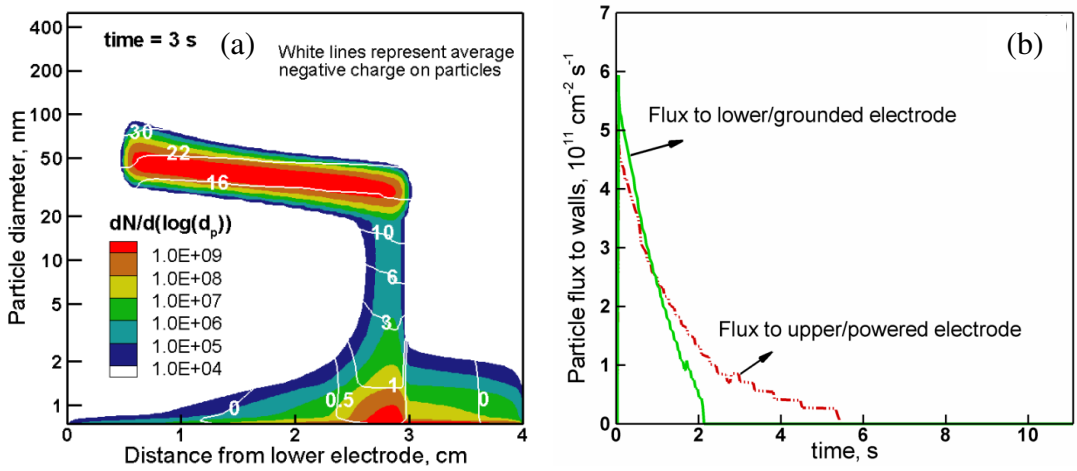


Figure 4.12 a) Particle size distribution and average charge at 3 s and b) nanoparticle flux to walls

Figure 4.12 (a) shows a snapshot of particle size distribution and average charge calculated from numerical model at 3.0 s. Figure 4.12 (b) shows the calculated flux of particles to both electrodes while the plasma is on. As the particle cloud is pushed towards lower electrode by neutral drag and gravity, fresh particle formation is shifted towards upper electrode in the particle free region. This results in a greater flux of small particles by diffusion to upper electrode in comparison to lower electrode. This is counterintuitive because gas drag and gravity try to push particles towards lower electrode. Since the freshly nucleated particles are small, diffusion is much stronger than the gas drag and gravity. Freshly nucleated particles diffusing towards lower electrode are lesser because during the course of their path to lower electrode, they may get charged and therefore trapped in the bulk region of plasma.

In the particle collection measurements presented in this work, particles were found both on lower and upper electrode (figure 4.11). However, these particles were deposited over the electrodes during both on and off phase of plasma. Therefore at this stage of

experimental research, nothing definite can be said about the flux of particles to the electrodes during the on phase of discharge in the experiments and it is subjected to future research.

## 4.4 Summary

Numerical simulations were performed for the spatiotemporal behavior of plasma-aerosol coupled system. Results of numerical model were compared to experimental measurements of spatially and temporally resolved plasma emission and laser light scattering. Experiments and simulations are in reasonable qualitative agreement on several major features of the evolution of scattering and emission profiles. Some discrepancies are likely caused by the fact that the model is 1D, whereas the experimental flow profile is 3D, with the gas flow affected by the presence of an exhaust port perpendicular to the axis of cylinder. Particle collection measurements followed by TEM analysis present interesting results. However, further experimental research is required to support the model prediction of phenomena that there is significant deposition of small size (around 2 nm) particles on upper electrode during the on phase of discharge in spite of gas flow being in opposite direction.

# Chapter 5: Study of dusty plasma afterglow

Plasma afterglow occurs when the discharge is in a decaying state: external electromagnetic fields which maintain the discharge are absent. In pulsed discharges, externally applied electromagnetic fields are present during part of the cycle and turned off for the rest of the cycle. The pulsing and afterglow phases of plasma have been extensively researched (84-87). In the semiconductor manufacturing industry, pulsed plasmas have been successfully used to control electron and ion energy (88-92).

Dusty plasma afterglows are important because they occur in several industrial, as well as laboratory, situations. For example, the deposition of nanoparticles over a substrate when power is turned off may have important implications for particle contamination during semiconductor processing, as well as for deliberate collection of nanoparticles for applications. Afterglows are an intrinsic aspect of plasma pulsing, which is of increasing interest for controlling plasma and nanoparticle properties.

Although the field of dusty plasma has received significant amount of attention from researchers, very few studies have investigated the decay of a dusty plasma discharge (93-98) . Ivlev et al (93) conducted the first experiment on decharging of complex plasmas in microgravity conditions, and developed a theoretical model to predict the residual charge on dust particles. They performed experiments in PKE-Nefedov experimental setup (99) and injected 5.8μm particles in the discharge. They observed that the particles retain around half of its original charge after the plasma is switched off. They also developed a theoretical model based on the time scale of charging and

diffusion. They assumed ambipolar diffusion until the plasma density falls off 3 orders of magnitude from its initial value.

Couedel et al (96) developed a numerical model to study the influence of the ambipolar-to-free diffusion transition on dust particle charge in a dusty plasma afterglow. Their numerical model was based on the time scales of different processes and was not self-consistent. Important physical processes such as space charge electric field and drift diffusion were not modeled. Results were compared with experiments. They observed that the character of ambipolar-to-free diffusion transition strongly influences the charge distribution—the faster the transition occurs, the smaller the mean dust particle charge and positive particles can be observed in charge distribution tail.

Denysenko et al (98) developed a self consistent global model for the afterglow of pure argon discharge and argon discharge with dust particles. Their model considered monodisperse particle distribution. Particle charge was calculated by a charge balance equation. Their model did not account for particle transport and coagulation in afterglow. Particle transport and coagulation can be very important in dusty plasma afterglow and may change the way particles interact with other chemical species, such as argon metastables. They explained the role of argon metastables in pure argon afterglow and in afterglow with dust particles. Based on the comparison of experimental and numerical results, they concluded that metastable-metastable pooling ($Ar^* + Ar^* \rightarrow Ar^+ + e + Ar^0$) is the most important processes for electron generation in the argon/dusty plasma afterglow. Their numerical model results were not in good agreement with the experimental results for the afterglow of argon with dust particles. They mention that the

difference is due to their assumption of a Maxwellian electron energy distribution in the afterglow.

In addition to afterglows, pulsed dusty plasmas have been investigated. Berndt et al (100) conducted experiments of pulsed argon-acetylene discharges. They found that pulse frequency has significant influence on dust formation. According to their results, if frequency is higher than a critical frequency, particle formation is observed; otherwise, particle formation is not observed. They explained their results based on a simple model which calculates the density of those negative ions which are responsible for particle formation.

In another study by Berndt et al (101), they measured electron density in pulsed complex plasma by microwave interferometry. They found that electron density shows anomalous behavior: when power is switched off electron density starts to increase. They propose that there may be some mechanism which causes dust particles to release electrons in the afterglow phase.

Schweigert et al (97) developed a self-consistent hybrid fluid and particle-in-cell Monte Carlo model to study the anomalous behavior reported by Berndt et al (101). In their model, they assume that the charge of particles in afterglow can be calculated by equating electron/ion flux with dust particle flux. They also assume a monodisperse distribution of dust. They claim to account for dust particle transport, though no mention of its effect seems to be made in their calculations. Coagulation was not taken into account in their simulations. They found that electron density in afterglow increases mainly due to

electrons released from the dust surface. They also found that metastable-metastable ionization is also important in the increase of electron density in afterglow.

Besides the aforementioned studies, pulsed dusty plasmas have also been used to produce size-controlled nanoparticles. Kim et al (102) used inductively-coupled pulsed plasmas to produce size-controlled silicon nanoparticles. They reported the size of nanoparticles can be controlled by adjusting the plasma particular times. They also reported that particle growth occurs mainly because of surface growth.

This discussion shows that pulsed dusty plasmas and dusty plasma afterglow are interesting regmies which should be explored in detail. This chapter examines a self-consistent model for dusty plasma afterglow and pulsed dusty plasma which we have developed. The model self-consistently calculates the space charge electric field, particle transport, coagulation, transition from ambipolar to free diffusion, and particle charging in the afterglow environment. The afterglow model does not currently include silane and argon metastable chemistry. However, the model described in this chapter presents a framework for self-consistent afterglow and pulsed dusty plasmas which needs to be improved by adding silane and argon metastable chemistry.

## 5.1 Numerical model and assumptions

To simulate the dynamics of afterglow, we used the computational model described in Chapter 2 with a different time slicing scheme. In a dusty plasma afterglow, the presence of charged species requires the Poisson's equation to be solved despite the absence of an external field. Population balance equations are solved for all species; the details of these

equations are given in Section 2.2. Electron temperature is calculated using the electron energy density equation and assuming a Maxwellian electron energy distribution. In a dusty plasma afterglow, the actual electron energy distribution may be far from Maxwellian, in which case it should be solved kinetically. However, kinetic schemes for electron energy distribution are complex and computationally expensive. For dust particle dynamics, the aerosol general dynamics equation is solved using the sectional method (Section 2.2). This equation has terms for charge-dependent coagulation, particle charging, nucleation, and surface growth. Details of these terms are given in Section 2.2. Orbital motion limited (OML) theory is assumed for particle charging in afterglow. This is a reasonable assumption at low pressures, because the particles' mean free path is much larger than the Debye length. However, as the electrons and ions diffuse to the walls in dusty plasma afterglow, the Debye length is on the order of reactor dimension, so OML theory may not be a good assumption. Again, in such a situation, the kinetic model for particle charging is a better approach. For nucleation and surface growth, it is assumed that as power is switched off, nucleation ends, and the rate of nucleation and surface growth are set to be zero. Once the power is switched off, electrons lose their energy within few microseconds and quench electron impact reactions, which are important for nucleation and surface growth. During the power on part of the cycle, the nucleation rate is assumed to be $10^{12}$ $cm^{-3}s^{-1}$, and surface growth rate is assumed to be 12 nm/s. These values are based on the detailed chemistry model developed by Bhandarkar et al (21). Nucleation is quenched where particle surface area is greater than $1.8x10^{9}$

$nm^2cm^{-3}$. Surface growth is present where nucleation is quenched, as mentioned in Section 3.1.

## 5.2 Time slicing and management of time steps

The time slicing scheme used in the afterglow case differs from that of Chapter 2. During the power-on phase, the plasma and aerosol modules are evaluated at different time steps, as discussed in Chapter 2. However, during the off phase or afterglow phase, both modules are evaluated at the plasma time step ($10^{-10}$ s) until the electrons are relaxed i.e. they lose their energy and lost to the walls. A short time step for both aerosol and plasma is optimal because of the transient nature of plasma afterglow. In an afterglow, or in decaying plasma, electrons and ions are lost by attaching to particles or diffusing to the walls. Therefore, the time slicing technique of Section 2.3, which evaluated the plasma and aerosol modules at different time steps (assuming the aerosol responds to averaged plasma quantities) cannot be used. The global time scale in such a transient system as an afterglow must be the smallest time scale of any event which occurs. Electron diffusion and charging time scales are on the order of $10^{-7}$ to $10^{-6}$ s, so a time step of $10^{-10}$ s is used when electrons are present. When electrons are no longer present, the smallest time scale is that of the ions: $10^{-5}$ s for diffusion and $10^{-6}$ s for charging. Thus, the time step is increased at this point from $10^{-10}$ s to $10^{-8}$ s. Similarly, once the ions are lost from the system, the smallest time scale belongs to dust particles. Depending on the dust particles' size, either diffusion or viscous flow time scales might be important, allowing the time step to be increased accordingly. For example, if particles 2 nm diameter are present in the system, their diffusion time scale is on the order of $10^{-4}$ s, while time scales for

viscous flow are on the order of $10^{-3}$ s. In this case, the time step is determined by diffusion time scales. However, if the smallest particle present in the system is 100 nm in diameter, the diffusion time scale reduces to $10^{-2}$ s and the viscous flow time scale remains at the order of $10^{-3}$ s. Thus, the global time scale is determined by that of viscous flow.

## 5.3 Pristine pulsed plasma results

In a plasma afterglow, the time scales of different events are very important. During the discharge's "on" phase, the walls become negatively charged because electrons are much more mobile than ions. As the discharge is switched on, there is a flux of electrons and ions to the walls. The steady state situation arises when the walls develop sufficient negative potential to equalize the electrons and ion fluxes. In this situation, electrons and ions tend to diffuse with one another, a phenomenon known as ambipolar diffusion. When the discharge is switched off, electrons and ions diffuse to the walls, reducing their densities. This results in the decay of space charge and the transition from ambipolar to free diffusion. The time scales of these events are important in understanding the dynamics of afterglow.

To analyze pristine dusty plasmas, two cases were considered. In the first, the time period was 10 μs (frequency = $10^5$ Hz); in the second, the time period was 100 μs (frequency = $10^4$ Hz). The duty cycle for both cases was 50%. In both cases, pressure is 13 Pa (100 mTorr), gas temperature is 300 K, RF voltage amplitude is 100 V, frequency is 13.56 MHz, and gas flow rate is 30 sccm of argon.

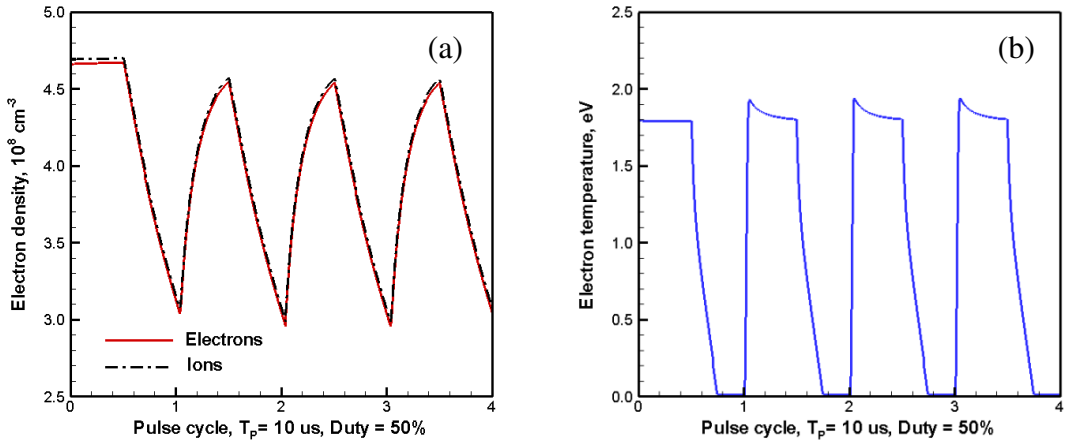


Figure 5.1: (a) Electron and ion density vs. pulse cycle and (b) electron temperature vs. pulse cycle at center for the case with pulse time period 10 μs and duty 50%

Figure 5.1 (a) and (b) shows electron and ion densities and electron temperature at center of discharge as function of pulse cycle number when the time period is 10 μs. "Time zero" corresponds to steady state discharge; at this time, electron and ion densities are around 4.7 x $10^8$ $cm^{-3}$ at the center. The discharge is turned off after the first half of the cycle, causing electron temperature relaxation within 2 μs. Because of this, electron and ion production by ionization is negligible, so electron and ion densities decay. Electron and ion density decay together because of the ambipolar diffusion caused by the residual sheath potential. As the discharge is switched on again at the beginning of next cycle, electron temperature begins to increase within 1 μs. It is important to note the spike in electron temperature. This spike has been reported in previous experiments and numerical models (85). Spike in electron temperature occurs to create a burst of ionization. Because of the increased ionization, electron and ion densities increase to 4.5 x $10^8$ $cm^{-3}$, which is less than their steady state value. The short (10 μs) pulse period prevents the electron

density from reaching its steady state value. In other words, 5μs is not sufficient for the plasma species densities and electron temperature to reach their steady state values.

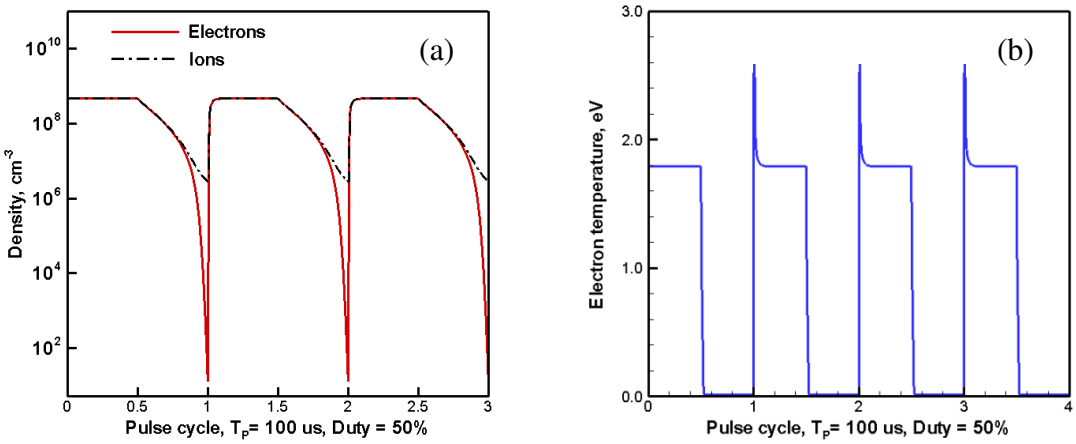


Figure 5.2: (a) Electron and ion density and (b) electron temperature vs. pulse cycle at center for the case with pulse time period 100 μs and duty 50%

Figure 5.2 (a) and (b) shows electron and ion densities and electron temperature as functions of pulse cycle number when the time period is 100 μs. Again, "time zero" corresponds to the point of steady state discharge. Once the discharge is turned off, electron temperature relaxes within 2.5 μs. Electron and ion densities decay together because of ambipolar diffusion; the transition from ambipolar to free diffusion occurs approximately 30 μs after the discharge is switched off (figure 5.2 (a)). Once the transition from ambipolar to free diffusion takes place, the electron density decays rapidly. When the discharge is turned back on at the beginning of the next cycle, electron temperature increases very quickly, as evidenced by the spike in electron temperature. Comparing the temperature profiles of figures 5.1 (b) and 5.2 (b) shows that electron temperature spike is stronger in the 100 μs case. This is because electron density is

reduced by 7 orders of magnitude in the 100μs case, compared to a factor of 0.6 in the 10μs case. It is also important to note that during the "on" phase of the discharge, both the electron and ion densities and electron temperature reach their steady state values in the 100 μs case, as opposed to the 10 μs case.

These two cases show that plasma afterglow results from a combination of events occurring at different time scales. The next section explains the importance of the time scales of different events in a dusty plasma afterglow.

## 5.4 Study of time scales

To understand the behavior of the system, it is important to know the time scales of processes such as electron and ion attachment to particles, electron temperature relaxation, and electron and ion diffusion in dusty plasma afterglow. As mentioned in the previous section, electron temperature relaxation occurs rapidly once the discharge is turned off. Given our simulation conditions, the time scale for electron temperature relaxation is around 1-3 μs, which has important consequences for particle charging. When the discharge is turned on, most particles are negatively charged. The time scale of electron/negative-particle attachment depends on the electron temperature. Time scales for charging were calculated using equations 2.8 and 2.9. If the electrons have high energy—for example, around 1 eV—the time scale for electron attachment to negatively charged particles is around 10 μs. However, when electron temperature relaxation has occurred (electron temperature equals approximately 0.025 eV), the time scale for electron attachment to negatively charged particles increases to 1s. The time scale for ion attachment to negatively charged particles (where ions are considered to be at same

temperature as background gas temperature), is around 10 μs. As discussed in the previous section, the time scale for transition from ambipolar electron/ion diffusion to free diffusion is around 30-50 μs, depending on simulation conditions. Once the transition from ambipolar to free diffusion takes place, electron free diffusion occurs on the order of a few μs, and ion diffusion occurs in tens of milliseconds. Free diffusion time scales for ions and electrons were calculated based on their diffusion coefficient and characteristic length of the system. Times scales of different processes for the simulations conditions mentioned in previous section are listed in table 5.1. For the calculations of charging time scales, particle diameter was assumed to be 50 nm carrying -10 charges.

Table 5.1: Time scales for different process

| Process | Time scale |
|---|---|
| Electron attachment to particle (Te ~1 eV) | ~ 1 μs |
| Electron attachment to particle (Te ~ 0.025 eV) | ~ 1 s |
| Ion attachment to particle (T ~ 300 K) | 10 μs |
| Electron diffusion | 10 μs |
| Ion diffusion | 10 ms |
| Ambipolar to free diffusion transition | ~ 40 μs |

From analyzing time scales, it may be concluded that in the dusty plasma afterglow, electron loss is primarily due to diffusion. Further, because of rapid electron energy relaxation, electrons do not contribute to particle charging. However, ions are lost primarily by attaching to dust particles.

## 5.5 Dusty plasma afterglow results

To understand the physics of dusty plasma afterglow, two cases are considered. The first corresponds to a stagnation flow profile, while the second corresponds to the no-flow case. The model simulates a 13.56 MHz capacitive RF argon-silane (30:1) plasma at a pressure of 17 Pa. The gap between electrodes is 4 cm, with the upper electrode powered and the lower electrode grounded. The applied RF voltage is 55V with a DC self-bias of -20 V. These conditions are same as in chapter 3 and 4.

### 5.5.1 Case with stagnation flow, t =5.0 – 5.1 s

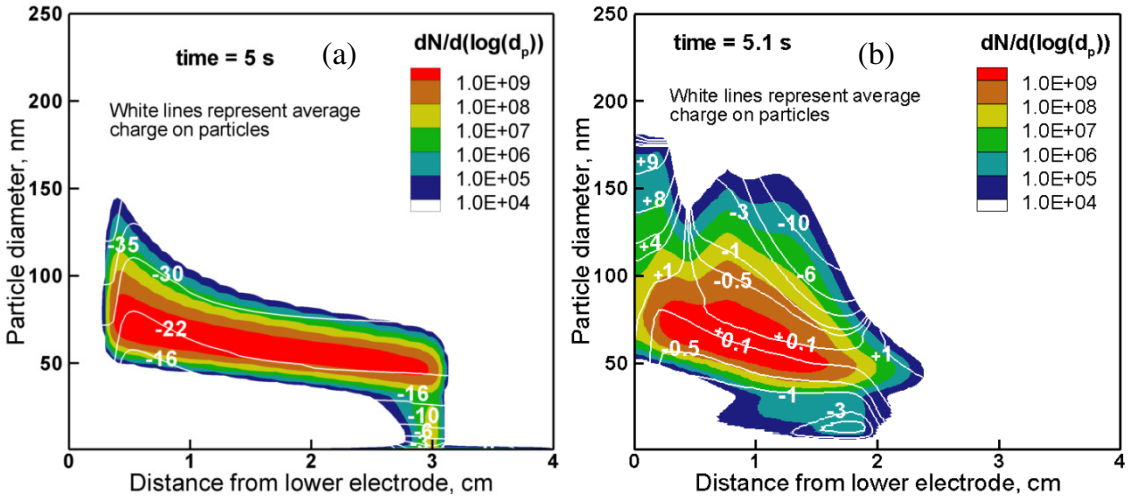


Figure 5.3: Behavior of particle cloud in afterglow in the case with stagnation gas flow: (a) particle size distribution and average particle charge at t = 7.125 s, at which time applied RF voltage is switched off; (b) corresponding profiles 100 ms later

At t=5.0 s, when the applied voltage is turned off; figure 5.3 (a) shows particle size distribution and average particle charge at this instant, and figure 5.3 (b) shows the same at 100 ms into the afterglow. Particles are no longer trapped once the voltage is turned

off, so the particle cloud is pushed toward the lower electrode by the gas flow coming from the upper electrode, which has a showerhead configuration.

Figure 5.3 (a) and 5.3 (b) clearly shows a significant change in particle size distribution and average charge. As mentioned earlier, system behavior in a dusty plasma afterglow depends strongly on the time scales of processes like electron and ion attachment to particles, electron energy relaxation, electron and nanoparticle diffusion, coagulation, and the electric field decay present at the instant the voltage is switched off. Several numerical models for dusty plasma afterglow, which are based on the time scales of these processes, have been developed (93,96). However, in the numerical model presented here, important processes are accounted for by the basic equations (Section 5.1) and the model is fully self-consistent.

The white contour lines in figure 5.3 (a) and 5.3 (b) show the average particle charge. Figure 5.3 (a) clearly shows that at the instant of voltage switch-off, particles are negatively charged. Large particles, therefore, are trapped between the two electrodes by electrostatic force. However, 100ms into the afterglow (Figure 5.3 (b)), most particles have been neutralized or even attained a positive charge. It is clear from figure 5.3 (b) that positive particle charging is most pronounced near the lower electrode, where ion density far exceeds electron density at the instant that applied voltage is switched off.

As discussed in the previous chapter, the sectional method is used to model the general dynamics equation. The sectional method allows one to account for particle size and charge distribution. If particles of a given size have a broad distribution of charge states,

it is clear that the charge distribution of dust particles in figure 5.3 (b) is essentially bipolar. Even for regions and particle sizes where the average charge is close to zero, most particles are charged. For example, figure 5.4 (a) and (b) shows the charge

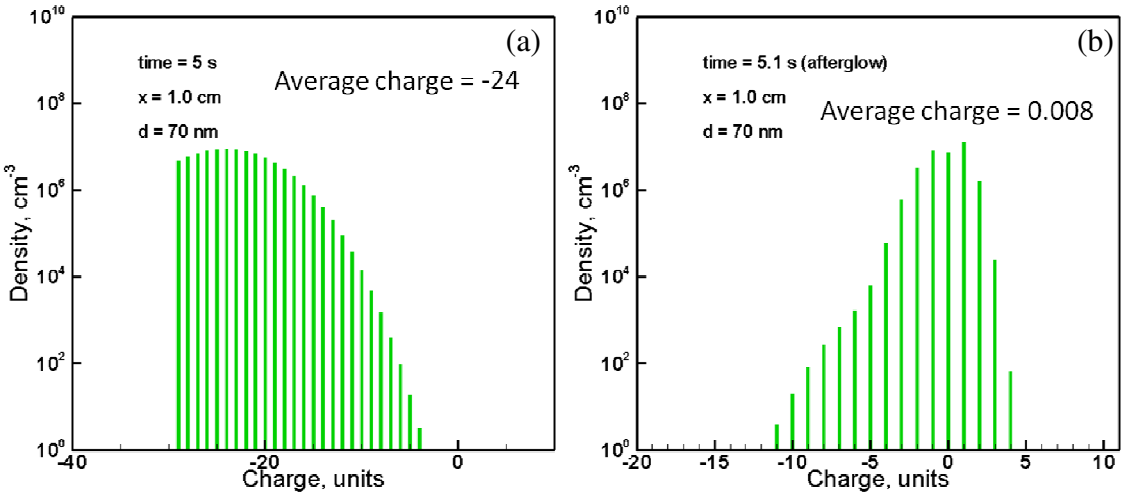


Figure 5.4: Charge distribution at (a) the instant of voltage switch off t = 5.0 s and (b) 100 ms into afterglow i.e t=5.1 s

distribution at the instant of voltage switch-off, and 100 ms into the afterglow phase, for those 70 nm diameter particles which are located at x = 1.0 cm. In figure 5.4 (a), all particles are negatively charged, with an average charge is -24. Conversely, average particle charge in figure 5.4 (b) is close to zero (0.008), but only 21% of these particles are neutral; most (43%) are positively charged. The bipolar distribution of particle charge states results in enhanced coagulation between oppositely charged particles. The rapid growth of particles observed in figure 5.3 occurs because of coagulation, which broadens the particle size distribution. Figure 5.5 (a) and (b) show the particle size distribution at x

= 1 cm for the two instants. Comparing figure 5.5 (a) and (b) cm shows that particle size distribution is much broader in the afterglow than at the instant of voltage switch-off.

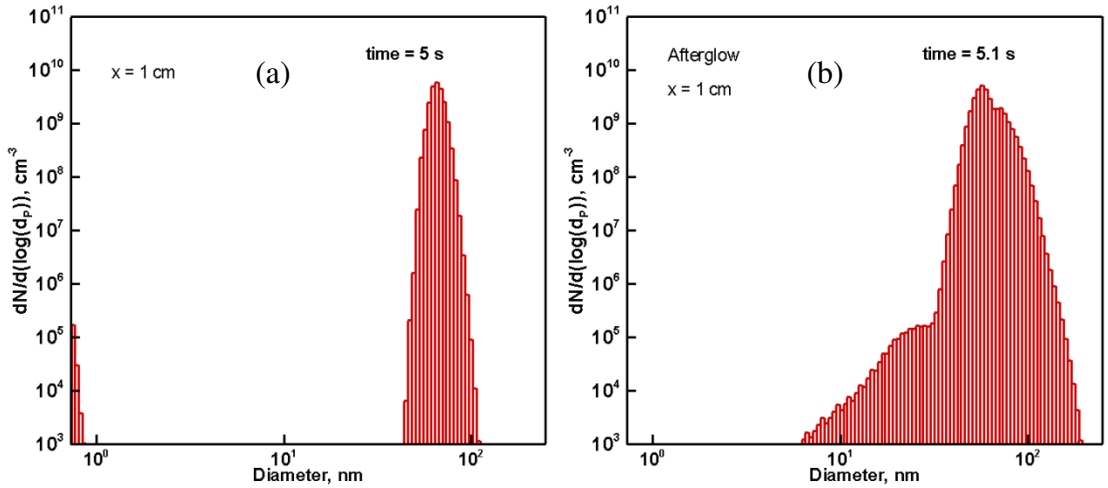


Figure 5.5: Particle size distribution at x= 1 cm at (a) the instant of voltage switch off and (b) 100 ms into afterglow

## 5.5.2 Case with no gas flow, t = 7.125 s , 7.2 s, 7.7 s

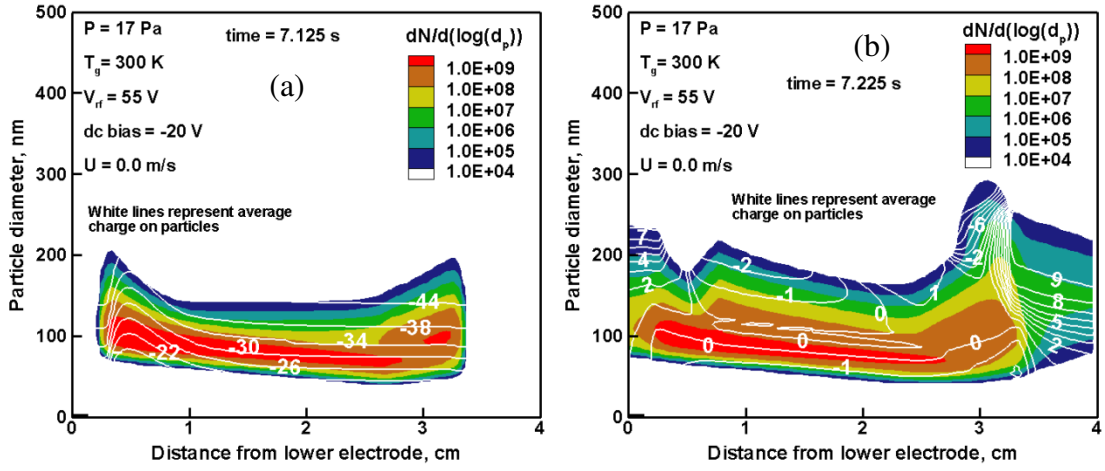


Figure 5.6: Behavior of particle cloud in afterglow in the case with no gas flow: (a) particle size distribution and average particle charge at t = 7.125 s, at which time applied RF voltage is switched off; (b) corresponding profiles 100 ms later

The case with no gas flow is particularly interesting. Because no gas flow means there is no neutral drag force, dust particles remain in the reactor longer, and are lost to electrodes because of gravity and diffusion. For this case, the discharge was turned off at t=7.125 s. Particle size distribution and average charge are shown at this instant in figure 5.6 (a), and after 100 ms of afterglow (i.e. 7.225 s) in figure 5.6 (b). At the instant of voltage switch-off (figure 5.6 (a)), dust particles are trapped in the reactor and average charge is negative. 100 ms into afterglow, particles have largely lost their negative charge, so they tend to diffuse towards both electrodes as shown in figure 5.6 (b). Figure 5.6 (b) also shows that particles tend to gain positive charge near the electrodes; this occurs because of the higher ion densities near the walls at the instant of voltage switch-off.

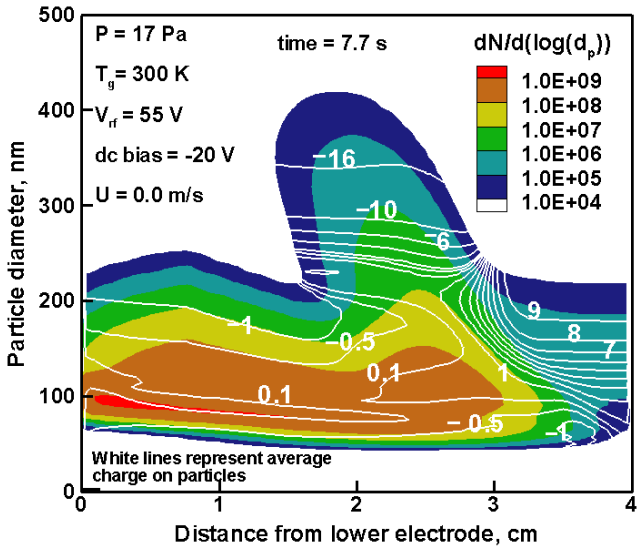


Figure 5.7: Particle size distribution and average charge for the no gas flow case at 7.7 s i.e. 575 ms into afterglow

The previous section stated that in the afterglow, dust particles grow rapidly by coagulation and become bipolar due to ion charging. In the "no-flow" case, particle

residence time in the reactor is around 2 seconds, which is much higher than the "gas flow" case (300 ms). This yields interesting features at later times in the "no gas flow" case. For example, figure 5.7 shows the particle size distribution and average charge at 7.7 s, i.e. 575 ms into the afterglow. These particles' high residence time makes them more likely to coagulate, so their size distribution broadens significantly. Figure 5.8 (a) and (b) shows the particle size distribution at midplane at the instant of voltage switch off and 575 ms into afterglow. Comparing the size distributions of figures 5.8 (a) and (b), it is clear that at the instant of voltage switch-off, particles of diameter ranging from 43 nm to 168 nm are present at the midplane. After 575 ms of afterglow, however, particle diameter ranged from 39 nm to 480 nm at the midplane.

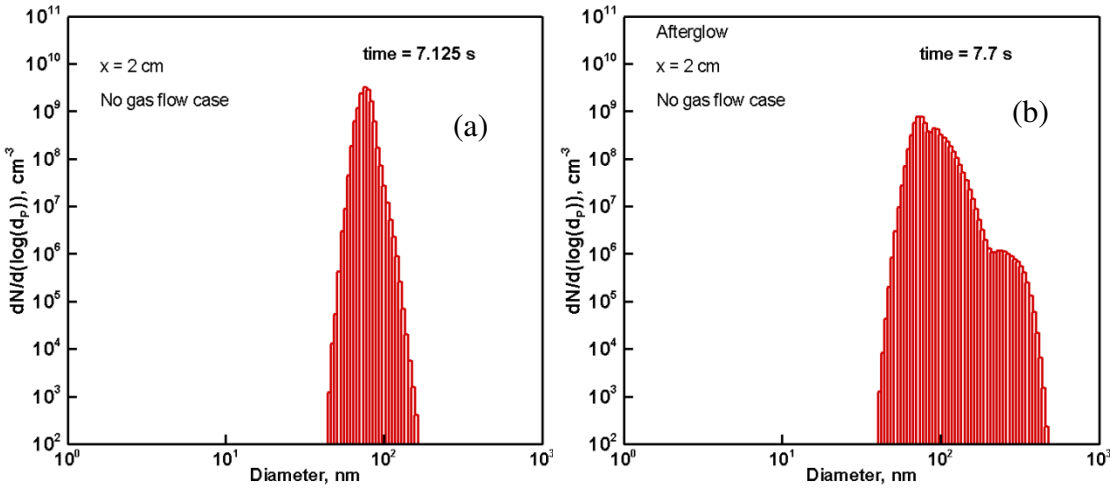


Figure 5.8: Particle size distribution at x= 1 cm at (a) the instant of voltage switch off and (b) 575 ms into afterglow

Coagulation plays a small role in the growth of particles in dusty plasmas. This is because larger particles are negatively charged when the discharge is on, and coagulation is only important between these large particles and very small neutral particles. In the afterglow,

however, the charge distribution of dust particles is bipolar because of ion charging and rapid electron energy relaxation. Therefore, there is significant coagulation between large, oppositely-charged particles in the afterglow. This results in significant growth. Comparing figures 5.6 (a) and 5.7 shows that particles of size up to 200 nm (figure 5.6 (a)) at the instant of voltage switch off have grown beyond 400 nm (figure 5.7) by coagulation after 575 ms of afterglow

As discussed in Chapter 3, it is necessary to study dusty plasmas' size and charge distribution to understand their underlying physical processes. The discussion in this section shows that considering the charge and size distribution of dust particles is important to model the physics of afterglow.

## 5.6 Pulsed dusty plasma results

Pulsed dusty plasmas are of increasing interest for control of plasma—and potentially nanoparticle—properties. Pulsed dusty plasma was simulated using the numerical model described in Section 5.1. A few authors have attempted to model dusty plasma afterglow in recent years (93,96-98), but to the best of our knowledge, no self-consistent model for pulsed dusty plasmas is reported in the literature. In this section, two cases with pulse frequency 1666 Hz and 10 Hz have been considered. Simulation conditions are the same as in Section 5.5, and the gas flow is assumed to have a stagnation profile.

Figure 5.9 (a) shows the electron density, ion density and net negative particle charge at the central axial position as a function of pulse cycle when pulse frequency is 1666 Hz and duty cycle is 50%. Figure 5.9 (b) shows the electron temperature at the central axial

position as a function of pulse cycle for the same case. Here, “time zero” corresponds to pristine, steady-state plasma. At “time zero,” particles start to nucleate and grow. The figure shows that as negative particle charge increases during the “on” phase of discharge, ion density must increase to maintain quasi-neutrality. Once the discharge is switched off, electron temperature relaxation occurs in 2.5 μs, which is similar to the pristine plasma case. In the model presented here, super-elastic collisions are neglected, though it is possible that they cause electrons to retain their energy for a longer time in afterglow(85). Further research is needed to discern any effects.

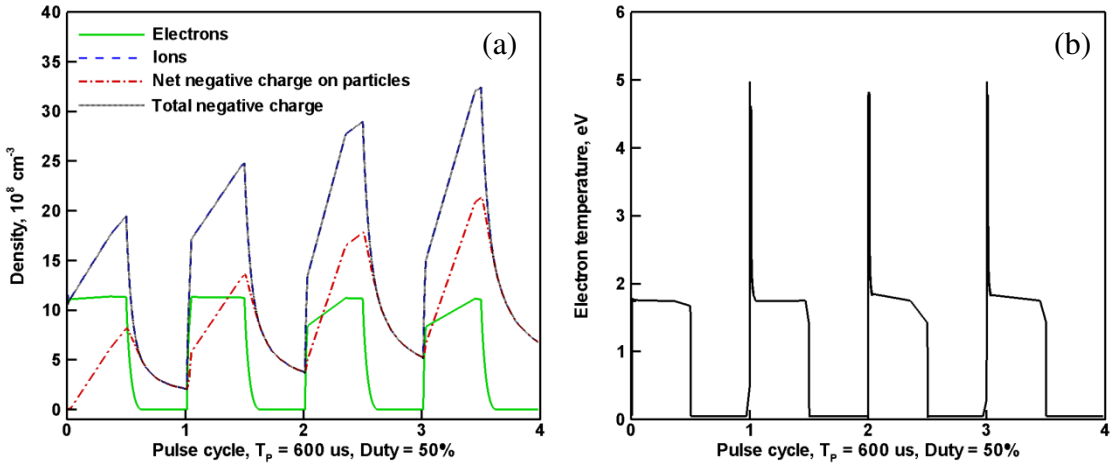


Figure 5.9: (a) Electron, ion and net negative particle charge density and (b) electron temperature vs. pulse cycle at center (x = 2 cm) for the case with pulse time period 600 μs and duty 50%

The nature of ambipolar diffusion is interesting in dusty plasma conditions. As the discharge is turned off, electrons, ions, and charged particles tend to diffuse with one another. This is illustrated by figure 5.9 (a), which shows that the net positive charge (given by ion density) and net negative charge (given by negative particle and electron densities) decay together. As the space charge decreases, highly mobile electrons make a

transition to free diffusion, while ions and charged particles continue to diffuse together because of the space charge electric field. To understand the importance of the space charge electric field, we simulated afterglow without solving Poisson's equation. In simulations without Poisson's equation, electrons, ions, and charged particles diffuse freely once the discharge is switched off as seen in figure 5.10.

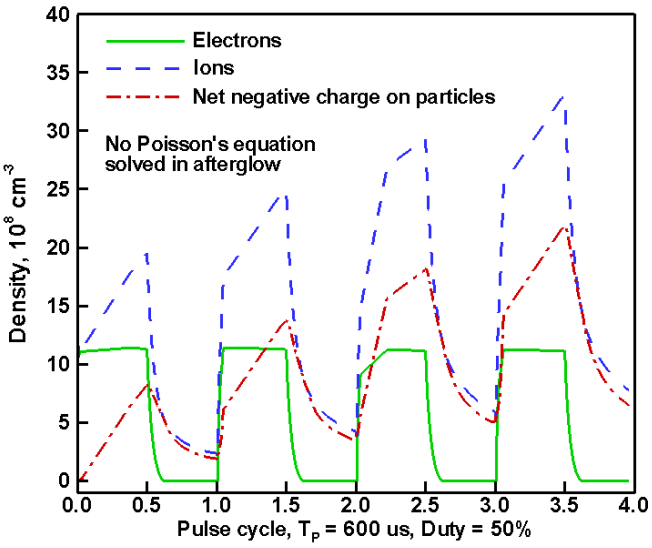


Figure 5.10: (a) Electron, ion and net negative particle charge density vs. pulse cycle at center (x = 2 cm) for the case with pulse time period 600 μs and duty 50%. In this case Poisson's equation was not solved.

The slopes of the curves of electrons, ions and net negative particle charge density (figure 5.9 (a)) when the discharge is on are related to particle nucleation and growth. As particles nucleate and grow, they continue to consume electrons. Therefore, during the "on" phase of pulse cycle #3 (i.e., 2 to 2.5) in figure 5.9 (a), the increase in electron density slows; this trend repeats during the "on" phase of cycle #4 (i.e. 3 to 3.5).

Figure 5.9 (b) shows that electron temperature rises much higher in dusty plasma than in pristine plasma (figures 5.1 (b) and 5.2 (b)). This occurs to create a burst of ionization with which to generate electrons. Since particles consume electrons within time scales on the order of microseconds, electron temperature must rise much higher to maintain a sufficient electron population to maintain plasma. Note that our model does not consider silane and argon metastable chemistry; a spike in electron temperature may have important consequences on electron impact reactions when these species are included.

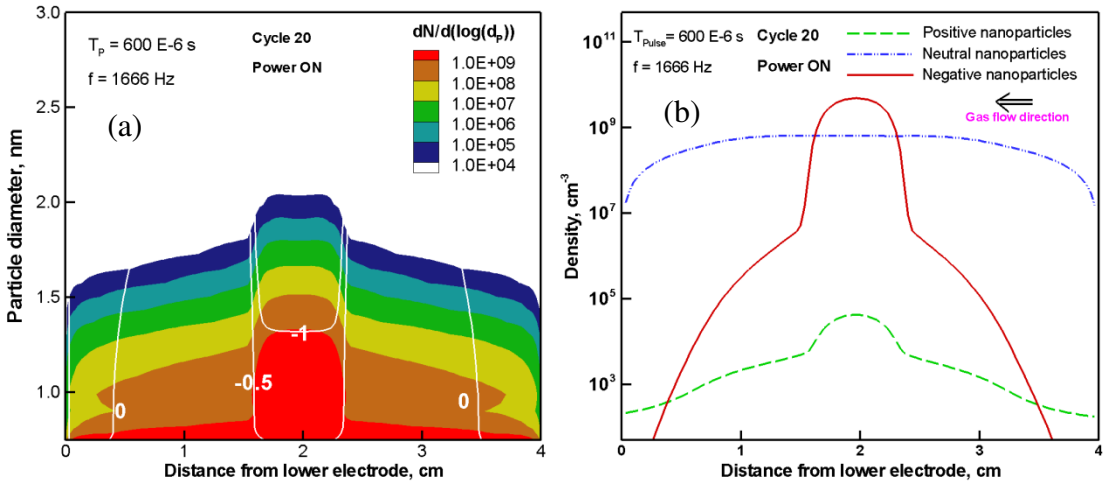


Figure 5.11: (a) Particle size distribution and average charge and (b) positive, neutral and negative nanoparticle densities during the ON phase of pulse cycle 20 where pulse period is 600 μs and duty is 50%

Figure 5.11 (a) and (b) shows particle size distribution, as well as average charge and density of positive, negative, and neutral particles when the discharge is on. Conversely, figure 5.12 (a) and (b) shows these values when the discharge is off. Figure 5.11 clearly shows that negatively-charged particles of up to 2 nm and of unity negative charge are trapped when the discharge is on, and diffuse toward the electrode when the discharge is off (figure 5.12). When the discharge is on, negatively-charged particles are trapped in

the center by electrostatic forces, while positive and neutral particles are not trapped (figure 5.11). When the discharge is switched off, the electric field disappears, so negatively charged particles diffuse towards electrodes (figure 5.12). This particular phenomenon may be interesting for processes requiring controlled deposition of small particles. By changing several pulse parameters such as pulse frequency and duty cycle, one can have better control over the process.

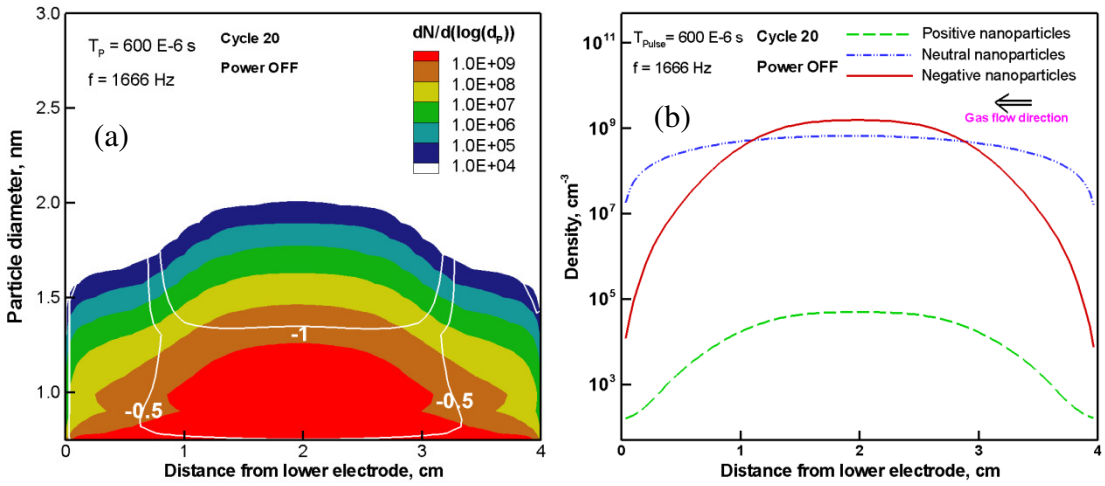


Figure 5.12: (a) Particle size distribution and average charge and (b) positive, neutral and negative nanoparticle densities during the ON phase of pulse cycle 20 where pulse period is 600 μs and duty is 50%

## 5.7 Summary

A self-consistent numerical model was developed to study the spatiotemporal behavior of dusty plasma afterglow and pulsed dusty plasma. Particle size and charge distribution were obtained using a sectional model. The varying time scales of different processes, such as electron/ion charging or diffusion, are important. In the afterglow phase, electrons' rapid energy relaxation and diffusion cause particle charging to be driven mainly by ions. Consequently, the dust charge distribution is bipolar, which causes

coagulation between large, oppositely-charged dust particles, in turn causing particles to grow rapidly. Finally, we discuss the space charge electric field's important effect on the ambipolar diffusion of electrons, ions, and charged particles. Pulsed dusty plasmas are important, and may offer exciting opportunities for the controlled deposition of small nanoparticles.

# Chapter 6: Numerical modeling of chemically reactive argon silane dusty plasmas

Argon-silane plasmas are commonly used for the plasma enhanced chemical vapor deposition (PECVD) of amorphous silicon thin films for solar cell applications (103), thin film transistors used in liquid crystal displays (104) and light emission devices (105). Nanoparticle formation may occur as a result of series of polymerizing reactions in such chemically reactive plasmas. Depending on application, these particles can either be useful or harmful. For example, particles formed in the thin film deposition of amorphous silicon are considered as harmful particles and their formation is undesired (6). On the other hand, particles are deliberately synthesized in argon-silane plasmas for applications in optoelectronics (14). Argon-silane dusty plasmas are highly complex and involve several phenomena like gas phase chemical reactions, heterogeneous surface reactions, particle transport, charging and coagulation. These different phenomena are coupled to each other. For example, particle transport and charging affects gas phase chemistry. Similarly formation and growth of dust affects the electron density and temperature which in turn affects gas phase chemistry. Therefore a good understanding of spatiotemporal behavior of such plasmas is required to control the process of particle formation.

Argon-silane dusty plasmas have been subject of extensive experimental (16,70,106) and numerical (41,42,78) research. Bouchoule and Boufendi (70) performed laser light scattering, light emission and particle collection measurements to understand the particle

formation, growth and its effect on plasma properties. They concluded from their emission experiments that the presence of dust particles affects the plasma properties. From the analysis of their laser light scattering experiments and particle collection measurements they suggested a three step process of particle growth. They suggested that high concentrations of small crystallites (2 nm) are formed as the initial step. This step is followed by coagulation of these small crystallites leading to the formation of small particles of size around 50 nm. Coagulation ceases as these particles become increasingly negatively charged. Particles then grow by surface deposition of small radical species. Their theory was based on two key observations from particle collection and laser light scattering measurements. As the particle size increases, particle concentration dropped while no change was observed in the particle mass concentration. Second observation was based on images of particle by transmission electron microscopy. In the images, particles (~40 nm) appreared to be clusters of small crystallites. These observations are important however dusty plasmas are highly complex and there might be some other factors related to chemistry like variable growth and nucleation rate which can cause similar effects.

Kushner (41) developed a 1D hybrid fluid-kinetic numerical model of argon silane plasmas for PECVD of amorphous hydrogenated silicon (a Si:H) in RF and DC discharges. His model considered extensive silane chemistry. He considered electron impact reactions, neutral-neutral reactions, ion-ion reactions and ion-neutral reactions in their reaction set. The rate constants for electron impact reactions were obtained from a Monte Carlo simulation. They also considered the formation of dust particles however

their simulation was limited to gas phase chemistry and did not account for dust transport, charging and growth.

Belenguer et al (42) performed fluid and particle in cell-Monte Carlo (PIC-MC) simulations for pure and dusty argon plasmas. Concentration and size of dust particles were taken from experimental measurements of argon-silane plasmas. Their model included particle charging however particle transport, coagulation and silane chemistry were not included. They found that presence of dust particles in the plasma results in the change in impedance of the discharge and the discharge becomes more resistive.

Bhandarkar et al (21,78) developed a 0D model for argon silane plasmas. They developed a detailed silane chemistry model for silicon hydride clustering in argon silane plasma and coupled it to a sectional aerosol dynamics model for coagulation and surface growth of particles. They considered more than 300 species and 5500 reactions in their extensive model for particle formation and growth. They found that the main precursors in nucleation pathway leading to particle formation are silyl and silylene anions. They also found that the delay in particle nucleation on the increase of gas temperature is due to the strong temperature dependence of Brownian diffusion coefficient and thus the increased diffusion loss of chemical species.

De Bleecker et al (47,60) modeled silane dusty plasmas using sectional method for particle size distribution. Their numerical model was 1D and self consistently coupled to a plasma fluid model. They used a modified version of detailed chemistry mechanism in (21) to model particle formation. Particle charge distribution was not modeled rather

particle charge was calculated by equating the ion and electron currents. They did not account for charge dependent coagulation and surface growth of particles. They found that silyl anions are the most important species in particle formation. They also studied the particle transport and analyzed the importance of different forces in silane plasmas. Their results were presented in terms of spatial distribution of various quantities without any indication of time dependence.

Girshick and coworkers (23,24) developed a numerical model to model a dusty argon plasma containing silicon nanoparticles. They used sectional method to simulate the dust particle size and charge distribution. Their dust particle model was self consistently coupled to a plasma fluid model, including the solution of Poisson's equation for electric field. Their model accounted for plasma-particle interaction, particle transport, coagulation, charging, surface growth and nucleation. Particle formation and growth chemistry was not modeled rather nucleation and surface growth rates were taken as input parameters. Effect of image potentials was considered in neutral charged particle coagulation. They presented the spatiotemporal behavior of dust particle size distribution and plasma. They also found that coagulation is important between very small neutral particles and large negatively charged particles enhanced by the image potential in neutrals.

More recently, Liu et al (107) developed a self consistent 2D fluid model for silane dusty discharges. Their model is similar to the one developed by De Bleecker et al (47). Liu et al (107) used sectional method to describe the dust particles and coupled it to fluid plasma model including the particle formation chemistry. Similar to the model of De

Bleecker et al (47), particle charge distribution was not modeled and coagulation was not considered charge dependent. Surface growth was not modeled. Their results were presented in terms of particle density in two dimensions.

In this work, numerical model developed by Girshick and coworkers (23,24) has been extended by the addition of simplified silane chemistry for particle formation and surface growth. Nucleation and surface growth rates are obtained from the chemistry model. This numerical model self consistently accounts for particle-plasma interaction, particle formation and growth chemistry, coagulation, charging/decharging and particle transport. Numerical mode is discussed in detail in chapter 2. A detailed discussion of spatiotemporal evolution of dust particle cloud, chemical species and plasma properties is given in the following section.

Simulation conditions consist of 13.56 MHz RF argon-silane (30:1) plasma at a pressure of 13 Pa, contained between parallel plate with a 4-cm gap. The top electrode is powered and showerhead whereas the lower electrode is grounded and solid. The applied voltage amplitude equals 100 V and the model self consistently accounts for DC bias by making the net current zero at the top electrode. Gas flows through the top electrode with a velocity of 0.263 m/s corresponding to a flow rate of 31 sccm through an electrode with a diameter of 12 cm. Stagnation flow profile is assumed for the velocity profile.

## 6.1 Results

The spatiotemporal evolution of chemical species and the dust particle cloud is described at three different times namely 0 s, 1 s and 5 s.

### 6.1.1 Case 1, t = 0 s

The time 0 here represents the steady state pristine plasma with all the gas phase species. Spatial profiles of charged and neutral chemical species are shown in figure 6.1. Figure 6.1 (a) shows the spatial profiles of charged species whereas figure 6.1 (b) shows the spatial profiles for neutral species (silane, silyl and silylene radicals, argon metastables) at 0 seconds. At this instant, there are no particles and silane has been partially dissociated. These profiles represent the steady state solution of argon-silane plasma with no particles. Most of the species are created by the inelastic collision of electrons with their parent molecules therefore the species concentrations follow the electron concentration profile to some extent and their concentration is higher in the bulk of plasma outside the sheaths (figure 6.1 (a) and (b)).

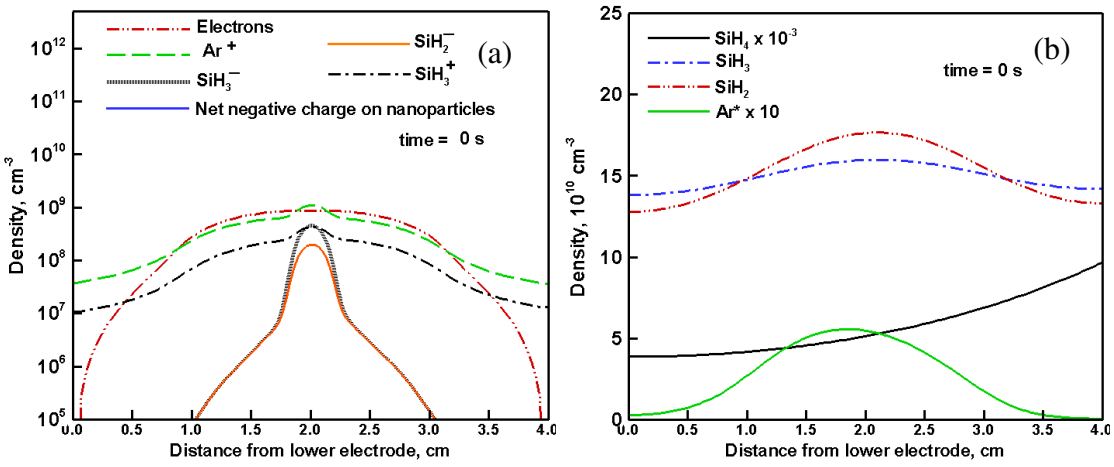


Figure 6.1: Spatial profiles of (a) charged species and (b) selected neutral species at time 0 s

The asymmetry in the profile of argon metastable is related to the spatial profile of silane (figure 6.1 (b)). Silane concentration is fixed at inlet and as it flows through the reactor, it

gets dissociated into radicals and ions and therefore its concentration is lower near lower electrode. Silane reacts with argon metastables to create silyl and silylene radicals. Argon metastables are produced in the bulk of plasma by inelastic collision of electrons with argon molecules therefore argon metastables have higher concentration outside the sheaths. Near the upper electrode i.e. the gas inlet, higher concentration of silane results in higher consumption of argon metastables. Because of lower concentration of silane near lower electrode, argon metastables in the lower electrode sheath have concentration slightly higher than that in the upper electrode sheath.

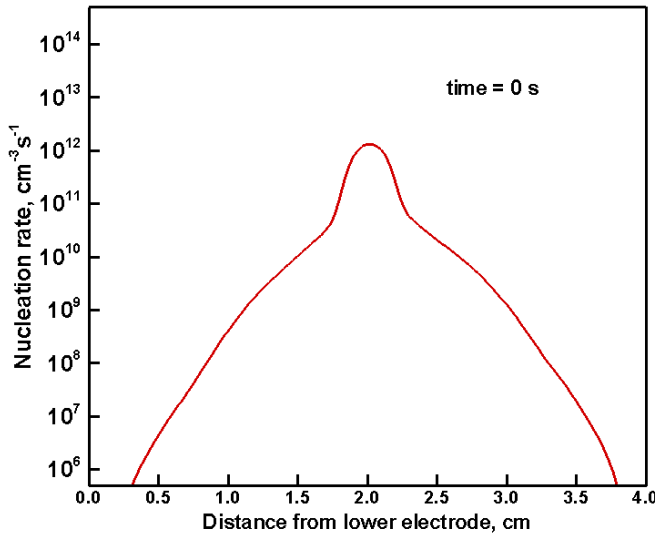


Figure 6.2: Spatial profile of nucleation rate at time 0 s

Profile of nucleation rate at t = 0 s is shown in figure 6.2. Anion-neutral reactions are the main pathways leading to particle formation (21). Bhandarkar et al (21) found that $Si_2H_5^-$ and $Si_2H_4^-$ are the main precursors in reaction pathways leading to particle formation. Therefore, in the chemistry model considered here, nucleation is simply the rate of

reactions involving silyl and silylene anion with silane. Therefore, nucleation profile follows the profile of silyl and silylene anions. Since no particles are present at time zero, surface growth is not included here. Time 0 is considered to be the time for onset of nucleation.

### 6.1.2 Case 2, t = 1 s

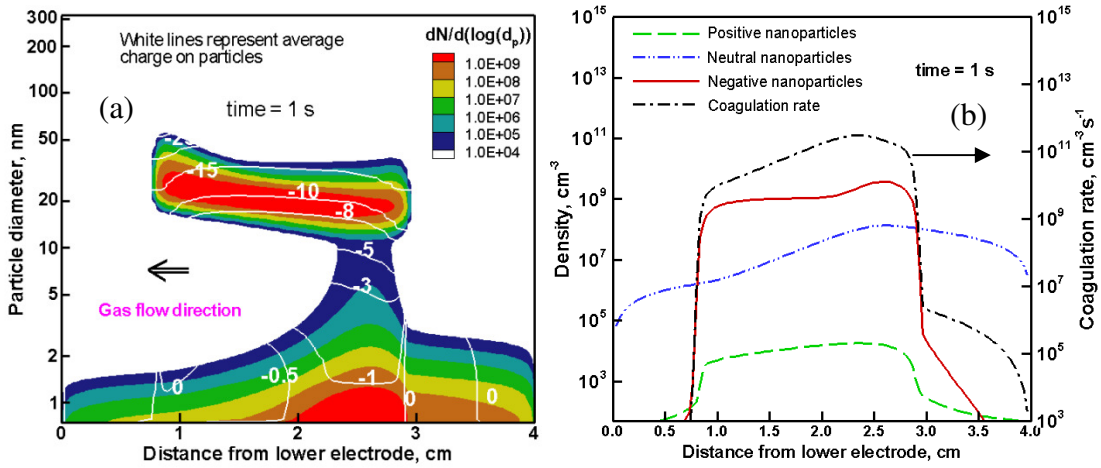


Figure 6.3: (a) Particle size distribution and average charge and (b) spatial profiles of neutral, negative and positive particle density and coagulation rate at 1 s

Figure 6.3 (a) shows the particle size distribution and average charge on particles at 1 s. At this instant particles that are negatively charged and trapped have a mean diameter of 27 nm at x = 1 cm. Negatively charged particles are trapped because of the action of electric force. It is clear from figure 6.3 (a) that larger particles are pushed towards lower electrode because of the neutral drag. Neutral particles are not trapped and therefore tend to diffuse towards walls. Particle distribution is clearly bimodal. Two separate populations are formed because of ongoing nucleation, coagulation and surface growth. Figure 6.3 (b) shows the density of neutral, negative and positive particles and the

coagulation rate profile at 1 second. It is clear from figure 6.3 (b) that high density of negatively charged particles is present at 1 s. Since the particles are still being formed by fresh particle nucleation, stochastic charging for small particles (size < 2 nm that can carry maximum 1 charge) results in a population of both neutral and positive particles.

Coagulation at this instant is important between large negatively charged particles and small neutral particles enhanced by image potentials in neutrals. Figure 6.3 (b) shows that coagulation profile follows the neutral particle density as well as negative particle density profile. Coagulation is mainly important outside the sheaths as seen in figure 6.3 (b) because of presence of high concentration of negative and neutral particles. Coagulation profile outside the sheath region nearly follows the neutral particle density profile. Peak in the profile of coagulation rate occurs at x = 2.4 from lower electrode which is close to the peak in neutral particle concentration profile. Coagulation within the sheaths follows negative particle concentration profile as seen in figure 6.3 (b).

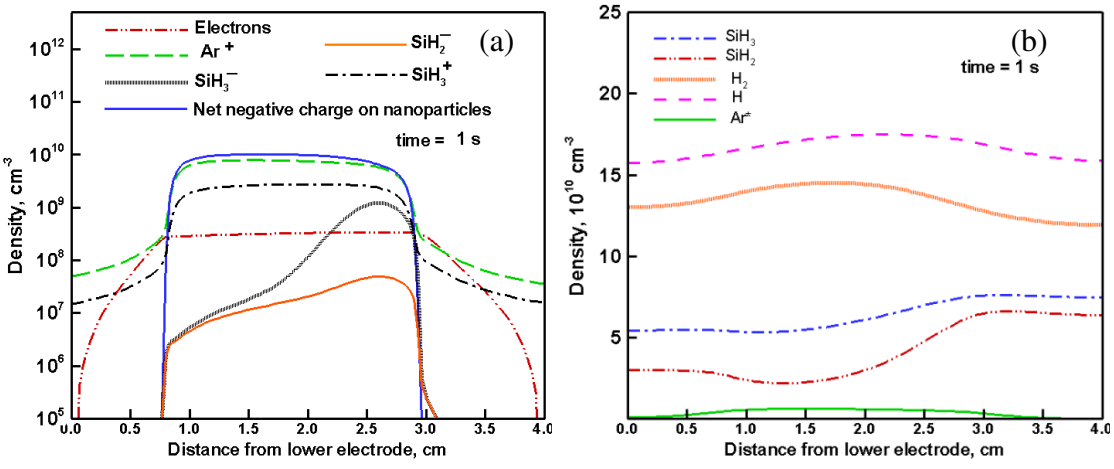


Figure 6.4: Spatial profiles of (a) charged species density and (b) neutral species density at 1 s

Figure 6.4 (a) and (b) show the density of charged and neutral species at 1 s. As the particles grow bigger they consume electrons and therefore electron density is lower than positive ion species density. At this instant as seen in figure 6.4 (a), net negative charge on particles density is on the order of $10^{10}$ $cm^{-3}$ and the electron density is on the order of 3 x $10^{8}$ $cm^{-3}$. It is interesting to note the profiles of silyl ($SiH_3^-$) and silylene ($SiH_2^-$) anions. Profiles of silyl and silylene anions are related to the profiles of silyl ($SiH_3$) and silylene ($SiH_2$) radicals in figure 6.4 (b). Silyl and silylene radicals are the main precursors for surface growth. It is clear from figure 6.4 (b) that silyl and silylene radicals are consumed near lower electrode because of the presence of large surface area of particles near lower electrode (figure 6.5). As seen in figure 6.5, surface area density at 1 s peaks at x = 1.38 cm from lower electrode, minima in the concentration of silyl and silylene radicals occur exactly at 1.38 cm from lower electrode. Similarly, the concentration of silyl and silylene radicals peaks outside the sheaths where small neutral particles are present and the particle surface area is smallest.

Figure 6.4 (b) shows the hydrogen and atomic hydrogen concentration. Atomic hydrogen is created by the electron impact dissociation of silicon hydrides and hydrogen gas. The atomic hydrogen concentration maximizes at x = 2.3 cm which lies in between the maxima of hydrogen density (x = 1.75 cm) and the density of silyl and silylene radicals (x = 3.0 cm). Hydrogen gas is generated by surface reactions and the anion neutral reactions. Maximum of hydrogen density lie in between the maximum of particle surface area density (x= 1.38 cm, figure 6.5) and the maximum of silyl and silylene anions (x=2.6 cm).

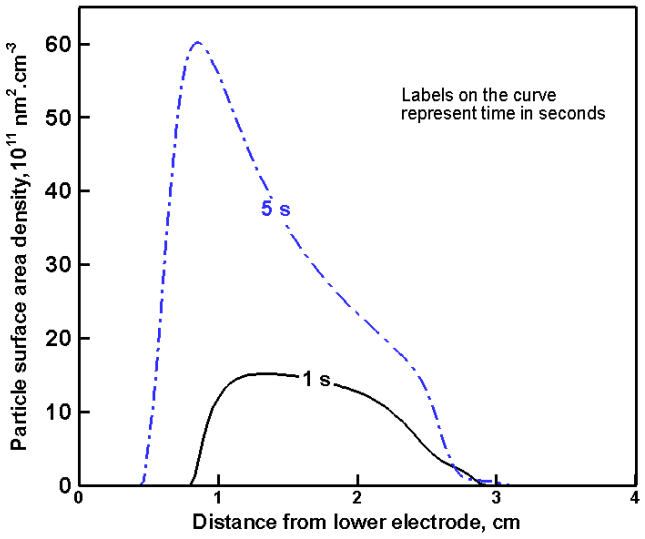


Figure 6.5: Spatial profile of particle surface area density at 1s and 5s

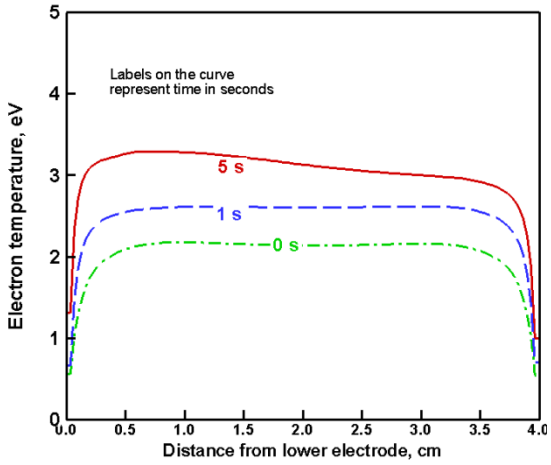


Figure 6.6: Spatial profiles of electron temperature at 0 s, 1 s and 5 s

As seen in figure 6.4 (a), density of silyl anion is greater than electron density near upper electrode. Similarly, silyl positive ion density is on the order of $10^9$ cm$^{-3}$. As the particles consume electrons, negative charge on particles increases and the electron density decreases. This results in increase in electron temperature to generate more electrons and

ions as seen in figure 6.6. Figure 6.6 shows the electron temperature at 3 instants namely 0 s, 1 s and 5 s. Increase in electron temperature results in increased ionization of silane and electron attachment to neutral species. Therefore, there is an increase in the density of silyl positive ions as compared to the same at time zero. In comparison to time 0 s, the density of silyl anion is increased near upper electrode because the density of silyl radical is higher near upper electrode and increase in electron temperature results in increase in electron attachment to silyl radicals. However, silyl anion density is lower in the lower half of reactor because of consumption of silyl radicals by particles in the lower half of reactor as mentioned previously.

Figure 6.7 (a) shows the spatial profile of nucleation rate. As mentioned earlier, nucleation rate profile follows the profiles of silyl and silylene anions. Nucleation profile peaks at x = 2.6 cm from lower electrode. Profiles of silyl and silylene anions also peak exactly at x = 2.6 cm. Nucleation rate equals the rate of reaction of silyl and silylene anions with silane. It was mentioned earlier, silyl and silylene anions follow the profiles of silyl and silyene radicals. As the large dust particles are pushed towards lower electrode, they consume the reactive silicon species from that region and therefore nucleation rate is higher in the relatively particle free regions.

Figure 6.7 (b) shows the profile of surface growth rate along with the profiles of silyl and silylene radicals at 1s. Profile of surface growth is related to the profile of silyl and silylene radicals. Surface growth is enhanced by the dipole-dipole interaction between large negatively charged particles and small neutral silyl and silylene radicals. Negatively charged particles are trapped outside the sheaths therefore surface growth is important

only outside the sheath region. It was mentioned earlier that the concentration of silyl and silylene radicals is lower in the region where particles surface area is higher and peaks in the particle free regions. Surface growth rate follows the similar behavior and its minima coincides with the minima (x = 1.38 cm) in profiles of silyl and silylene radicals (figure 6.7 (b)).

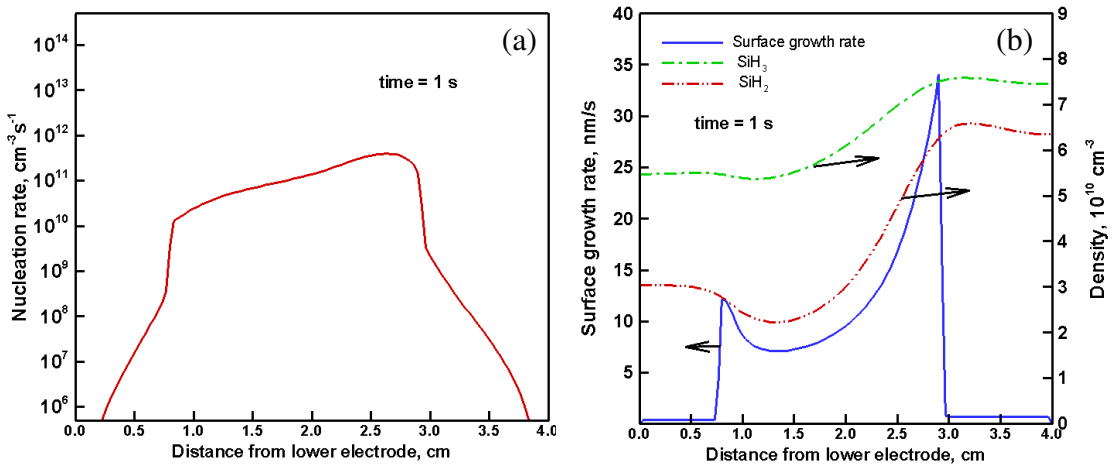


Figure 6.7: Spatial profiles of (a) nucleation rate and (b) surface growth rate and density of silyl and silylene radicals

### 6.1.3 Case 3, t = 5 s

Figure 6.8 shows the particle size distribution and average charge at 5 s. At this instant, particles have a mean diameter of 46 nm at x = 1 cm. As the particles grow bigger, they are pushed towards lower electrode because of neutral drag. Ion drag becomes important for larger negatively charged particles. Ion drag force pushes particles out from the center of discharge towards both the electrodes. Presence of large particles of size greater than 50 nm near upper electrode at around x = 3 cm is due to the action of ion drag force. It is interesting to note the behavior of white colored contour lines in figure 6.8 representing

the average charge. The curvature around x = 1 cm in these contour lines indicates that particles have become less negatively charged near lower electrode. For example, 45 nm (diameter) particle at x = 1 cm from lower electrode carries 12 negative charges, however

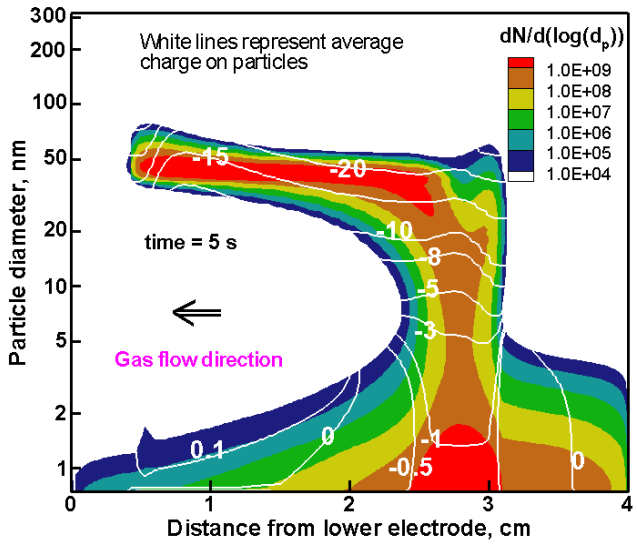


Figure 6.8: Particle size distribution and average charge at 5 s

the same diameter particle at x = 2 cm carries 20 negative charges. As the particles become bigger, they consume more and more electrons and the electron density is approximately two orders of magnitude lower than the ion density at around x = 1 cm. Ion to electron density ratio at x =1 is higher than the same at x = 2 cm. This results in particles being less negatively charged near lower electrode.

Figure 6.9 (a) and (b) show the spatial profiles of charged species and neutral species. It is clear from figure 6.3, 6.4, 6.8 and 6.9 that dust particles are strongly coupled with plasma. Growth and dynamics of dust particles strongly influences the profiles of chemical species. As particles grow and spatially spread in the reactor, they consume

these chemical species including electrons and therefore concentration of these species is changed. At 5 seconds, particles have grown bigger and their surface area has increased in comparison to the same at 1 s (figure 6.5). Therefore the concentration of electrons, silyl anion, silylene anion, silyl and silylene radicals has reduced near lower electrode at

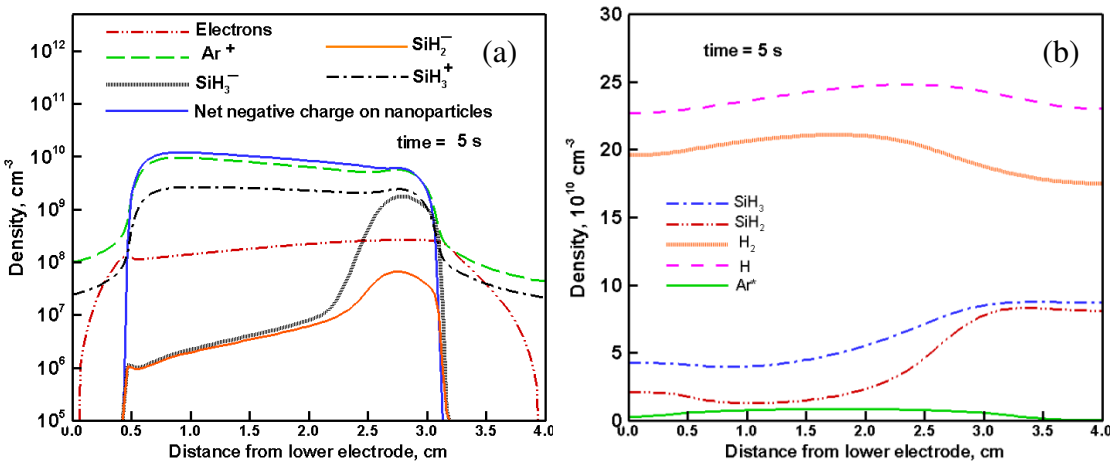


Figure 6.9: Spatial profiles of (a) charged species and (b) neutral species at 5 s

5 seconds in comparison to 1 s (figure 6.4 (a) and figure 6.9 (a)). As seen in figure 6.6, electron temperature at 5 s has increased in comparison to 1 s and 0 s. For example, at x =1 cm, electron temperature is 2.1 eV, 2.6 eV and 3.2 eV at 0 s, 1 s, and 5 s respectively. Electron temperature increases to maintain ionization in response to depletion of electrons and increase in net negative charge on dust particles.

Figure 6.10 shows the density of argon metastables at 0 s, 1 s and 5 s. Concentration of argon metastables increases because of increase in electron temperature. Although the electron density decreases and particle surface area (presence of particles acts as sink for

argon metastables) increases, increase in electron temperature is dominant and results in the increase in the concentration of metastables.

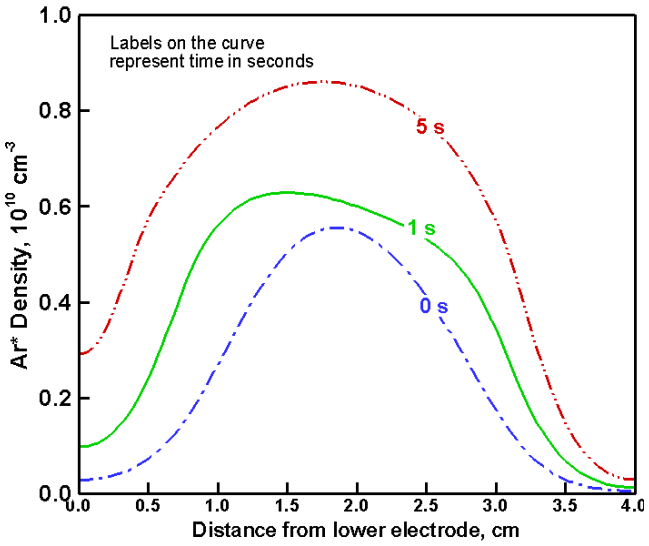


Figure 6.10: Spatial profiles of argon metastables density at 0 s, 1 s and 5 s

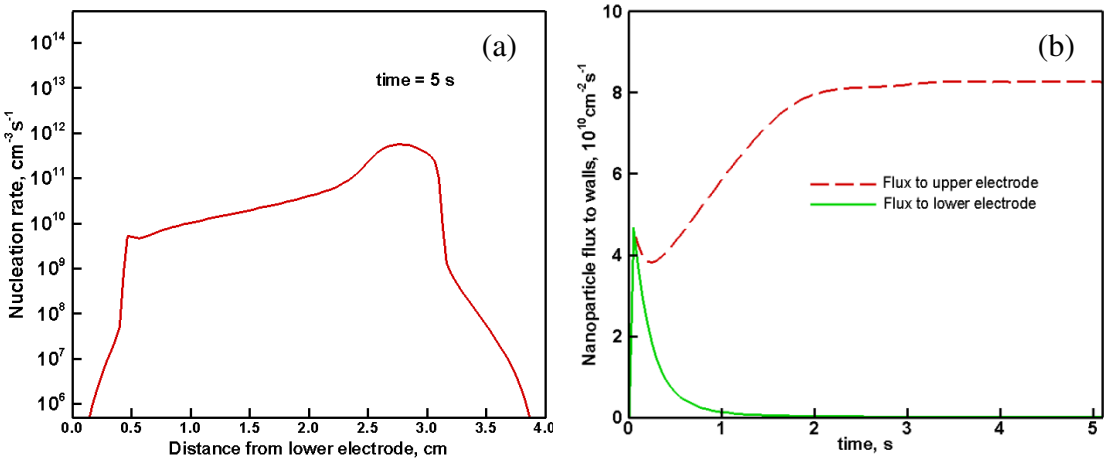


Figure 6.11: (a) Spatial profile of nucleation rate at 5 s and (b) nanoparticle flux to both the electrodes vs. time

Figure 6.11 (a) shows the spatial profile of nucleation rate. As mentioned earlier, nucleation rate follows the profiles of silyl and silylene anions and the nucleation rate is higher in relatively particle free regions. One consequence of nucleation becoming high in particle free regions near upper electrode is that the flux of small particles reaching upper electrode becomes greater than the flux of particle to the lower electrode as seen in figure 6.11 (b). This is counterintuitive because neutral drag tends to push particles away from upper electrode; however for small neutral particles (diameter ~ 2 nm) diffusion is more important than neutral drag. As the fresh particle formation takes place, particles that get negatively charged are trapped due to electric force and the neutral particles tend to diffuse towards electrodes. The flux of particles towards lower electrode is less because on their way to lower electrode, they may get negatively charged and trapped or they may coagulate with negatively charged particles.

Figure 6.12 shows the profile of surface growth rate at 5 s. It was mentioned earlier that profile of surface growth is related to profiles of silyl and silylene radicals. It is interesting to note in figure 6.12 and 6.7 (b) that the value of surface growth is lesser in the lower half of reactor and higher in the upper half of reactor at 5 s in comparison to 1 s. For example, at 1 s, at x = 1 cm and x = 2.8 cm, value of surface growth rate is 9 nm/s and 33 nm/s respectively. At 5 s, at x = 1 cm and x = 2.8 cm, value of surface growth rate is 2.1 nm/s and 38 nm/s respectively. This behavior is again related to the behavior of silyl and silylene radicals. As the particles grow bigger, they are pushed to lower electrode. Therefore, particle surface area available for the deposition of silyl and silylene radicals increases in the lower half of reactor as particles continue to grow bigger.

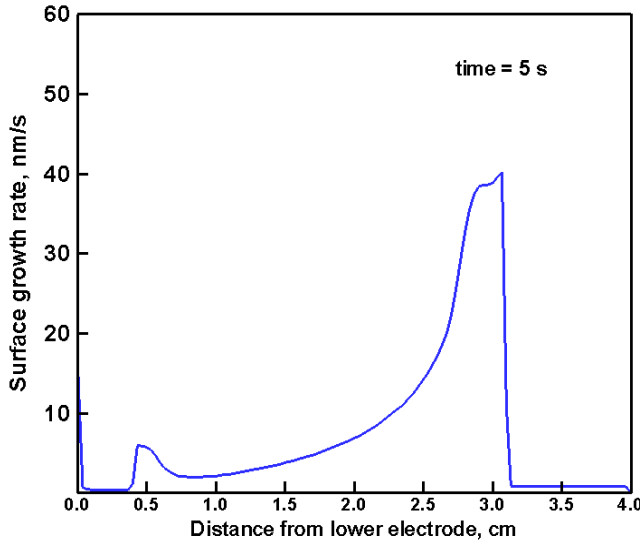


Figure 6.12: Spatial profile of surface growth rate at t = 5 s

However, it was mentioned earlier, electron temperature increases from 0 to 5 s. Increase in electron temperature results in increase in rate of electron impact dissociation of silane into silyl and silylene. Therefore, there is competition between consumption of silyl and silylene radicals by particles and the production of these radicals by electron impact dissociation. High consumption in lower half of reactor leads to decrease in silyl and silylene concentration in lower half of reactor whereas low consumption in the upper half of reactor leads to increase in the concentration of silyl and silylene radicals.

### 6.1.4 The evolution of particle size and concentration

Bouchoule and Boufendi (70) conducted particle collection measurements and laser light scattering measurements for different plasma on times. Based on these experiments, they describe the evolution of particle size and concentration by figure 6.13 (70). According to them, two well defined phases were observed. The first phase (0 to around 5 s in figure

6.13 (70)) is related to agglomeration or coagulation where particles of small size coagulate with each other and quickly form large particle. In this phase, particle growth rate was measured to be 10 nm/s and a sharp decrease in concentration was observed as seen in figure 6.13 (70). In the second phase (5 s to 30 s), concentration stays nearly constant and particles grow slowly by surface growth. Experimental conditions for this work consisted of 117 mTorr pressure, 30 sccm argon, 1.2 sccm silane and 600 V (peak to peak) voltage.

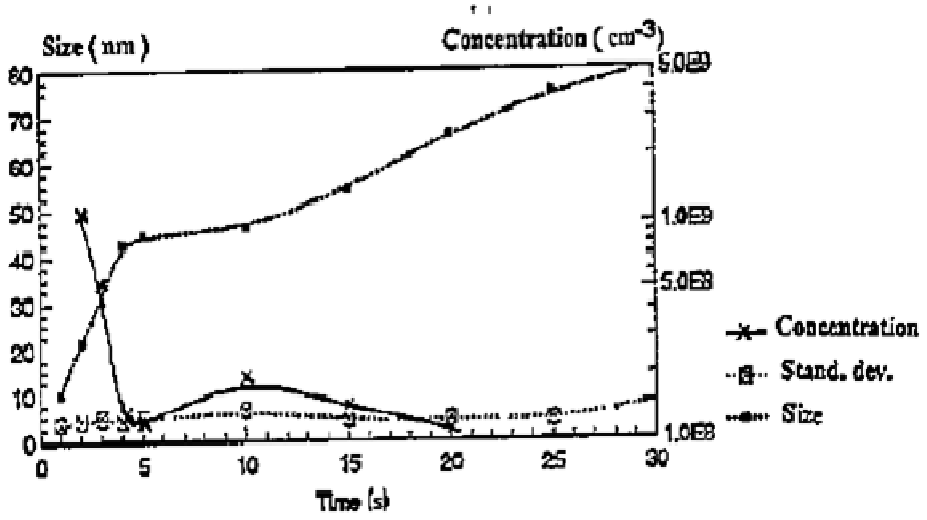


Figure 6.13: Evolution of particle size and concentration vs. time. Figure taken from Boufendi and Bouchoule (70)

In order to analyze the evolution of particle size and concentration, a similar plot as figure 6.13 (70) was created but using the results of numerical model results as seen in figure 6.14. Figure 6.14 shows the particle size vs. time and particle concentration at midplane vs. time. In the experiments, particles were collected over TEM grid. Particle sizes were measured and a size distribution was generated based on the count of particles

over the TEM grid. Diameter shown in figure 6.13 (70) is the mean diameter of size distribution in experiments. To represent the particle size in figure 6.14, modal diameters were obtained from numerical model at each spatial location and the largest modal diameter which has concentration greater than $10^7$ $cm^{-3}$ was selected. Particle concentration was simply the total concentration of particles at the midplane of the discharge. Considering the difference in experimental conditions and simulation conditions and the limitations involved in both experiments and simulations, simulation and experimental results find reasonable qualitative agreement. It is clear from figure 6.14 that the increase in particle size in first 2 seconds is faster and then the increase in particle size is at nearly steady rate. Similar to the results of Bouchoule and Boufendi (70) concentration at the center decreases relatively faster up to 2 seconds and then it decreases at a slower rate.

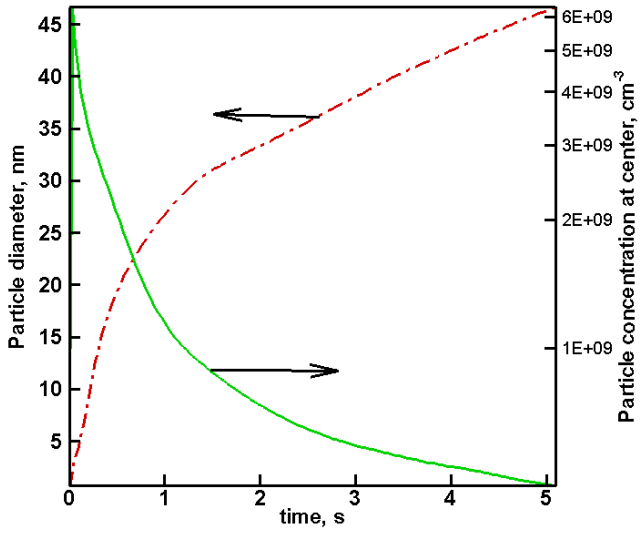


Figure 6.14: Evolution of particle size and concentration vs.time

From our numerical model, we find that the initial phase of fast growth up to 2 seconds in figure 6.14 is due to surface growth and the later phase of seemingly steady growth is also due to surface growth. Figure 6.15 (a) shows the surface growth rate at center vs. time. It is clear from figure 6.15 (a) that surface growth rate is higher at early times and decreases with time leveling off to a steady state value at much later time beyond 5 s. Such behavior is due to availability of chemical species like silyl and silylene radicals which participate in surface growth. Figure 6.15 (b) shows the concentration of silyl and silylene radicals at midplane vs. time. The concentration of silyl and silylene radicals decreases because of the consumption by particles. In the beginning at 100 ms, particles are smaller around 10 nm therefore the consumption rate of these species is lower. At later times, as the particles grow in size, consumption of these species increases resulting in the decrease in concentration of these species. Decrease in concentration in figure 6.14 is due to coagulation, diffusion and other transport mechanisms.

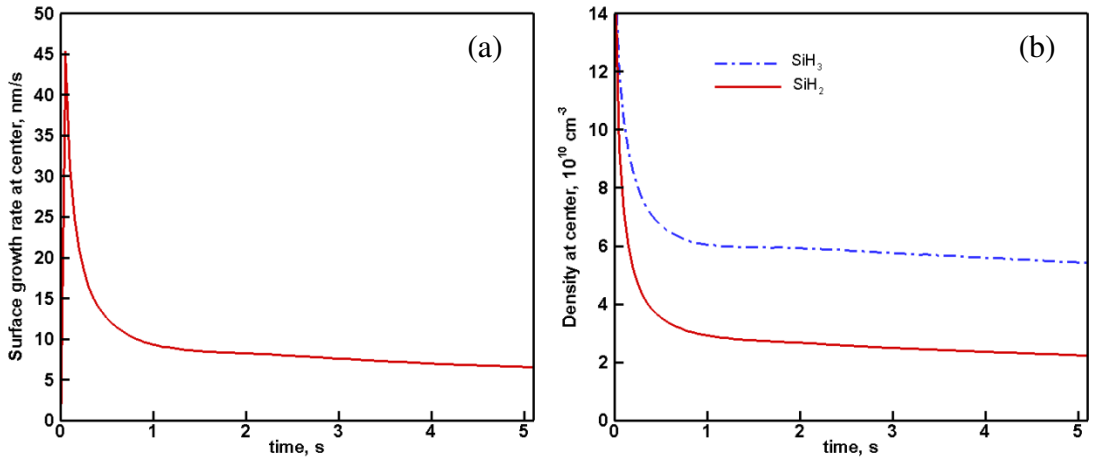


Figure 6.15: (a) Surface growth at center and (b) density of silyl and silylene radicals at center vs. time

## 6.2 Summary

A self consistent numerical model was developed to simulate argon silane plasmas. Numerical model consists of three modules namely plasma module, aerosol module and neutral chemistry modules. These three modules are self consistently coupled to each other. It was found that presence of particles significantly affect the composition of plasma. Nucleation and surface growth rates are calculated self consistently by chemistry calculations. Particle dynamics affects the nucleation and surface growth. As the particles grow bigger, they consume the chemical species and therefore nucleation shifts to relatively particle free regions. Evolution of particle size and concentration was discussed. It was found from numerical model that increase in particle size is due mainly to surface growth and decrease in particle concentration at center is due to decrease in nucleation rate as well as coagulation, diffusion and other transport mechanisms.

# Chapter 7: Conclusions and future work

In this work, numerical model developed by Girshick and coworkers (23,24) was modified to take advantage of a number of numerical enhancements, and run to a longer plasma times, thereby allowing consideration of phenomena affecting particles up to a few hundred nm in diameter. Spatiotemporal evolution of dust particle size and charge distribution was discussed. It was found that dust particles are strongly coupled to plasmas and the polydispersity in particle size and charge distribution has important consequences on particle dynamics and growth. At very early times following the onset of nucleation, when particles are at most a few nm in diameter, they are either neutral or have unit positive or negative charge because of stochastic charging. Negative particles are trapped due to electric force and thus grow by surface growth and coagulation whereas positive and neutral particles are lost to walls. Ongoing nucleation, coagulation, surface growth and diffusion lead to a polydisperse size distribution. When the nucleation is still present, size distribution is bimodal with two separate populations; one is the freshly nucleated small particles and other is the population of large stably trapped negatively charged particles. At this instant coagulation is primarily important between small neutral particles and larger negatively charged particles enhanced by image potentials in neutrals. As the particles grow bigger, forces on particles including neutral drag, ion drag and gravity cause the particle cloud to spread which eventually results in quenching of nucleation. Both the ion drag and electric force are charge dependent, so that the existence of a broad charge distribution, for particles of given size, affects the detailed structure of the particle cloud. Spreading of particle cloud affects the profiles of

electrons and ions. At later times, as the particles grow bigger, electron depletion in the region of maximum particle charge concentration becomes so strong that particles become less negatively charged on average with a small fraction becoming neutral or even positively charged. These non negative particles are not electrostatically trapped and therefore can deposit over electrodes or coagulate with negatively charged particles.

Sectional method was used to simulate particle size and charge distribution. Sectional method is quite computation intensive and suffers from numerical diffusion. Currently, implicit finite difference scheme has been used to discretize equations. Implicit schemes are difficult to parallelize. However, there are new developments in parallel processing techniques which involve use of GPU computing. Such techniques may offer possibility of numerical speed up. Numerical diffusion occurs because particle distribution within the section is considered to be uniform. It is suggested to look into the possibility of assuming piecewise particle size distribution within the section. Apart from section method, quadrature moment methods seem to offer promising approach for treating bivariate systems (108).

Numerical model predictions of laser light scattering and light emission from plasma were compared with the measured ones. Considering the limitations of numerical model and experiments, reasonable qualitative agreement was found with some discrepancies. Comparing the calculated and measured laser light scattering from particle cloud shows that majority of particles are located in the lower half of reactor because of neutral drag. Additionally, a double peak structure appears both in the measured and calculated spatial profiles of laser light scattering. Numerical model predicted that double peak structure is

due to Mie resonances. Double peak structure in experiments may either be due to Mie scattering or some other reasons like gas flow and reflection of laser. Mie scattering strongly depends on particle refractive index. Further laser light scattering experiments and particle collection experiments are required to understand the Mie scattering and the particle morphology in experiments. Discrepancies in the comparisons of laser light scattering might be due to 3D flow profile or reflection of laser light from top electrode. It is suggested to use low gas flow to avoid the complications due to gas flow profile.

It was observed both in experiments and numerical simulation that plasma light emission intensity first increases and then decreases. Plasma light emission depends on electron temperature and electron density. As the dust particles grow and the particle charge concentration increases, electron temperature increases whereas electron density decreases. At early times, increase in electron temperature dominates resulting in increase in the emission intensity. However, at later times, decrease in electron density dominates resulting in decrease in emission intensity. In the light emission measurements, it was found that stochastic heating is important in pristine plasma. Numerical model needs to be improved to account for stochastic heating of electrons.

Numerical model was modified to study the dusty plasma afterglow and pulsing. It was found that dusty plasma afterglow is dominated by different time scales for electron and ion dynamics. In dusty plasma afterglow, dust particle charging occurs primarily by ions because of rapid electron energy relaxation and free diffusion of electrons to walls. This results in a bipolar dust charge distribution. In turn, coagulation between large oppositely charged particles becomes important resulting in the broadening of dust particle size

distribution. Pulsed dusty plasmas were analyzed. Pulsed dusty plasmas may offer possibilities for controlling both nanoparticle properties and plasma characteristics. In numerical model, electron energy distribution was assumed to be Maxwellian. Electron energy distribution may differ significantly from Maxwellian distribution in afterglow. Similarly, orbital motion limited (OML) theory breaks down in decaying plasma. Therefore, kinetic treatment of electrons and particle charging is suggested in dusty plasma afterglow.

A simplified chemistry model was included in numerical model to simulate argon silane dusty plasmas. It was found that presence of particles significantly affects the chemical composition of plasma. Spatiotemporal evolution of dust particles, chemical species, nucleation rate and surface growth rate were discussed. Nucleation and surface growth are important outside the sheaths. Spatial profile of surface growth rate follows the profile of silyl and silylene radicals whereas that of nucleation rate follows the profile of silyl and silylene anions. Evolution of particle size and concentration was discussed and it was found that surface growth plays an important role in the evolution of particle size. In calculations of chemistry, reaction rate constants were calculated assuming the Maxwellian distribution of electrons. Electron distribution may differ from Maxwellian. This may have important consequence on the argon silane chemistry. Therefore, kinetic treatment of electrons is required to give more accurate results. Anion neutral reactions play an important role in particle formation. However, their rates are assumed to be the order of magnitude lower than Langevin rates. Reaction rates can also be calculated through quantum chemistry calculations. It is recommended that quantum chemistry

calculations should be performed for anion neutral reactions and the reaction rates should be modified accordingly. Plasma parameters like pressure, voltage, argon-silane ratio play an important role in plasma chemistry and particle dynamics. Simulations should be performed to explore the effects of these parameters.

In this work, numerical model consists of parallel plate capacitively coupled plasma. Numerical model can be extended to other types of plasma and geometries. Dust particles are generated in a variety of plasmas like fusion plasmas (109), inductively coupled plasmas (110) and capacitively coupled flow through reactors (111).

# References

(1) Merlino RL, Goree JA. Dusty plasmas in the laboratory, industry, and space. PHYSICS TODAY. 2004;57(7):32-39.

(2) Bouchoule A. Dusty plasmas: physics, chemistry, and technological impacts in plasma processing. : John Wiley & Sons Inc; 1999.

(3) Roth J, Tsitrone E, Loarte A, Loarer T, Counsell G, Neu R, Philipps V, Brezinsek S, Lehnen M, Coad P. Recent analysis of key plasma wall interactions issues for ITER. J Nucl Mater 2009;390:1-9.

(4) Winter J. Dust in fusion devices-experimental evidence, possible sources and consequences. Plasma Phys Controlled Fusion 1998;40:1201.

(5) Boufendi L, Bouchoule A. Industrial developments of scientific insights in dusty plasmas. Plasma Sources Sci Technol 2002;11:A211.

(6) Selwyn GS, Singh J, Bennett RS. In situ laser diagnostic studies of plasma-generated particulate contamination. Journal of Vacuum Science & Technology A: Vacuum, Surfaces, and Films 1989;7:2758.

(7) Boufendi L, Bouchoule A. Particle nucleation and growth in a low-pressure argon-silane discharge. Plasma Sources Sci Technol 1994;3(3):262-267.

(8) Barnes MS, Keller JH, Forster JC, O'Neill JA, Coultas DK. Transport of dust particles in glow-discharge plasmas. Phys Rev Lett 1992;68(3):313-316.

(9) Daugherty JE, Porteous RK, Graves DB. Electrostatic forces on small particles in low-pressure discharges. J Appl Phys 1993;73:1617.

(10) Choi SJ, Kushner MJ. The role of negative ions in the formation of particles in low-pressure plasmas. J Appl Phys 1993;74(2):853.

(11) Boufendi L, Plain A, Blondeau JP, Bouchoule A, Laure C, Toogood M. Measurements of particle size kinetics from nanometer to micrometer scale in a low-pressure argon-silane radio-frequency discharge. Appl Phys Lett 1992;60:169.

(12) Hamaguchi S, Farouki RT. Polarization force on a charged particulate in a nonuniform plasma. Physical Review E 1994;49(5):4430-4441.

(13) Tachibana K, Hayashi Y. Analysis of Coulomb-crystal formation process for application to tailored particle synthesis in RF plasmas. Pure and applied chemistry 1996;68:1107-1112.

(14) Poissant Y, Chatterjee P, Cabarrocas PRi. Analysis and optimization of the performance of polymorphous silicon solar cells: Experimental characterization and computer modeling. J Appl Phys 2003;94:7305.

(15) Kersten H, Thieme G, Fröhlich M, Bojic D, Tung DH, Quaas M, Wulff H, Hippler R. Complex (dusty) plasmas: Examples for applications and observation of magnetron-induced phenomena. Pure and applied chemistry 2005;77(2):415-428.

(16) Howling AA, Sansonnens L, Dorier JL, Hollenstein C. Negative hydrogenated silicon ion clusters as particle precursors in RF silane plasma deposition experiments. J Phys D 1993;26:1003-1006.

(17) Vepřek S, Schopper K, Ambacher O, Rieger W, Vepřek-Heijman MGJ. Mechanism of cluster formation in a clean silane discharge. J Electrochem Soc 1993;140:1935.

(18) Kawasaki H, Ohkura H, Fukuzawa T, Shiratani M, Watanabe Y, Yamamoto Y, Suganuma S, Hori M, Goto T. Roles of SiH3 and SiH2 radicals in particle growth in rf silane plasmas. Jpn.J.Appi.Phys.Vol 1997;36:4985-4988.

(19) Swihart MT, Girshick SL. Thermochemistry and kinetics of silicon hydride cluster formation during thermal decomposition of silane. J Phys Chem B 1999;103(1):64-76.

(20) Kee RJ, Rupley FM, Meeks E, Miller JA. CHEMKIN-III: A FORTRAN chemical kinetics package for the analysis of gas-phase chemical and plasma kinetics. : Sandia National Laboratories Livermore, CA; 1996.

(21) Bhandarkar UV, Swihart MT, Girshick SL, Kortshagen UR. Modelling of silicon hydride clustering in a low-pressure silane plasma. J Phys D 2000;33:2731-2746.

(22) Gallagher A, Howling A, Hollenstein C. Anion reactions in silane plasma. J Appl Phys 2002;91:5571.

(23) Warthesen SJ, Girshick SL. Numerical simulation of the spatiotemporal evolution of a nanoparticle-plasma system. Plasma Chem Plasma Process 2007 06;27(3):292-310.

(24) Ravi L, Girshick SL. Coagulation of nanoparticles in a plasma. Physical Review E (Statistical, Nonlinear, and Soft Matter Physics) 2009 02;79(2):026408 (9 pp.).

(25) Mott-Smith HM, Langmuir I. The theory of collectors in gaseous discharges. Physical review 1926;28(4):727-763.

(26) D'yachkov L, Khrapak A, Khrapak S, Morfill G. Model of grain charging in collisional plasmas accounting for collisionless layer. Phys Plasmas 2007;14(4):042102-042102-6.

(27) Zobnin AV, Nefedov AP, Sinel'shchikov VA, Fortov VE. On the charge of dust particles in a low-pressure gas discharge plasma. Journal of Experimental and Theoretical Physics 2000;91(3):483-487.

(28) Ratynskaia S, Khrapak S, Zobnin A, Thoma MH, Kretschmer M, Usachev A, Yaroshenko V, Quinn RA, Morfill GE, Petrov O. Experimental determination of dust-particle charge in a discharge plasma at elevated pressures. Phys Rev Lett 2004;93(8):85001.

(29) Gatti M, Kortshagen U. Analytical model of particle charging in plasmas over a wide range of collisionality. Physical Review E 2008;78(4):46402.

(30) Chu JH, I L. Direct observation of Coulomb crystals and liquids in strongly coupled rf dusty plasmas. Phys Rev Lett 1994;72(25):4009-4012.

(31) Bittencourt JA. Fundamentals of plasma physics. : Springer; 2004.

(32) Goree J, Morfill GE, Tsytovich VN, Vladimirov SV. Theory of dust voids in plasmas. Physical Review E 1999;59(6):7055-7067.

(33) Kilgore MD, Daugherty JE, Porteous RK, Graves DB. Ion drag on an isolated particulate in a low-pressure discharge. J Appl Phys 1993;73:7195.

(34) Khrapak SA, Ivlev AV, Morfill GE, Thomas HM. Ion drag force in complex plasmas. Physical Review E 2002;66(4):46414.

(35) Ivlev AV, Zhdanov SK, Khrapak SA, Morfill GE. Kinetic approach for the ion drag force in a collisional plasma. Physical Review E 2005;71(1):16405.

(36) Ikkurthi VR, Matyash K, Melzer A, Schneider R. Computation of ion drag force on a static spherical dust grain immersed in rf discharges. Phys Plasmas 2009;16:043703.

(37) Talbot L, Cheng RK, Schefer RW, Willis DR. Thermophoresis in a Heated Boundary Layer. J Fluid Mech 1980;101(4):737-758.

(38) Jellum GM, Daugherty JE, Graves DB. Particle thermophoresis in low pressure glow discharges. J Appl Phys 1991;69:6923.

(39) De Bleecker K, Bogaerts A, Goedheer W. Role of the thermophoretic force on the transport of nanoparticles in dusty silane plasmas. Physical Review E 2005;71(6):66405.

(40) Bogaerts A, Eckert M, Mao M, Neyts E. Computer modelling of the plasma chemistry and plasma-based growth mechanisms for nanostructured materials. J Phys D 2011;44:174030.

(41) Kushner MJ. A model for the discharge kinetics and plasma chemistry during plasma enhanced chemical vapor deposition of amorphous silicon. J Appl Phys 1988;63(8):2532-2551.

(42) Belenguer P, Blondeau JP, Boufendi L, Toogood M, Plain A, Bouchoule A, Laure C, Boeuf JP. Numerical and experimental diagnostics of rf discharges in pure and dusty argon. Physical Review A 1992;46(12):7923.

(43) Denysenko I, Berndt J, Kovacevic E, Stefanovic I, Selenin V, Winter J. The response of a capacitively coupled discharge to the formation of dust particles: Experiments and modeling. Phys Plasmas 2006;13:073507.

(44) Denysenko I, Yu MY, Ostrikov K, Smolyakov A. Spatially averaged model of complex-plasma discharge with self-consistent electron energy distribution. Physical Review E 2004;70(4):46403.

(45) Schweigert IV, Alexandrov AL, Ariskin DA, Peeters FM, Stefanović I, Kovačević E, Berndt J, Winter J. Effect of transport of growing nanoparticles on capacitively coupled rf discharge dynamics. Physical Review E 2008;78(2):26410.

(46) Kortshagen U, Bhandarkar U. Modeling of particulate coagulation in low pressure plasmas. Physical Review E 1999;60(1):887-898.

(47) De Bleecker K, Bogaerts A, Gijbels R, Goedheer W. Numerical investigation of particle formation mechanisms in silane discharges. Physical Review E 2004;69(5):56409.

(48) Scharfetter D, Gummel H. Large-signal analysis of a silicon read diode oscillator. Electron Devices, IEEE Transactions on 1969;16(1):64-77.

(49) Seigneur C, Hudischewskyj AB, Seinfeld JH, Whitby KT, Whitby ER, Brock JR, Barnes HM. Simulation of aerosol dynamics: A comparative review of mathematical models. Aerosol Science and Technology 1986;5(2):205-222.

(50) Talukdar SS, Swihart MT. Aerosol dynamics modeling of silicon nanoparticle formation during silane pyrolysis: a comparison of three solution methods. J Aerosol Sci 2004;35(7):889-908.

(51) Frenklach M, Harris SJ. Aerosol dynamics modeling using the method of moments. J Colloid Interface Sci 1987;118(1):252-261.

(52) Gelbard F, Tambour Y, Seinfeld JH. Sectional representations for simulating aerosol dynamics. J Colloid Interface Sci 1980;76(2):541-556.

(53) Warren DR, Seinfeld JH. Simulation of aerosol size distribution evolution in systems with simultaneous nucleation, condensation, and coagulation. Aerosol science and technology 1985;4(1):31-43.

(54) Huang DD, Seinfeld JH, Okuyama K. Image potential between a charged particle and an uncharged particle in aerosol coagulation--enhancement in all size regimes and interplay with van der Waals forces. J Colloid Interface Sci 1991;141(1):191-198.

(55) Gallagher A. Model of particle growth in silane discharges. Physical Review E 2000;62(2):2690-2706.

(56) U. V. Bhandarkar. Study of particle nucleation and growth in low pressure silane plasmas. University of Minnesota; 2003.

(57) S. J. Warthesen. Numerical investigations of nanodusty plasmas. University of Minnesota; 2006.

(58) Meeks E, Larson RS, Ho P, Apblett C, Han SM, Edelberg E, Aydill ES. Modeling of SiO2 deposition in high density plasma reactors and comparisons of model predictions with experimental measurements. Journal of Vacuum Science & Technology A: Vacuum, Surfaces, and Films 1998;16(2):544-563.

(59) Perrin J, Leroy O, Bordage M. Cross-Sections, Rate Constants and Transport Coefficients in Silane Plasma Chemistry. Contributions to Plasma Physics 1996;36(1):3-49.

(60) K. De Bleecker. Modeling of the formation and behavior of nanoparticles in dusty plasmas.Universiteit Antwerpen; 2006.

(61) Ho P, Coltrin ME, Breiland WG. Laser-induced fluorescence measurements and kinetic analysis of Si atom formation in a rotating disk chemical vapor deposition reactor. J Phys Chem 1994;98(40):10138-10147.

(62) Kushner MJ. A model for the discharge kinetics and plasma chemistry during plasma enhanced chemical vapor deposition of amorphous silicon. J Appl Phys 1988;63(8):2532-2551.

(63) Buss RJ, Ho P, Breiland WG, Coltrin ME. Reactive sticking coefficients for silane and disilane on polycrystalline silicon. J Appl Phys 1988;63(8):2808-2819.

(64) Raizer YP, Braun C. Gas discharge physics. Appl Opt 1992;31:2400-2401.

(65) Nienhuis G, Goedheer W, Hamers E, Van Sark W, Bezemer J. A self-consistent fluid model for radio-frequency discharges in SiH–H compared to experiments. J Appl Phys 1997;82:2060.

(66) Passchier J, Goedheer W. A two-dimensional fluid model for an argon rf discharge. J Appl Phys 1993;74(6):3744-3751.

(67) Quinn MJ. Parallel Programming in C with MPI and OpenMP. : 清华大学出版社; 2005.

(68) Gropp W, Lusk E, Skjellum A. Using MPI: portable parallel programming with the message-passing interface. : MIT press; 1999.

(69) Chapman B, Jost G, Van der Pas R, Kuck DJ. Using OpenMP: portable shared memory parallel programming. : The MIT Press; 2007.

(70) Bouchoule A, Boufendi L. Particulate formation and dusty plasma behaviour in argon-silane RF discharge. Plasma Sources Sci Technol 1993;2:204.

(71) Bouchoule A, Plain A, Boufendi L, Blondeau JP, Laure C. Particle generation and behavior in a silane-argon low-pressure discharge under continuous or pulsed radio-frequency excitation. J Appl Phys 1991;70(4):1991-2000.

(72) Kim DJ, Kim KS. Analysis on nanoparticle growth by coagulation in silane plasma reactor. AIChE J 2002;48(11):2499-2509.

(73) Rozsa K, Bano G, Gallagher A. The location of very small particles in silane RF discharge. Plasma Science, IEEE Transactions on 2001;29(2):256-260.

(74) Boufendi L, Bouchoule A, Hbid T. Electrical characterization and modeling of a dust forming plasma in a radio frequency discharge. Journal of Vacuum Science & Technology A: Vacuum, Surfaces, and Films 1996;14(2):572-576.

(75) Green MA, Keevers MJ. Optical properties of intrinsic silicon at 300 K. Prog Photovoltaics Res Appl 1995;3(3):189-192.

(76) Bohren CF, Huffman DR editors. Absorption and scattering of light by small particles. ; 1983.

(77) Vlcek J. A collisional-radiative model applicable to argon discharges over a wide range of conditions. I. Formulation and basic data. J Phys D 1989;22:623.

(78) Bhandarkar U, Kortshagen U, Girshick SL. Numerical study of the effect of gas temperature on the time for onset of particle nucleation in argon–silane low-pressure plasmas. J Phys D 2003;36:1399.

(79) Hollenstein C, Dorier JL, Dutta J, Sansonnens L, Howling AA. Diagnostics of particle genesis and growth in RF silane plasmas by ion mass spectrometry and light scattering. Plasma Sources Sci Technol 1994;3:278.

(80) Plain A. Determination of the size, optical index and density of particles in an argon–silane radio-frequency discharge. J Appl Phys 1998;83:4012.

(81) A. Bapat. Plasma synthesis of silicon nanocrystals: Development and diagnostics. University of Minnesota; 2007.

(82) F. Galli. Charge and Energy Interactions between Nanoparticles and Low Pressure Plasmas. University of Minnesota; 2010.

(83) Nitschke TE, Graves DB. A comparison of particle in cell and fluid model simulations of low-pressure radio frequency discharges. J Appl Phys 1994;76(10):5646-5660.

(84) Lymberopoulos D, Kolobov V, Economou D. Fluid simulation of a pulsed-power inductively coupled argon plasma. Journal of Vacuum Science & Technology A: Vacuum, Surfaces, and Films 1998;16(2):564-571.

(85) Ramamurthi B, Economou DJ. Pulsed-power plasma reactors: two-dimensional electropositive discharge simulation in a GEC reference cell. Plasma Sources Sci Technol 2002;11:324.

(86) Subramonium P, Kushner MJ. Two-dimensional modeling of long-term transients in inductively coupled plasmas using moderate computational parallelism. I. Ar pulsed plasmas. Journal of Vacuum Science & Technology A: Vacuum, Surfaces, and Films 2002;20(2):313-324.

(87) Kushner MJ. Pulsed plasma-pulsed injection sources for remote plasma activated chemical vapor deposition. J Appl Phys 1993;73(8):4098-4100.

(88) Shin H, Zhu W, Xu L, Donnelly VM, Economou DJ. Control of ion energy distributions using a pulsed plasma with synchronous bias on a boundary electrode. Plasma Sources Sci Technol 2011;20:055001.

(89) Economou D. Control of the Ion Energy Distribution on Plasma Electrodes. Bulletin of the American Physical Society 2011;56.

(90) Diomede P, Economou DJ, Donnelly VM. Particle-in-cell simulation of ion energy distributions on an electrode by applying tailored bias waveforms in the afterglow of a pulsed plasma. J Appl Phys 2011;109:083302.

(91) Shin H, Zhu W, Economou DJ, Donnelly VM. Ion energy distributions, electron temperatures, and electron densities in Ar, Kr, and Xe pulsed discharges. Journal of Vacuum Science & Technology A: Vacuum, Surfaces, and Films 2012;30:031304.

(92) Wang SB, Wendt AE. Control of ion energy distribution at substrates during plasma processing. J Appl Phys 2000;88:643.

(93) Ivlev AV, Kretschmer M, Zuzic M, Morfill GE, Rothermel H, Thomas HM, Fortov VE, Molotkov VI, Nefedov AP, Lipaev AM. Decharging of complex plasmas: First kinetic observations. Phys Rev Lett 2003;90(5):55003.

(94) Couëdel L, Mikikian M, Boufendi L, Samarian AA. Residual dust charges in discharge afterglow. Physical Review E 2006;74(2):26403.

(95) Couëdel L, Samarian AA, Mikikian M, Boufendi L. Dust charge distribution in complex plasma afterglow. EPL (Europhysics Letters) 2008;84:35002.

(96) Couëdel L, Samarian AA, Mikikian M, Boufendi L. Influence of the ambipolar-to-free diffusion transition on dust particle charge in a complex plasma afterglow. Phys Plasmas 2008;15:063705.

(97) Schweigert I, Alexandrov A. Effect of nanoparticles on an rf discharge afterglow. J Phys D 2012;45(32):325201.

(98) Denysenko I, Stefanović I, Sikimić B, Winter J, Azarenkov N, Sadeghi N. A global model for the afterglow of pure argon and of argon with negatively charged dust particles. J Phys D 2011;44:205204.

(99) Nefedov AP, Morfill GE, Fortov VE, Thomas HM, Rothermel H, Hagl T, Ivlev AV, Zuzic M, Klumov BA, Lipaev AM. PKE-Nefedov*: plasma crystal experiments on the International Space Station. New Journal of Physics 2003;5:33.

(100) Berndt J, Kovacevic E, Stefanovic I, Boufendi L. Controlled dust formation in pulsed rf plasmas. J Appl Phys 2009;106(6):063309-063309-8.

(101) Berndt J, Kovačević E, Selenin V, Stefanović I, Winter J. Anomalous behaviour of the electron density in a pulsed complex plasma. Plasma Sources Sci Technol 2006;15:18.

(102) Kim K, Park JH, Doo SG, Nam JD, Kim T. Generation of size and structure controlled Si nanoparticles using pulse plasma for energy devices. Thin Solid Films 2009;517(14):4184-4187.

(103) Saadane O, Longeaud C, Lebib S, Roca i Cabarrocas P. What makes a thin films semiconductor suitable for solar cells applications? Thin Solid Films 2003;427(1):241-246.

(104) Klauk H, Wright SL, Palmateer LF, Mohney SE, Jackson TN. Hydrogenated amorphous silicon germanium black-matrix material for active-matrix liquid-crystal displays. Journal of the Society for Information Display 2012;5(4):393-397.

(105) Optimization of Light Emission from Silicon Nanocrystals Grown by PECVD. Materials Research Society Symposium Proceedings: Cambridge Univ Press; 2010.

(106) Hollenstein C, Dorier J. Diagnostics of particle genesis and growth in RF silane plasmas by ion mass spectrometry and light scattering. Plasma Sources Sci Technol 1994;3:278.

(107) Liu XM, Song YH, Xu X, Wang YN. Phase-shift effects on growth and transport of dust particles in VHF capacitively coupled silane discharges: Two dimensional fluid simulation. Phys Plasmas 2011;18:083508.

(108) Yoon C, McGraw R. Representation of generally mixed multivariate aerosols by the quadrature method of moments: I. Statistical foundation. J Aerosol Sci 2004;35(5):561-576.

(109) Winter J. Dust: A new challenge in nuclear fusion research? Phys Plasmas 2000;7:3862.

(110) Bapat A, Perrey CR, Campbell SA, Barry Carter C, Kortshagen U. Synthesis of highly oriented, single-crystal silicon nanoparticles in a low-pressure, inductively coupled plasma. J Appl Phys 2003;94(3):1969-1974.

(111) Mangolini L, Thimsen E, Kortshagen U. High-yield plasma synthesis of luminescent silicon nanocrystals. Nano letters 2005;5(4):655-659.